UTILIZING THE STRUCTURE-PROPERTY RELATIONSHIP OF POROSITY AND COMPOSITION IN ADDITIVELY MANUFACTURED METALLIC SYSTEMS

A Dissertation

by

OLGA VALERIEVNA ELISEEVA

Submitted to the Office of Graduate and Professional Studies of
Texas A&M University
in partial fulfillment of the requirements for the degree of

DOCTOR OF PHILOSOPHY

Chair of Committee,	Ibrahim Karaman
Committee Members,	Raymundo Arroyave
	Ankit Srivastava
	Alaa Elwany
Head of Department,	Ibrahim Karaman

May 2021

Major Subject: Materials Science and Engineering

ABSTRACT

As the focus in additive manufacturing shifts to manufacturing parts in load bearing applications, microstructure and composition become of critical importance. In this work, we aim to enhance our understanding of the relationship between the process parameters, composition and the resulting microstructure of the additively manufactured parts, utilizing the structure-processing relationships. These relationships will be examined utilizing a combination of computational and experimental approaches. The two major questions we will explore are the compositional relationship of functional gradients to their printability and the relationship of thermal histories on porosity formation. The first question explores the compositional effects of diffusion, phase formation, and evaporation; while the second question explores the relationship of melting, evaporation, and process thermal history on defect formation.

The integrity of functional gradients in alloys tends to be compromised by the presence of brittle phases. Recently, CALPHAD-based thermodynamics tools have been used to generate isothermal phase diagrams that are in turn utilized to plan gradient paths that completely avoid these phases. However, existing frameworks rely extensively on the (limited) ability of humans to visualize and navigate high-dimensional spaces. To tackle this challenge, a Machine Learning approach was used and validated by designing and additively manufacturing a functional gradient in bulk samples from 316L stainless steel to pure chromium with a multi-material direct laser deposition system. The compositional

space was then increased from three powder feedstock to four, and a functional gradient from Fe_9Cr to W was fabricated.

Porosity is an expensive and pervasive problem in additively manufactured parts. To minimize materials waste and save time we propose a machine learning algorithm that can address the likelihood of porosity formation based on thermal signatures to feed into a process plan optimization methodology. The proposed scheme combines extensive cross sectional optical microscopy data from a laser powder bed fusion printed Ti-6Al-4V cylinder with a discrete thermal heat source model that produces a thermal signature at specific locations within an additively manufactured component. Experimentally determined porosity distributions are used to train and test a machine-learning algorithm to identify the likelihood of porosity formation at a given location. The effectiveness of this methodology is assessed and the overall link between porosity formation and thermal signatures is discussed.

DEDICATION

I would like to dedicate this dissertation to my mother Dr Tatiana Eliseeva, my hero, and my inspiration. Your tireless dedication to education throughout my life has been a driving force. Every day you told me that no one can take away what you have learned. Without your words of wisdom, I would have never grown into the person I am today. You taught me to keep my head up and все будет хорошо, for that I can never repay you.

ACKNOWLEDGEMENTS

I would like to acknowledge my committee Ibrahim Karaman, Raymundo Arroyave, Ankit Srivastava, Alaa Elwany and Edwin Schwalbach for their constant mentoring and support though out this process. I would also like to thank Jules and Sheri for their constant unwavering advice and for providing a safe space to vent my frustration. The department could not continue functioning with your tireless work or constant emotional support.

I would also like to thank my family for putting up with my 8 years of school and always offering support whether with a good wine or a good whine. I always had a hot meal and a hug waiting when I needed it most. I will also remember the impromptu beach trips and tyrannosaurus ribs; I wouldn't change a moment of it.

Finally, I would like to thank my wombat for his constant reassurance and cuddles. I could not have moved to Texas or completed this degree without the secret chocolate stashes or epic D&D sessions. You always know how to make me feel better or when I needed space, I don't know how but we got though this; together.

CONTRIBUTORS AND FUNDING SOURCES

Contributors

This work was supervised by a dissertation committee consisting of Professor Ibrahim Karaman of the Department of Materials Science and Engineering, Professor Raymundo Arroyave of the Department of Materials Science and Engineering, Professor Ankit Srivastava of the Department of Materials Science and Engineering, Professor Alaa Elwany of the Department of Industrial & Systems Engineering, and Doctor Edwin Schwalbach of the Air Force Research Laboratory.

The WDS data analyzed for Chapters 2 and 3 was provided by Dr. Andrew Mott. The XRD analyses depicted in Chapter 2 and 3 were conducted in part by Dr. Anup Bandyopadhyay of the Department of Materials Science and Engineering. The computational model in Chapters 2 and 3 was created by Tanner Kirk of the Department of Mechanical Engineering and Dr. Raymundo Arroyave of the Department of Materials Science and Engineering. Chapter 4 is a collaborative effort with Air Force Research Laboratory (AFRL). All other work conducted for the dissertation was completed by the student independently.

Funding Sources

The author would like to thank the U.S. Air Force Research Laboratory – Minority Leaders Program (subcontract UTC-17-S7700-01-C5), QuesTek in partnership with U.S. Department of Energy, Grant No. DE-SC0020032 and the U.S. Army Research Office (Award No. W911NF-18-1-0278 P00001) for funding the research presented in this work.

The author also acknowledges the support of the U.S. National Science Foundation through a Fellowship from the Texas A&M NSF Research Traineeship (NRT) Program on Data Enabled Discovery and Development of Energy Materials (D3EM) under Grant No. NSF-DGE-1545403. The acquisition of the direct energy deposition system utilized in this work was funded by the U.S. Air Force Office of Scientific Research, Aerospace Materials for Extreme Environments Program, under Grant No. FA9550-16-1- 0311.

NOMENCLATURE

AFRL	Air Force Research Laboratory
AM	Additive Manufacturing
BCC	Body Centered Cubic
BSE	Backscattered-Electron
CALPHAD	CALculation of PHAse Diagram
CSA	Constraint Satisfaction Algorithm
CT	Computed Tomography
DED	Direct Energy Deposition
DT	Decision Tree
EDM	Electrical Discharge Machining
EDS	Energy Dispersive Spectroscopy
EPMA	Electron Microprobe Analyzer
FCC	Face Centered Cubic
FGMs	Functionally Graded Materials
HCS	Hot Cracking Susceptibility
HT	Heat Treatment
KNN	K-Nearest Neighbour
LENS	Laser Engineered Net Shaping
LOF	Lack-of-Fusion
LPBF	Laser Powder Bed Fusion

RRT	Rapidly Exploring Random Tree
RRT*FN	Rapidly Exploring Random Tree algorithm with a Fixed-Node
SAD	Selected Area Diffraction
SEM	Scanning Electron Microscope
SS	Stainless Steel
SVDD	Support Vector Data Description
SVM	Support Vector Machine
TEM	Transmission Electron Microscopy
TTT	Time-Temperature-Transformation
WDS	Wavelength Dispersive Spectroscopy
XRD	X-ray Diffraction

TABLE OF CONTENTS

Page

LIST OF FIGURES

Page

LIST OF TABLES

Page

1. INTRODUCTION

Materials science relies on the understanding and analysis of the process-structure-property relationship. The process-structure-property relationship is complex, and a substantial investment of time and money is required to research this relationship in newer manufacturing techniques, such as metallic additive manufacturing.

While metal additive manufacturing (AM) has been around since the 80's; for much of its existence, the industry focused on creating geometrically accurate parts for non-load bearing applications [1]–[4]. Achieving geometric accuracy moved the focus to using powder bed fusion AM techniques to create fine details and geometrically accurate parts with little to no post processing [5]–[8]. Many advancements were made for the manufacturing of prototype quality parts and creating molds for mass market production [9]–[11]. In recent years, focus has again shifted from using additive parts as molds for mass manufacturing to creating additive parts for direct use. Direct use of additive parts requires that these parts are able withstand stress critical situations, high temperature, and harsh environments.

To meet these requirements and demands, parts must be manufactured from materials with accurate microstructure and precise compositions. Largely dismissed until recent years, research focusing on how to control compositional homogeneity or compositional heterogeneity on demand and porosity is vital. In order to create components with precise chemistries, microstructures and specific properties, engineers must understand how to control process parameters to tailor these properties by revealing process-structure relationships. Traditional post-processing cannot eliminate all

fabrication and microstructural problems that result during additive manufacturing [13]–[15]. Therefore, chemical and microstructural tailoring must be completed during printing the part.

In this work, we look to further our understanding of the relationship between the process parameters and the resulting metallic microstructure. The two major questions we will address are the accurately controlling the local composition in functional gradients by controlling processing history and the relationship between process thermal histories and porosity. The first question explores the compositional effects of diffusion, phase formation, and evaporation; while the second question explores the relationship of melting, evaporation, and process thermal history on defect formation.

1.1. References

[1] "Additive manufacturing of metals - ScienceDirect." https://www.sciencedirect.com/science/article/pii/S1359645416305158 (accessed Jan. 07, 2020).

[2] W. E. Frazier, "Metal Additive Manufacturing: A Review," J. Mater. Eng. Perform., vol. 23, no. 6, pp. 1917–1928, Jun. 2014, doi: 10.1007/s11665-014-0958-z.

[3] T. D. Ngo, A. Kashani, G. Imbalzano, K. T. Q. Nguyen, and D. Hui, "Additive manufacturing (3D printing): A review of materials, methods, applications and challenges," Compos. Part B Eng., vol. 143, pp. 172–196, Jun. 2018, doi: 10.1016/j.compositesb.2018.02.012.

[4] D. Herzog, V. Seyda, E. Wycisk, and C. Emmelmann, "Additive manufacturing of metals," Acta Mater., vol. 117, pp. 371–392, Sep. 2016, doi: 10.1016/j.actamat.2016.07.019.

[5] B. Fotovvati and E. Asadi, "Size effects on geometrical accuracy for additive manufacturing of Ti-6Al-4V ELI parts," Int. J. Adv. Manuf. Technol., vol. 104, no. 5, pp. 2951–2959, Oct. 2019, doi: 10.1007/s00170-019-04184-1.

[6] H. Luan, M. Grasso, B. M. Colosimo, and Q. Huang, "Prescriptive Data-Analytical Modeling of Laser Powder Bed Fusion Processes for Accuracy Improvement," J. Manuf. Sci. Eng., vol. 141, no. 1, Jan. 2019, doi: 10.1115/1.4041709.

[7] M. Aminzadeh and T. Kurfess, "Vision-Based Inspection System for Dimensional Accuracy in Powder-Bed Additive Manufacturing," presented at the ASME 2016 11th International Manufacturing Science and Engineering Conference, Sep. 2016, doi: 10.1115/MSEC2016-8674.

[8] M. Khanzadeh, P. Rao, R. Jafari-Marandi, B. K. Smith, M. A. Tschopp, and L. Bian, "Quantifying Geometric Accuracy With Unsupervised Machine Learning: Using Self-Organizing Map on Fused Filament Fabrication Additive Manufacturing Parts," J. Manuf. Sci. Eng., vol. 140, no. 3, Mar. 2018, doi: 10.1115/1.4038598.

[9] Y.-A. Song, S. Park, D. Choi, and H. Jee, "3D welding and milling: Part I–a direct approach for freeform fabrication of metallic prototypes," Int. J. Mach. Tools Manuf., vol. 45, no. 9, pp. 1057–1062, Jul. 2005, doi: 10.1016/j.ijmachtools.2004.11.021.

[10] C. T. Mueller, A. Irani, and B. E. Jenett, “Additive Manufacturing of Structural Prototypes for Conceptual Design,” Proc. IASS Annu. Symp., vol. 2014, no. 16, pp. 1–8, Sep. 2014.

[11] A. Gebhardt, Understanding Additive Manufacturing: Rapid Prototyping • Rapid Tooling • Rapid Manufacturing. München: Carl Hanser Verlag GmbH & Co. KG, 2011.

[12] “Metal Additive Manufacturing: A Review of Mechanical Properties | Annual Review of Materials Research.” https://www.annualreviews.org/doi/abs/10.1146/annurev-matsci-070115-032024 (accessed Jan. 07, 2020).

[13] N. Sanaei, A. Fatemi, and N. Phan, “Defect characteristics and analysis of their variability in metal L-PBF additive manufacturing,” Mater. Des., vol. 182, p. 108091, Nov. 2019, doi: 10.1016/j.matdes.2019.108091.

[14] S. Gangireddy, E. J. Faierson, and R. S. Mishra, “Influences of Post-processing, Location, Orientation, and Induced Porosity on the Dynamic Compression Behavior of Ti–6Al–4V Alloy Built Through Additive Manufacturing,” J. Dyn. Behav. Mater., vol. 4, no. 4, pp. 441–451, Dec. 2018, doi: 10.1007/s40870-018-0157-3.

[15] L. Hackel, J. R. Rankin, A. Rubenchik, W. E. King, and M. Matthews, “Laser peening: A tool for additive manufacturing post-processing,” Addit. Manuf., vol. 24, pp. 67–75, Dec. 2018, doi: 10.1016/j.addma.2018.09.013.

2. FUNCTIONALLY GRADED MATERIALS THROUGH ROBOTICS-INSPIRED PATH PLANNING*

2.1. Introduction

Additive manufacturing (AM) enables many opportunities for design by exceeding the capabilities of conventional manufacturing, specifically with respect to part shape and material composition [1–4]. One rapidly expanding area of research in AM is the utilization of location-dependent composition control to create Functionally Graded Materials (FGMs) [5–9], characterized by the gradual variation in composition and microstructure, on a location-by-location basis, resulting in corresponding changes in the properties/behavior of the material. Much research has been done on the use of locational composition/structure control in polymers [10–14], but less attention has been paid to compositional grading in metals [9, 15]. While there are multiple ways to achieve a functional gradient, a common approach is to vary the composition of the manufactured part on a layer-by-layer basis by making use of direct energy deposition (DED)-based 3D printers with multi-powder capabilities [1–4,16–18]. By independently controlling the feeding rate for different powders the corresponding composition of the deposited metal can be controlled [4]. However, even though this methodology provides the ability to create functional gradients, the process does not always result in functional/reliable parts [2, 3]. Challenges that can cause the failure of an FGM part/component include

* O. V. Eliseeva et al., "Functionally Graded Materials through robotics-inspired path planning," Materials & Design, vol. 182, p. 107975, Nov. 2019, doi: 10.1016/j.matdes.2019.107975.

mismatched lattices, differences in thermal expansion coefficients, and difficulty in optimizing printing parameters for multiple materials simultaneously. Even if all of these difficulties are accounted for, part failure can still occur from the formation of detrimental, often brittle, phases [4]. It is thus important to minimize the possibility of failure and maximize performance given the interest in these materials in risk-averse industries like defense and aerospace [1, 6].

Many earlier works have established that the formation of deleterious phases is a common occurrence in the creation of gradient alloys. Carroll et al. [3] employed DED to manufacture a gradient from 304L stainless steel to Inconel 625. However, microcracks were observed to form in the gradient due to the presence of carbides. After analysis, these carbides were shown to be predicted by CALculation of PHAse Diagram (CALPHAD) software [19,20]. Reichardt et al. [2] attempted to plan a gradient between Ti-6Al-4V to 304L stainless steel by including a Vanadium interlayer but observed cracking due to the formation of brittle intermetallics that were also predicted by CALPHAD-based phase stability calculations. In Bobbio et al. [4], brittle intermetallics led to significant cracking in a gradient from Ti-6Al-4V to Invar 36. These works show that although deleterious phases are often encountered in FGMs, they can be consistently predicted by CALPHAD-based methods, provided suitable thermodynamic databases are available.

Hofmann et al. [1,6] proposed an approach to prevent the formation of detrimental phases along linear composition gradients in which CALPHAD-based predictions of isothermal ternary sections were used to visualize the regions where

detrimental phases were likely to form, defining then a gradient path that circumvented these regions. Figure 1 provides an example of this process. After using computational thermo- dynamics software (based on CALPHAD Gibbs energy parameterizations) to

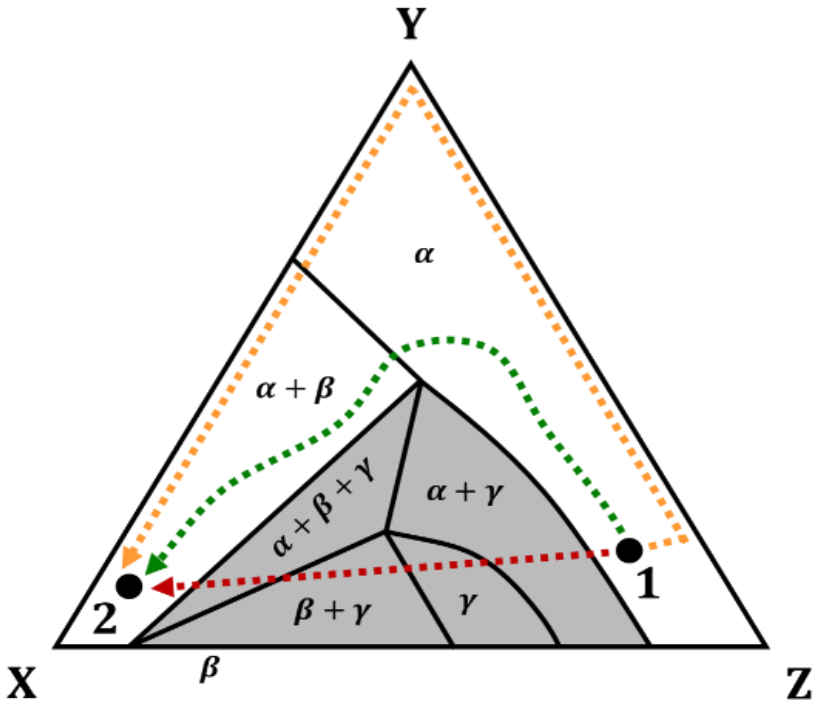

Figure 1. An example of how an isothermal ternary phase diagram can be used to design Functionally Graded Materials (FGMs), as proposed by Hofmann et al. [1,2]. Consider γ phase to be a detrimental phase that appears in ternary alloys composed of elements X, Y, and Z. The linear gradient (shown in red) between alloy 1 and 2 will develop a significant amount of γ phase, while a gradient (shown in yellow) that follows the Y-Z and X-Y binaries will not develop any γ phase. Some other gradient (shown in green) might also avoid γ phase, while requiring less deviation from the linear gradient.

generate an isothermal phase diagram of the relevant system, detrimental phases can be located in composition space. Subsequently, gradient paths can be planned such that these regions of the phase diagram are avoided. However, this technique is limited to visualizing three elements (or two degrees of freedom in the composition space) at a

time at a single temperature. As such, it becomes increasingly cumbersome as the number of elements increases and the temperature of the process fluctuates. Moreover, since the analysis is limited to isothermal sections, existing frameworks are incapable of predicting none equalibrium detrimental phases at intermediate temperatures prevalent during the fabrication process, as well as during post-processing treatments, such as hot isostatic pressing (HIP) as well as homogenization or stress relief heat treatments.

The present work demonstrates the feasibility of a novel computational design method for FGMs that plans compositional gradients such that detrimental phases are avoided, as detailed in Kirk et al. [21]. This method improves upon previous works by encoding the proposed design methodology algorithmically, enabling FGM gradient paths to be planned in high-dimensional spaces and optimized with respect to some cost function. With the ability to plan gradient paths in high-dimensional spaces, FGMs consisting of any arbitrarily large number of elements can in principle be designed. The method consists of two major steps. First, machine learning techniques are used to map regions in the multi-dimensional composition-temperature space that contain detrimental phases over a range of temperatures. This is followed by the use of a motion planning algorithm adapted from the robotics community to plan a compositional gradient path that optimizes a given cost function. Regions of detrimental phases identified during the first step are considered to be ‘obstacles’ to be avoided during path planning. This results in designed gradient pathways that are more robust to manufacturing temperatures, cooling rates, or post-fabrication heat treatment. Selection of an appropriate cost function is essential to guarantee FGM robustness. For example, using a path planning

objective of maximizing compositional distance from detrimental phase regions would increase robustness to uncertainty in phase diagram predictions or compositional variance in the manufacturing process.

To assess the feasibility of the method, FGM gradient paths were designed from austenitic 316L steel to 100% chromium while avoiding two detrimental phases ($CrNi_2$ and σ phases). Paths were optimized to increase the chance of success under the constraints given by manufacturing limitations. Using a Laser Engineered Net Shaping (LENS) DED system with four powder hopper capabilities, the designed FGMs were created and compositionally and microstructurally evaluated to determine the effectiveness of the design method in eliminating detrimental phases. For a more in-depth explanation of the algorithm used refer to Appendix 1.

2.2. Experimental Procedure

To fabricate bulk samples and validate the designed functionally gradient path between 316L stainless steel (SS) and 100% chromium, three different types of powders were utilized: 316L stainless steel, pure nickel and pure chromium in order to sample the different regions of the Fe-Ni-Cr ternary phase diagram. The bulk samples were fabricated using an Optomec LENS MR 7 direct energy deposition (DED) AM system. The powders were fabricated using gas atomization in argon and had spherical shapes. The stainless steel and nickel powders were commercially obtained from LPW Technology and the chromium powder was fabricated by TLS Technic. The powders had a size distribution ranging from 44μm to 106μm, with an average particle size or the d50 of around 84μm.

Before loading the powders into the powder feeders and printing, all powders were dried for 12 h at 80 °C in an argon-controlled atmosphere to remove any remaining moisture from manufacturing and handling. The powders were then transferred into the hoppers of the LENS system while still inside the argon-controlled atmosphere (in a glove box), in order to minimize oxidation and moisture contamination, which cause clumping and inconsistent flow rates from the powder feeders.

A 304L stainless steel plate was used as the substrate for printing, which was solution heat treated at 850 °C for 6 h and water quenched to remove preferential orientation, precipitate phases, and any residual stress that may exist. The substrate was then polished to remove the oxide layer and coated with a thin layer of carbon dry lubricant to prevent back reflection under the laser. The Optomec LENS MR 7 printer has 4 separate hoppers, 3 of which were employed for these experiments. Before printing the gradient structures, a process parameter selection procedure was followed in order to fabricate defect free cubes from the three initial powders selected. Cubes from each powder were printed using a systematic parameter sweep. The parameters examined were the laser power at 300 W, 350 W, 400 W, the hatch spacing of 0.25 mm, 0.38 mm, 0.50 mm (hatch spacing: the distance between the centers of the subsequent laser passes), and the platen speed of 25.4 cm/min, 38.1 cm/min, 50.8 cm/min.

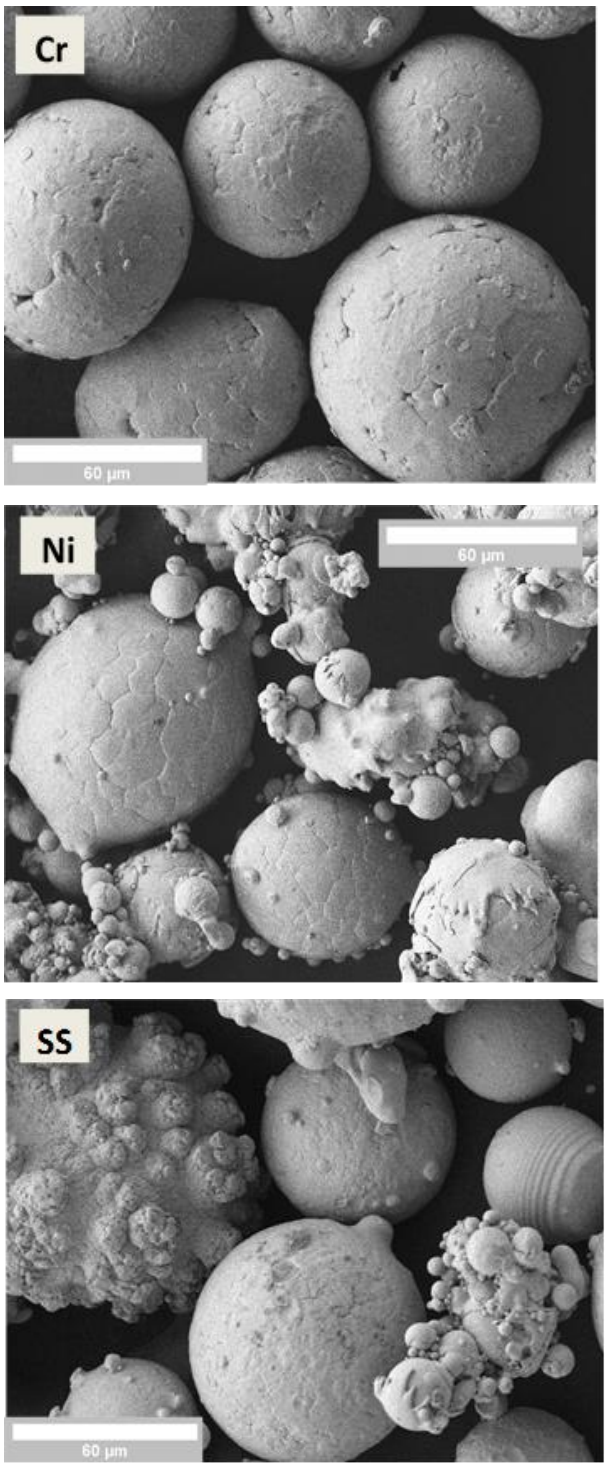

Figure 2. Backscattered electron images of the three different powders used in this study, showing the surface roughness and satellites of individual powders before printing.

The total of 27 pillars of 5 mm diameter and 5 mm length were printed for each material. The above parameters were selected based on the suggested printing parameters provided by the LENS vendor. From the sets of samples that resulted in the greatest density, the following parameters were identified as optimum for each material powder: 350 W laser power, 38.1 cm/min platen speed, and 0.38 mm hatch spacing for stainless steel, 400 W laser power, 38.1 cm/min platen speed, and 0.38 mm hatch spacing for chromium, and 325 W laser power, 38.1 cm/min platen speed, and 0.38 mm hatch spacing for nickel. Since these parameters are the same for hatch spacing and platen speed, and only slightly different in laser power, the final printing parameters of 350 W laser power, 38.1 cm/min platen speed, and 0.38 mm hatch spacing were selected. The last parameter to be determined was the flow rate used in each of the feeders. As flow rate is not directly controlled in the existing LENS system, the rotation rate of the internal disk in the hoppers, that allow the powder to pass through powder channels, was used to indirectly control the flow rates. Preliminary prints of the functionally graded samples revealed that if the same powder flow rate was used for all three powders during the mixing, the Cr content in the mix was depressed relative to the rest of the powders.

Upon examination of the powders under scanning electron microscopy using backscattered electron mode (Figure 2), it was observed that the Cr powder was perfectly spherical and lacked satellites as compared to other powders. The lack of satellites increases packing ability and decreases flowability. Therefore, while a

maximum rotation rate of 6 rpm was used for Ni and stainless steel, 7 rpm was used for Cr powder, to overcome the flowability differences.

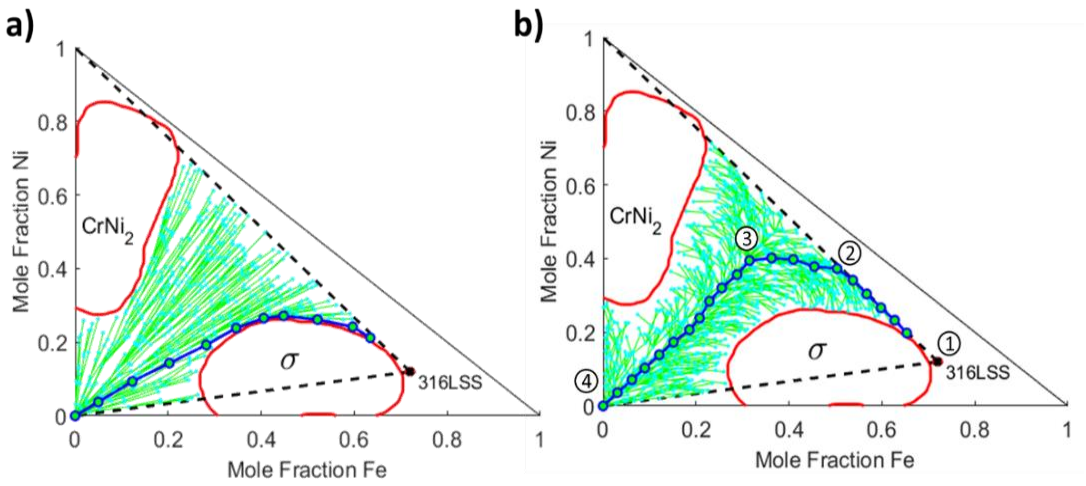

Figure 3. a) The decision tree created by the RRT*FN algorithm (see text for details) when minimizing the path length to go from 316L stainless steel to pure chromium in the Fe-Cr-Ni phase map, estimated by the Constraint Satisfaction Algorithm, while avoiding both CrNi2 and σ phases. The optimal path is shown in blue. b) The decision tree created by the RRT*FN algorithm when maximizing the distance from the undesirable phase regions. The optimal path is shown in blue. The numbered points represent the vertices of the simplified path used for experimental validation.

Two different functionally graded samples were fabricated in bulk: a linear gradient sample going directly from 316L SS to 100% Cr on a linear path in the compositional space (Figure 3, the black dashed line), and the planned gradient sample with the compositional path having the maximum distance from the deleterious phase boundaries (Figure 3b). The linear gradient sample had the dimensions of 22 mm × 10 mm × 10 mm and the planned gradient sample was a 12.7 mm × 12.7 mm × 12.7mm cube.

These samples were created in a computer aided design software (AutoCAD 2018), which was then converted and sliced into layers using the vendor's field

converter. A gradient path design software, provided by the LENS vendor, was used to create the process parameters to print the desired gradients. The software takes the desired starting and end flow rates (i.e. rotation rates) as well as the user defined number of layers to achieve the gradient into account. Then, each horizontal layer, measuring roughly 0.0254 cm in thickness, in the gradient structure has a single composition that is calculated within the program by taking the final rotation speed, subtracting the starting rotation speed, and dividing by the number of layers specified by the user. While this is a simple task for the linear gradient samples, it is more difficult for the planned, non-linear paths employed in this study. In the latter case, the 4 critical points, as shown in Figure 3b, were calculated and a linear path was drawn between these points, starting from the initial condition of 100% stainless steel and ending at the final condition of 100% Cr. This allowed for the planned, fragmented paths to be calculated in a similar way to the linear path.

After the fabrication, the functionally graded samples were cut using wire electrical discharge machining (EDM) in 2 mm slices with the normal axis of the slices perpendicular to the long axis (z axis), which is parallel to the built direction, such that each slice includes all layers in the gradient. One of the slices from each functionally graded sample was then embedded in epoxy mount and mechanically polished down to a 0.01μm surface finish, first using Si carbide paper from 600 grit to 1200 grit, followed by diamond paste polishing from 6μm to 0.05μm, and finished off with a Si slurry with 0.01μm particle size. The phase structures of the gradient samples were then determined using a Bruker-AXS D8 X-ray diffractometer with Cu Kα (wavelength $\lambda = 0.154$ nm)

radiation. The microstructure of the samples was examined using a JEOL JSM-7500F scanning electron microscope (SEM) equipped with an Oxford Energy Dispersive Spectroscopy (EDS). More detailed local chemical analysis was performed using a Cameca SX Five Electron Microprobe Analyzer (EPMA) using wavelength dispersive spectroscopy (WDS), operated at 15 keV and 20 mA. Another slice for each gradient case was polished down to 100μm thickness, and 3 mm discs were mechanically punched from the foils for transmission electron microscopy (TEM) investigation. These discs were electrolytically polished in a Struers TenuPol-5 twin jet electro-polisher using a solution of 10% perchloric acid in methanol at 12 V and −30 °C. The samples were then examined in a FEI Tecnai G2 F20 transmission electron microscope (TEM) operating at 200 kV accelerating voltage.

2.3. Results and Discussion

A functionally graded bulk sample was first fabricated using the linear gradient path from 316L SS to pure chromium, as shown in Figure 4 (the black line). Each layer was a discrete step between the starting composition and the final composition divided by the number of layers. This specimen acted as a baseline to understand the formation kinetics of σ phase. As shown in Figure 4, most of the linear path is within the predicted σ phase region and the path directly intersects the single-phase σ region. As such, it is expected that more σ phase will be present in this sample than the σ phase in the sample fabricated using the planned gradient path. The linear gradient path resulted in a distinct vertical crack in the sample along the build direction, as shown in Figure 5a. It was hypothesized that the relatively large volume fraction of σ phase should be responsible

for cracking during printing as the material cannot accommodate the process induced residual stresses, due to the presence of brittle phases [24]. The σ phase formation results in higher hardness values and degrades both elongation to failure and toughness in steels [24]. To explore whether or not σ phase was responsible for the cracking seen in the sample with the linear gradient path, SEM images were taken around the cracks. While the backscattered electron images, as shown in Figure 5b, did not show distinct contrast around the cracks, indicative of σ phase, elemental analysis via EDS revealed the chemical composition around cracks were in fact consistent with the composition of the σ phase. While it is impossible to unequivocally state whether the σ phase caused the crack without further characterization, the inherent brittle nature of the phase combined with the composition around the crack being well within the σ region, may indicate that the σ phase contributed to the crack initiation and/ or propagation. Note that the spherical dark region in Figure 5b is rich in Cr which might be an unmelted Cr particle.

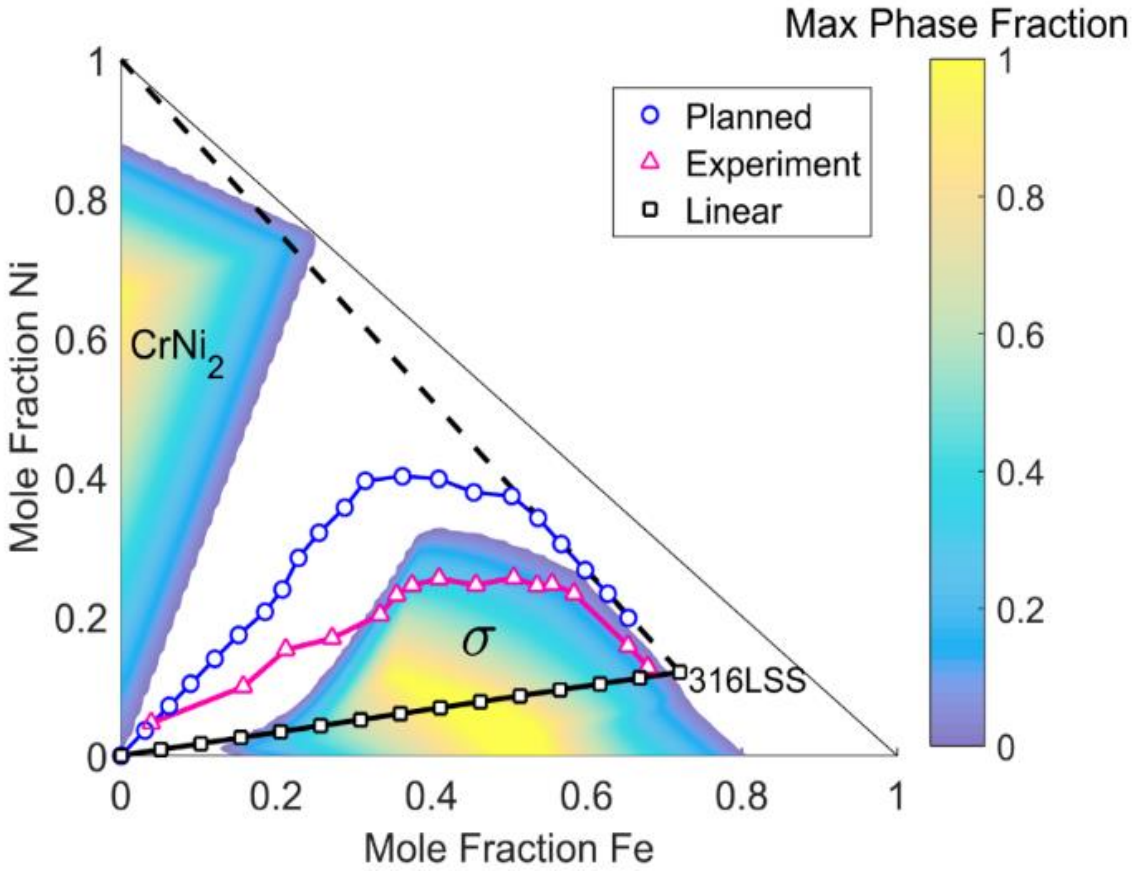

Figure 4. The linear gradient as well as the nominal and experimental paths for the planned gradient are shown in the composition space in order to fabricate functionally graded samples starting from 316L stainless steel and ending at pure chromium while avoiding the detrimental phases (CrNi2 and σ). Also shown is the maximum phase fraction encountered from 300 to 1100 K for both CrNi2 and σ phase.

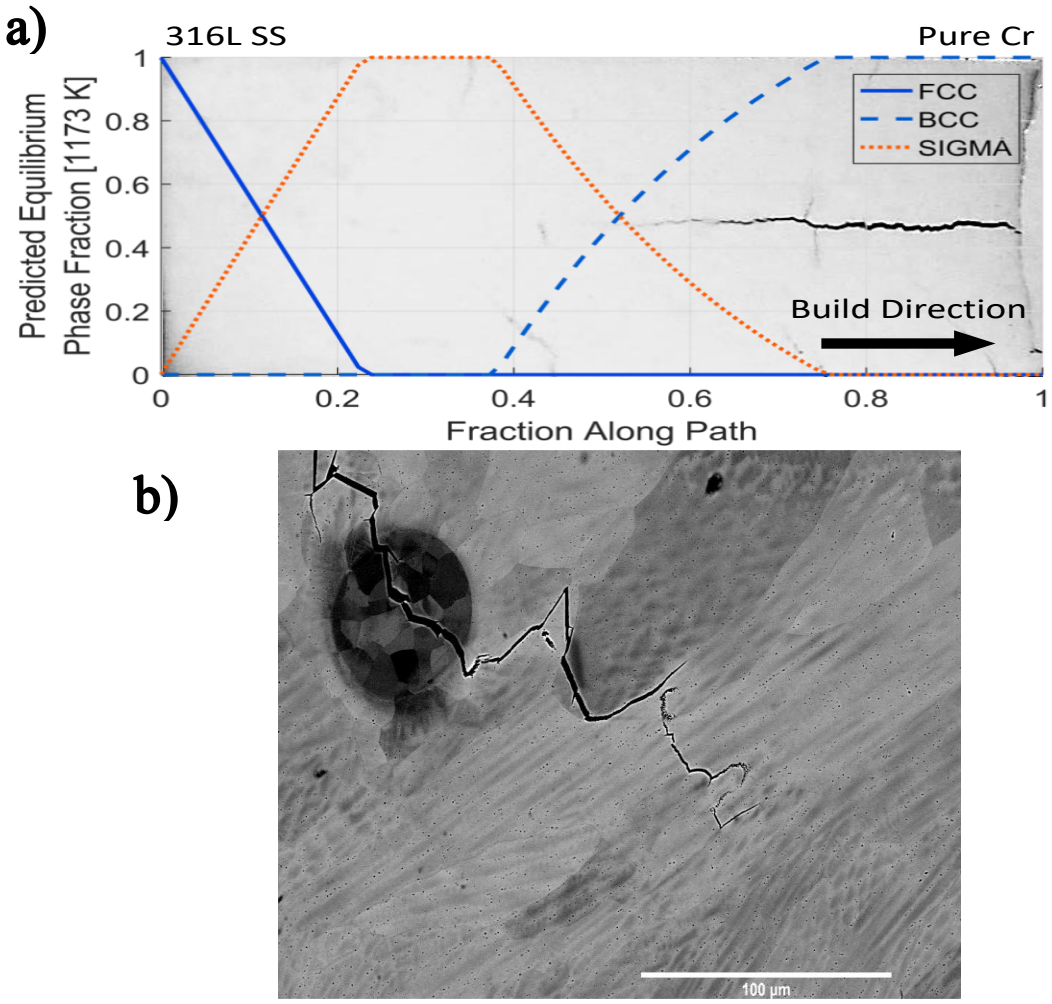

Figure 5. a) An optical image of the functionally graded sample; additively manufactured using the linear gradient path shown in Figure 4. Note the center crack that formed during the printing. Superimposed on the image is the plot of the phase fractions, predicted using CALPHAD, along the linear gradient path. b) A backscattered electron image of a crack-initiation site.

In an effort to determine if the σ phase formed during the fabrication using the linear gradient path, XRD was also conducted on the transverse cross-sections of the samples at five different locations along the composition gradient (the build direction). As shown in Figure 6, there was a clear change from FCC to BCC crystal structure as the percentage of chromium in the sample increases going from the bottom of the sample

to the top. However, it was not possible to detect any σ phase using the conventional XRD technique, as conventional XRD is typically incapable of detecting phases that exist at low volume fractions. Furthermore, it has been reported in the literature that the σ phase tends to form only upon slow cooling of the material, as the kinetics of nucleation and growth of this complex crystal structure, with a composition much different from the matrix, tends to be sluggish [25]. Since solidification in additive manufacturing is a rapid cooling process, it can be surmised that large quantities of σ phase would not have had sufficient time to form, thus preventing it from being detected in XRD.

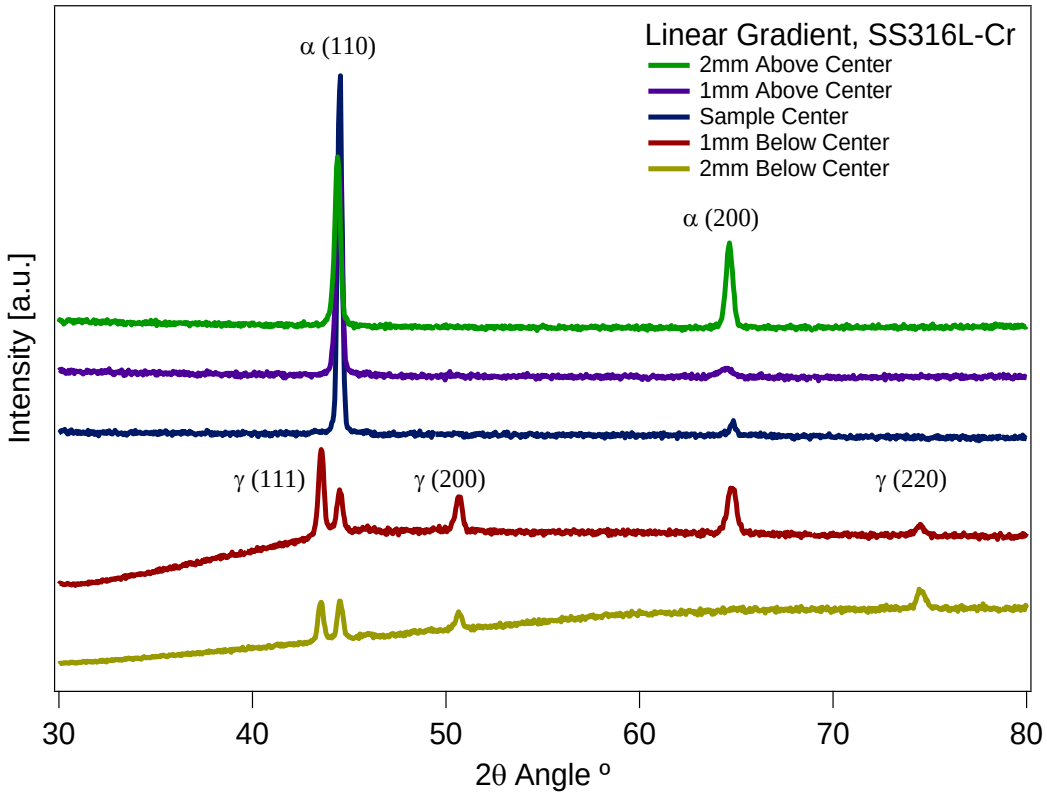

Figure 6. Room temperature XRD results of the as-printed 316L stainless steel – Chromium functionally graded sample, fabricated following the linear gradient path in Figure 4, from the bottom of the sample (near the substrate, 100% 316L stainless steel) to the top of the sample (100% chromium).

In order to find out whether nano-sized σ phase particles are present in the microstructure, TEM foils were prepared 12 mm from the top of the sample, or the location for maximum anticipated σ phase formation. The corresponding bright field TEM images and the corresponding diffraction patterns are shown in Figure 7. The bright field image (Figure 7a) shows that the microstructure consists of two phases. Selected area diffraction (SAD) patterns were recorded from both phases (Figure 7b and

c). The SAD pattern from the matrix was consistently indexed as bcc α phase, while the precipitate was indexed as fcc γ phase. σ phase was not observed in the microstructure.

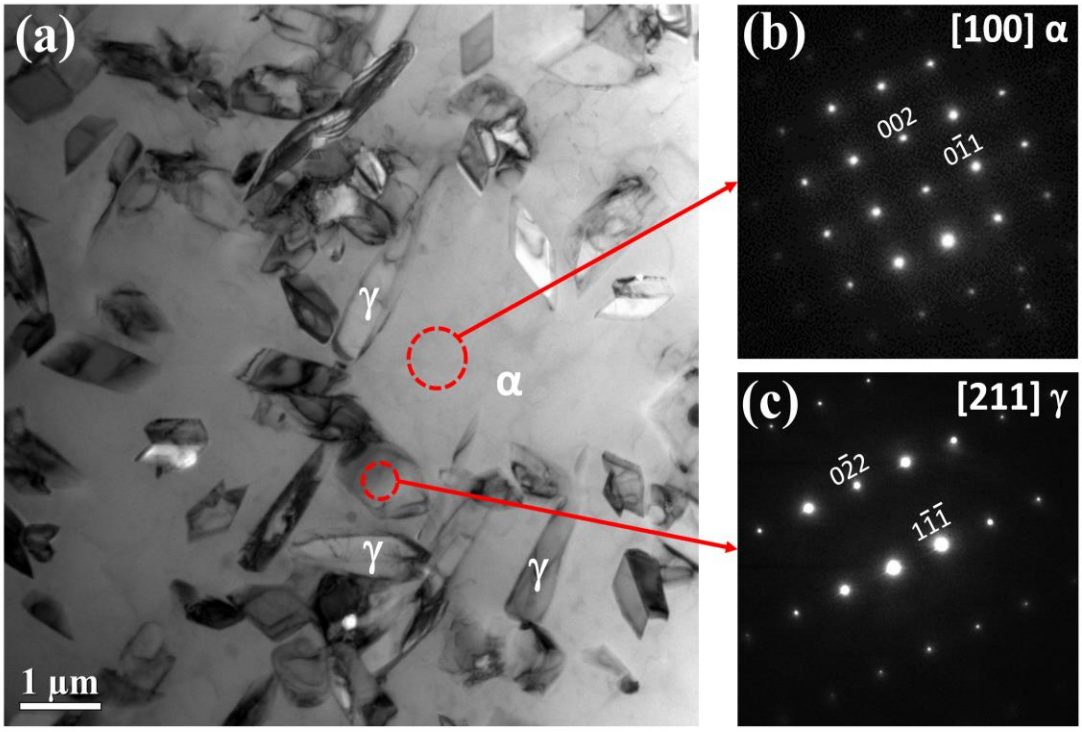

Figure 7. a) Bright field TEM image of the 316L stainless steel – chromium functionally graded sample, fabricated following the linear gradient path in Figure 4. b) Selected area diffraction (SAD) pattern of the matrix. c) SAD pattern of the precipitate phase.

It is likely that the cooling rate of the melt pool is sufficiently fast to prevent the formation of the σ phase upon AM fabrication using the present DED system. To explore this further, a series of additional TEM foils were prepared and examined from the different composition regions of the gradient sample in which the presence of σ phase was predicted by CALPHAD (near center of the gradient sample) and yet no sign of σ phase was detected in the as-printed samples. However, even if the σ phase did not form due to the long time necessary for it to nucleate and grow in appreciable amounts,

the post processing heat treatment of these samples could trigger the precipitation of σ phase, due to the composition of the center region of the sample perfectly matching that of σ phase. Therefore, the complete avoidance of σ-prone compositions is necessary.

In order to further investigate if the σ phase forms at all in the sample with the linear gradient, the as-printed sample was heat treated at 900 °C for 8 h. This heat treatment was decided by inferring the kinetics of σ formation from the TTT diagram for a duplex stainless steel (Fe-22% Cr-5% Ni-3% Mo-0,15% N-0,02% C, having a microstructure of 40–45% of ferrite and 55–60% austenite) [25]. Although the duplex steel has a lower nickel content than 316L stainless steel, it provides a rough estimate on the kinetics of the precipitation and growth of σ phase in the Fe-Ni-Cr alloy system. After the heat treatment, the XRD was performed on the heat-treated sample and showed the presence of a significant fraction of σ phase in the bottom and center portions of the linear gradient sample, as demonstrated in Figure 8.

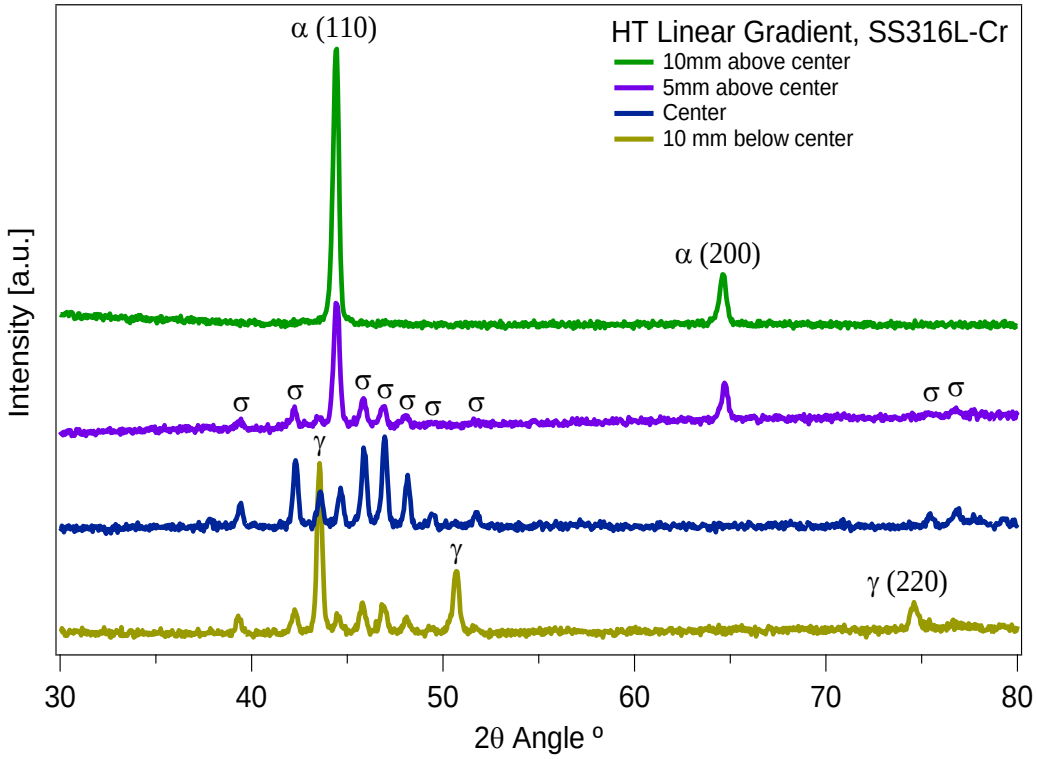

Figure 8. Room temperature XRD results of the as-printed and heat-treated 316L stainless steel – Chromium functionally graded sample, fabricated following the linear gradient path in Figure 4. The heat treatment was performed at 900 °C for 8 h in vacuum. The measurements taken from the bottom of the sample (near the substrate, 100% 316L stainless steel) to the top of the sample (100% chromium) at different distances.

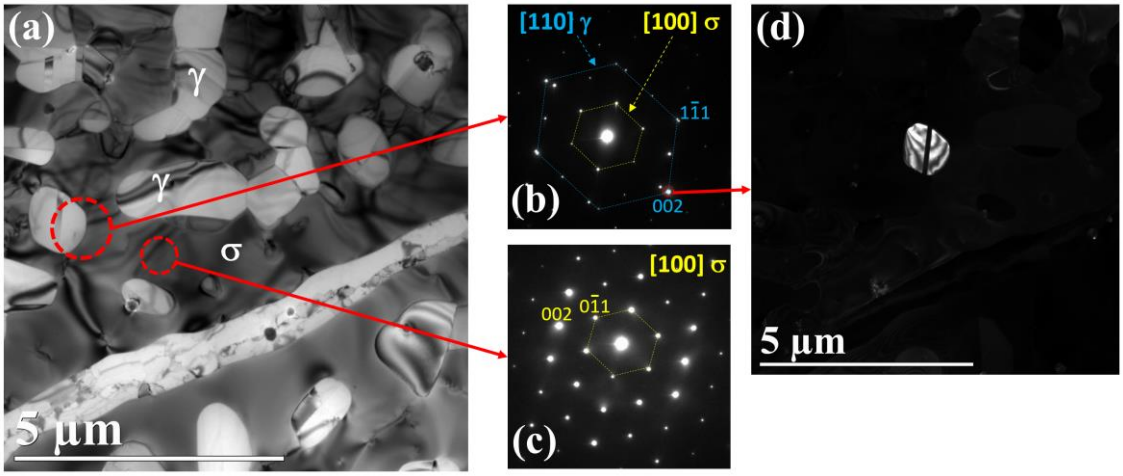

Figure 9. a) Bright field TEM image of the heat-treated 316L stainless steel – chromium functionally graded sample, fabricated following the linear gradient path in Figure 4. b) SAD pattern of the precipitate + matrix. c) SAD pattern of the matrix indicating that the matrix is the σ phase. d) Dark field image of the precipitate showing that the precipitates have FCC structure.

The existence of a large amount of σ phase in the microstructure after heat treatment was further supported though TEM investigations. Figure 9a through d shows the TEM results recorded from a foil that was prepared 5 mm from the top of the sample. The bright field image (Figure 9a) as well as the SAD patterns (Figure 9b and c) revealed that the matrix phase is the σ phase with tetragonal structure and the precipitate phase is fcc γ. Figure 9b presents a diffraction pattern recorded from a σ-γ phase boundary and the corresponding dark field image in Figure 9d is captured using the (002) γ reflection and shows a single γ phase particle.

Overall, the above results point out the fact that although σ phase kinetics do not allow it to form in the as-printed condition due to the rapid cooling of the melt pool, when subject to secondary heat treatments, the σ phase forms rapidly in large amounts. If a manufactured part were to undergo common post-processing techniques, such as hot

isostatic pressing (HIPing), for stress relief or porosity reduction, this could result in a massive σ presence in the final part. Therefore, a Functionally Graded Material created using the linear gradient path from 316L stainless steel to pure chromium would not be desirable for practical applications, as it cannot be post-processed without forming the σ phase precipitates.

In order to demonstrate the validity of the path planning methodology described above and show if σ and CrNi2 phases were completely avoided by following the planned gradient path during the fabrication or after post-processing heat treatment, a functionally graded sample was fabricated using the planned gradient path shown in Figs. 5 and 6. The planned path was simplified by identifying three linear segments that closely approximated the original planned path shown in Figure 3b. These linear compositional gradients were then programmed into to the LENS DED system to create a representation of the planned gradient path and the 12.7 × 12.7 × 12.7 mm3 sample was printed. The sample was then examined using SEM to confirm that σ phase did not appear. As with the linear gradient path, there was no evidence of σ formation in the sample. XRD was then conducted on this sample, as seen in Figure 10 (upper figure). It was again shown that there was no sign of σ phase in the as-printed condition. TEM investigations also confirmed this conclusion. The planned gradient samples then underwent the same heat treatment as the linear gradient sample. The XRD results showed that a small amount of σ phase become evident, as displayed in Figure 10 (lower figure). Even with σ phase present, its volume fraction is significantly less in the planned gradient sample than what was found in the linear gradient sample. Using the Rietveld

analysis, the volume fraction of the σ phase was determined to be 98.9% for the heat-treated linear path samples, while the volume fraction of the σ phase was only 3.5% for the heat-treated planned path samples.

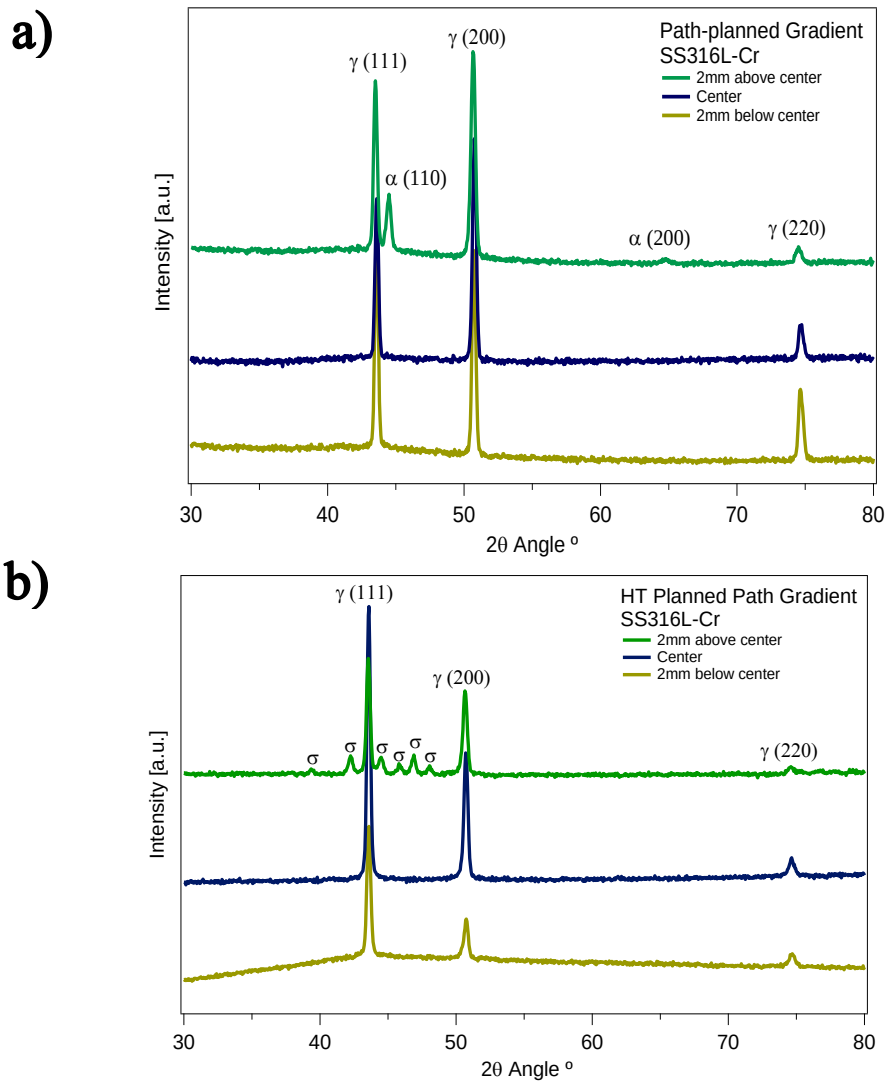

Figure 10. Room temperature XRD results of the as-printed 316L stainless steel – chromium functionally graded sample, fabricated following the planned gradient path in Figure 4, from the bottom of the sample (near the substrate) to the top of the sample (upper figure), the same sample after the secondary heat treatment (HT) at 900 °C for 8 h (lower figure).

TEM investigations summarized in Figure 11 further demonstrate the significant reduction in the σ phase content in the planned gradient sample over the linear gradient sample (Figure 9). The TEM bright field image (Figure 11a), the indexed SAD patterns (Figure 11b through d), as well as the associated dark filed image (Figure 11e), confirm that unlike the linear gradient sample, here the γ phase is the matrix and the σ phase appears in form of particles at the grain boundaries of γ phase.

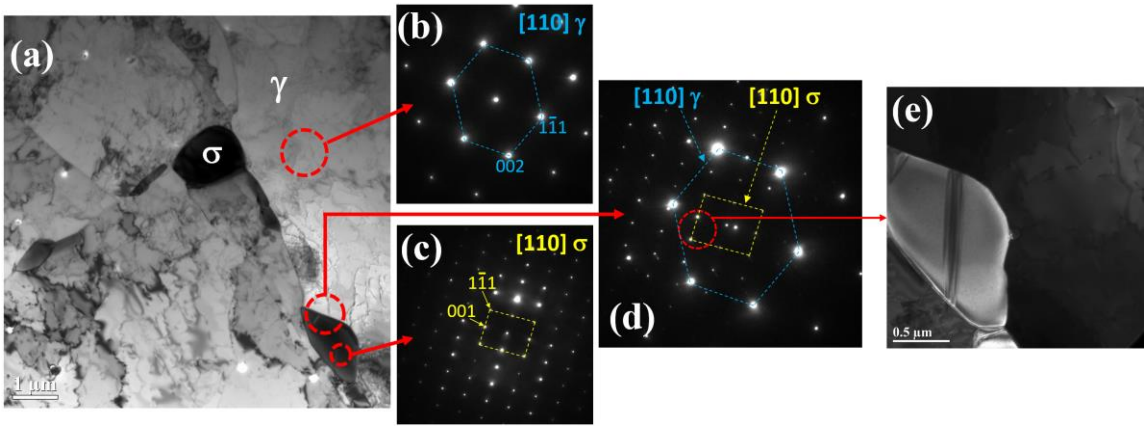

Figure 11. a) Bright field TEM image of the heat-treated 316L stainless steel – chromium functionally graded sample, fabricated following the planned gradient path in Figure 4. b) SAD pattern of the precipitate. c) SAD pattern of the matrix indicating that the matrix is the FCC phase. d) SAD pattern of the precipitate and the matrix. e) Dark field image of the precipitate showing that the precipitates are σ phase.

A closer look into these TEM images using ImageJ image analysis soft- ware revealed that the amount of the σ phase was decreased from 71.6% in the linear gradient sample to 7.46% in the planned gradient sample. This significant change indicates that even with the same heat treatment applied to both samples, the planned gradient path managed to avoid most of the σ phase composition region during the fabrication, and therefore, decrease the amount of σ phase that formed after the heat treatment.

It is still plausible, however, to ask the question of why the planned gradient path was not successful in totally eliminating the σ phase or avoiding the σ phase composition region. The cost function used was supposed to maximize the distance from the obstacles, i.e. detrimental phases, in order to avoid any surprises that may arise from issues related to initial powder variability or AM processing issues, yet the σ phase still appeared after the heat treatment, albeit in much smaller amounts as compared to the linear gradient path sample. We attributed this unexpected observation to challenges associated with the fabrication of the compositionally gradient path itself. The detailed compositional analysis using WDS demonstrated that the existence of the σ phase in the planned gradient sample was very likely because the actual deposited composition of Ni during DED printing was consistently lower than the target Ni content as determined by the path-planning algorithm. Figure 4 displays the experimentally measured compositions at different locations of the sample, clearly showing this depletion in nickel content by plotting the composition of the planned gradient as printed as well as the nominal compositions. Clearly, Ni concentration achieved in the planned gradient path sample is much lower than the target composition, providing an explanation behind the observation of the σ phase.

The reduced amount of Ni relative to the actual planned composition gradient could have been the result of the differential evaporation of nickel in the melt pool. However, the amount of nickel loss (max 5.82%) is much higher than what would be expected from the differential evaporation loss [26], [27], therefore, there must be other factors at play. It is possible that since nickel has the greatest density, the nickel powder

may not have enough pressure behind it to push it through the powder feeding system at the same speed as the other powders. Another factor that one needs to take into account is the differences in surface roughness among the powders used, which may lead to different flow rates even though preset flow rates for each powder might be the same. Regardless of which possibility is the main cause of the nickel loss, it is obvious that any effort on fabricating Functionally Graded Materials using DED AM systems should be preceded by a careful calibration study to determine the flow rates of each powder type and batch, and powder hopper, in order to accurately capture the mass deposition rate of each powder. Ongoing work by the authors is focusing on the redesign of the powder feeding system and better calibration of powder deposition parameters to attain better control over the compositions deposited in the DED system currently in use. The preliminary work on the calibration of the powder deposition parameters has been introduced below and the results are presented in Figure 12, showing a much better match between the planned and experimentally fabricated compositional gradients.

In order to calibrate the deposited mass from each of the powder hoppers, and thus, to better control the local composition and composition gradient, we created a calibration curve correlating the hopper motor rotations per minute (rpms) to the mass of the powder exiting the nozzles for each powder type.

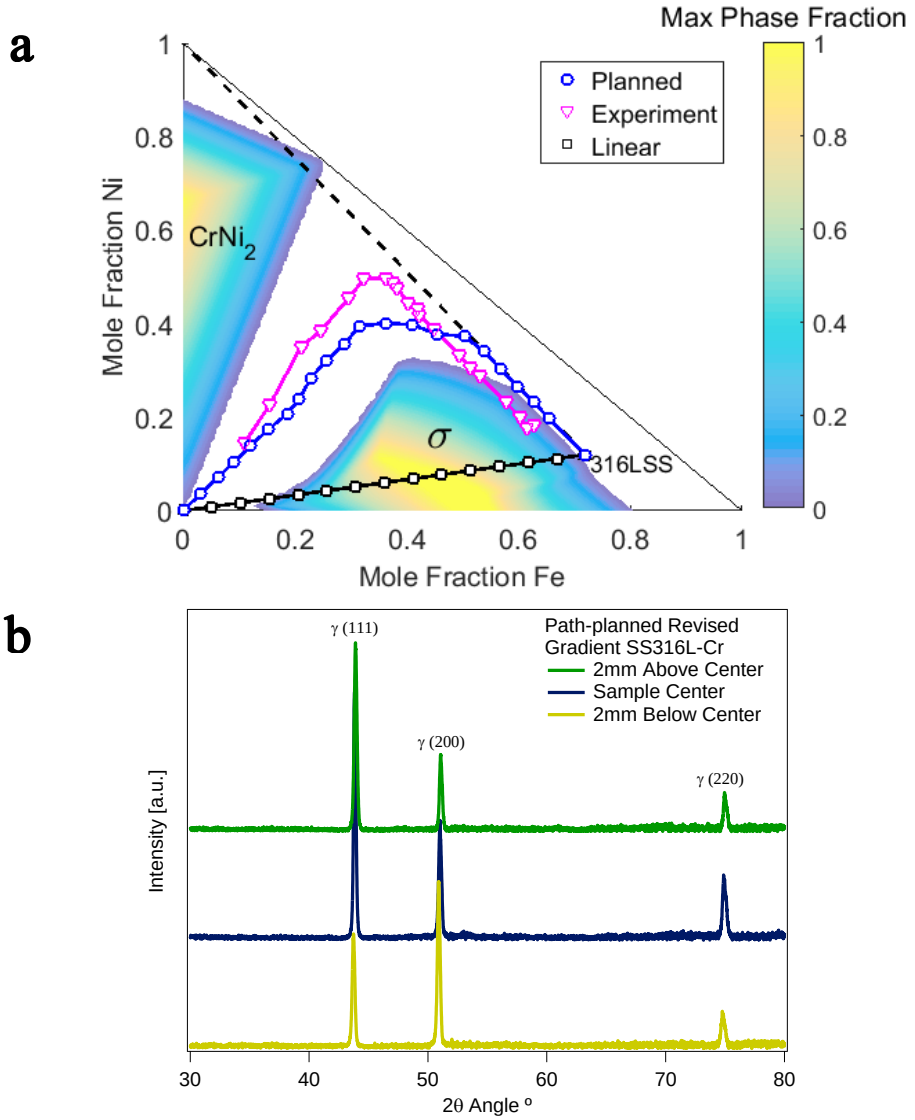

Figure 12. a) The linear gradient (the black path) as well as the nominal (the blue path) and experimental paths (the pink one) for the planned gradient are shown in the composition space for the functionally graded samples starting from 316L stainless steel and ending at pure Cr while avoiding the detrimental phases (CrNi2 and σ). The experimental planned path samples were fabricated after calibrating the powder flow rates for each type of powder to achieve the desired mass deposition rates at a given point. Note the much better match with the nominal planned path compositions, as compared to the experiments shown in Figure 4. b) Room temperature XRD results of the as-printed functionally graded sample, fabricated following the planned gradient path in Figure 4, after a better calibration of the powder flow rates for target compositions, from the bottom (near the substrate) to the top of the sample, c) the same sample after the secondary heat treatment (HT) at 900 °C, 8 h.

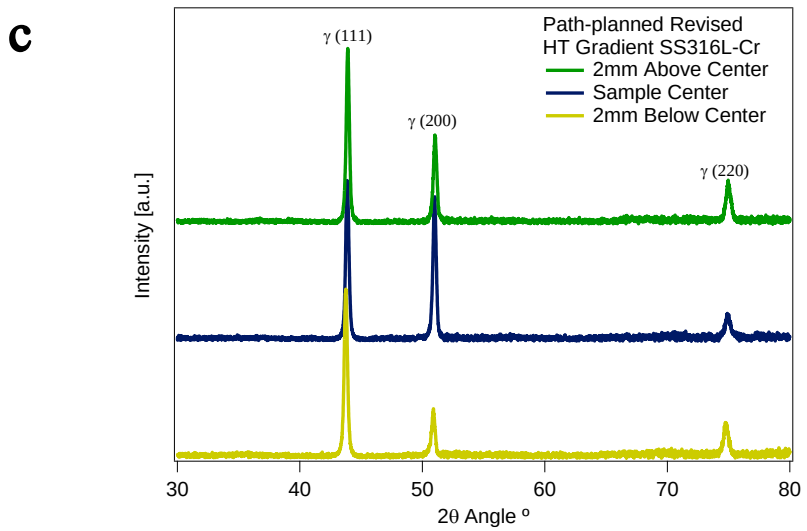

Figure 12. Continued.

We then identified the critical points of inflection from the path designed using our path planning algorithm (Figure 3b, the blue path) and determined the necessary rpms to deposit the target compositions, as described in Section 4, using the gradient path design software. Starting with the 316L stainless steel as a known standard, we deposited the path by starting at optimal rpm for the pure 316L stainless steel, then adjusted the rpms of all powders, accordingly, to maintain a constant target mass out of the nozzle at a given layer, based on the planned compositional gradient. This methodology resulted in a measured compositional gradient in the designed path, much closer to the planned composition gradient (Figure 12a), and eventually, led to the complete elimination of the σ phase in the heat-treated samples as seen in Figure 12c

The presence of detrimental phases is a significant issue in the fabrication of functionally graded alloys. A new algorithmic methodology for designing functional gradients that avoids detrimental phases is presented. This methodology was

experimentally validated by planning and 3-D printing a gradient from 316L stainless steel to pure chromium. Gradient samples were successfully printed using a multi-material direct energy deposition system with optimized processing parameters. The samples fabricated using the planned gradient and a linear gradient were characterized to identify their compositions and phases before and after secondary heat treatments. The presence of detrimental σ phase after the heat treatment (900 °C for 8 h) in the planned gradient sample was shown to be significantly less than the amount of σ phase detected in the heat-treated linear gradient sample. The as-printed planned gradient was determined to have less nickel content than what was planned. This difference in composition was attributed to the combination of differential evaporation and inconsistencies in powder flowability. Efforts to reduce the observed deviation in the printed composition from the planned gradient include modifications to the powder flow system of the printer and more rigorous flow calibration techniques. The preliminary work on the better calibration of powder flow rates to achieve target mass deposition rates and local compositions resulted in the fabrication of the planned gradient samples with much closer compositions to the planned values and the complete elimination of the σ phase, demonstrating the success of the proposed methodology.

By embodying a gradient design methodology algorithmically, there are numerous opportunities to design previously unknown gradient materials. While the present work demonstrates the methodology in a three-element system (Fe-Ni-Cr), there is no formal limit to the dimensionality of designed gradients. As such, more complicated FGMs could be designed that were previously impossible to fabricate due to

the inability to visualize detrimental phase regions. The ability to optimize gradient paths to a cost function also enables gradients to be designed for optimal properties like hardness, strength, or heat dissipation. The uncertainties in printed compositions and CALPHAD phase predictions could also be accounted for computationally to design more robust functional gradients.

2.4. Summary and Conclusion

The presence of detrimental phases is a significant issue in the fabrication of functionally graded alloys. A new algorithmic methodology for designing functional gradients that avoids detrimental phases is presented. This methodology was experimentally validated by planning and 3-D printing a gradient from 316L stainless steel to pure chromium.

Gradient samples were successfully printed using a multi-material direct energy deposition system with optimized processing parameters. The samples fabricated using the planned gradient and a linear gradient were characterized to identify their compositions and phases before and after secondary heat treatments. The presence of detrimental σ phase after the heat treatment (900 °C for 8 h) in the planned gradient sample was shown to be significantly less than the amount of σ phase detected in the heat-treated linear gradient sample. The as-printed planned gradient was determined to have less nickel content than what was planned. This difference in composition was attributed to the combination of differential evaporation and inconsistencies in powder flowability. Efforts to reduce the observed deviation in the printed com- position from the planned gradient include modifications to the powder flow system of the printer and

more rigorous flow calibration techniques. The preliminary work on the better calibration of powder flow rates to achieve target mass deposition rates and local compositions resulted in the fabrication of the planned gradient samples with much closer compositions to the planned values and the complete elimination of the σ phase, demonstrating the success of the proposed methodology.

By embodying a gradient design methodology algorithmically, there are numerous opportunities to design previously unknown gradient materials. While the present work demonstrates the methodology in a three-element system (Fe-Ni-Cr), there is no formal limit to the dimensionality of designed gradients. As such, more complicated FGMs could be designed that were previously impossible to fabricate due to the in- ability to visualize detrimental phase regions. The ability to optimize gradient paths to a cost function also enables gradients to be designed for optimal properties like hardness, strength, or heat dissipation. The uncertainties in printed compositions and CALPHAD phase predictions could also be accounted for computationally to design more robust functional gradients.

2.5. References

[1] D.C. Hofmann, J. Kolodziejska, S. Roberts, R. Otis, R.P. Dillon, J.-O. Suh, Z.-K. Liu, J.-P. Borgonia, Compositionally graded metals: a new frontier of additive manufacturing, J. Mater. Res. 29 (2014) 1899–1910.

[2] A. Reichardt, R.P. Dillon, J.P. Borgonia, A.A. Shapiro, B.W. McEnerney, T. Momose, P. Hosemann, Development and characterization of Ti-6Al-4V to 304L stainless steel gradient components fabricated with laser deposition additive manufacturing, Mater. Des. 104 (2016) 404–413.

[3] B.E. Carroll, R.A. Otis, J.P. Borgonia, J. Suh, R.P. Dillon, A.A. Shapiro, D.C. Hofmann, Z. K. Liu, A.M. Beese, Functionally graded material of 304L stainless steel and Inconel 625 fabricated by directed energy deposition: characterization and thermodynamic modeling, Acta Mater. 108 (2016) 46–54.

[4] L.D. Bobbio, R.A. Otis, J.P. Borgonia, R.P. Dillon, A.A. Shapiro, Z.-K. Liu, A.M. Beese, Additive manufacturing of a functionally graded material from Ti-6Al-4V to Invar: experimental characterization and thermodynamic calculations, Acta Mater. 127 (2017) 133–142.

[5] S. Tammas-Williams, I. Todd, Design for additive manufacturing with site-specific properties in metals and alloys, Scr. Mater. 135 (2017) 105–110, https://doi.org/10.1016/j.scriptamat.2016.10.030.

[6] D.C. Hofmann, S. Roberts, R. Otis, J. Kolodziejska, R.P. Dillon, J. Suh, A.A. Shapiro, Z.-K. Liu, J.-P. Borgonia, Developing gradient metal alloys through radial deposition additive manufacturing, Sci. Rep. 4 (2014) 5357.

[7] J. Wang, Z. Pan, Y. Ma, Y. Lu, C. Shen, D. Cuiuri, H. Li, Characterization of wire arc additively manufactured titanium aluminide functionally graded material: microstructure, mechanical properties and oxidation behavior, Mater. Sci. Eng. A 734 (2018) 110–119, https://doi.org/10.1016/j.msea.2018.07.097.

[8] Y. Zhang, Z. Wei, L. Shi, M. Xi, Characterization of laser powder deposited Ti–TiC composites and functional gradient materials, J. Mater. Process. Technol. 206 (2008) 438–444, https://doi.org/10.1016/j.jmatprotec.2007.12.055.

[9] C. Shen, Z. Pan, D. Cuiuri, J. Roberts, H. Li, Fabrication of Fe-FeAl functionally graded material using the wire-arc additive manufacturing process, Metall. Mater. Trans. B Process Metall. Mater. Process. Sci. 47 (2016) 763–772, https://doi.org/10.1007/s11663-015-0509-5.

[10] A.A. Askadskii, L.M. Goleneva, E.S. Afanas'ev, M.D. Petunova, Gradient polymeric materials, Rev. J. Chem. 2 (2012) 105–152, https://doi.org/10.1134/S207997801202001X.

[11] F. Momeni, S. M.Mehdi Hassani.N, X. Liu, J. Ni, A review of 4D printing, Mater. Des. 122 (2017) 42–79, https://doi.org/10.1016/j.matdes.2017.02.068.

[12] G. Hilmas, Innovative technique for rapidly prototyping parts of polymers, metals, ceramics, composites, and functionally graded materials, Mater. Technol. 11 (1996) 226–228, https://doi.org/10.1080/10667857.1996.11752706.

[13] M. Yin, L. Xie, W. Jiang, G. Yin, Design and fabrication of integrated micro/macro- structure for 3D functional gradient systems based on additive manufacturing, Opt. Commun. 414 (2018) 195–201, https://doi.org/10.1016/j.optcom.2017.12.088.

[14] D. Nuvoli, V. Alzari, J.A. Pojman, V. Sanna, A. Ruiu, D. Sanna, G. Malucelli, A. Mariani, Synthesis and characterization of functionally gradient materials obtained by frontal polymerization, ACS Appl. Mater. Interfaces 7 (2015) 3600–3606, https://doi.org/10. 1021/am507725k.

[15] A. Hinojos, J. Mireles, A. Reichardt, P. Frigola, P. Hosemann, L.E. Murr, R.B. Wicker, Joining of Inconel 718 and 316 Stainless Steel using electron beam melting additive manufacturing technology, Mater. Des. 94 (2016) 17–27, https://doi.org/10.1016/j. matdes.2016.01.041.

[16] R. Banerjee, P.C. Collins, D. Bhattacharyya, S. Banerjee, H.L. Fraser, Microstructural evolution in laser deposited compositionally graded α/β titanium-vanadium alloys, Acta Mater. 51 (2003) 3277–3292, https://doi.org/10.1016/S1359-6454(03)00158- 7.

[17] P.C. Collins, R. Banerjee, S. Banerjee, H.L. Fraser, Laser deposition of compositionally graded titanium–vanadium and titanium–molybdenum alloys, Mater. Sci. Eng. A 352 (2003) 118–128, https://doi.org/10.1016/S0921-5093(02)00909-7.

[18] T. Borkar, V. Chaudhary, B. Gwalani, D. Choudhuri, C.V. Mikler, V. Soni, T. Alam, R. V. Ramanujan, R. Banerjee, A combinatorial approach for assessing the magnetic properties of high entropy alloys: role of Cr in AlCoxCr1–xFeNi, Adv. Eng. Mater. 19 (2017), 1700048. https://doi.org/10.1002/adem.201700048.

[19] L. Kaufman, J. Agren, CALPHAD, first and second generation–birth of the materials genome, Scr. Mater. 70 (2014) 3–6.

[20] L. Kaufman, H. Bernstein,Computer calculation of phase diagrams with special reference to refractory metals. New York: Academic Press, 1970.

[21] T. Kirk, E. Galvan, R. Malak, R. Arroyave, Computational design of gradient paths in additively manufactured functionally graded materials, J. Mech. Des. (2018) https://doi.org/10.1115/1.4040816.

[22] S. Karaman, E. Frazzoli, Sampling-based algorithms for optimal motion planning, Int. J. Robot. Res. 30 (2011) 846–894.

[23] O. Adiyatov, H.A. Varol, Rapidly-exploring random tree based memory efficient motion planning, Mechatron. Autom. ICMA 2013 IEEE Int. Conf. On 2013, pp. 354–359, https://doi.org/10.1109/ICMA.2013.6617944.

[24] P. Raja, S. Pugazhenthi, Optimal path planning of mobile robots: a review, Int. J. Phys. Sci. 7 (2012) 1314–1320.

[25] T. Lozano-Pérez, M.A. Wesley, An algorithm for planning collision-free paths among polyhedral obstacles, Commun. ACM 22 (1979) 560–570.

[26] Y.K. Hwang, N. Ahuja, Gross motion planning—a survey, ACM Comput. Surv. CSUR 24 (1992) 219–291.

[27] M. Elbanhawi, M. Simic, Sampling-based robot motion planning: a review, IEEE Access 2 (2014) 56–77.

[28] E. Masehian, D. Sedighizadeh, Classic and heuristic approaches in robot motion planning-a chronological review, World Acad. Sci. Eng. Technol. 23 (2007) 101–106.

[29] J.-O. Andersson, T. Helander, L. Höglund, P. Shi, B. Sundman, Thermo-Calc & DICTRA, computational tools for materials science, Calphad 26 (2002) 273–312.

[30] E. Galvan, R.J. Malak, S. Gibbons, R. Arroyave, A constraint satisfaction algorithm for the generalized inverse phase stability problem, J. Mech. Des. 139 (2017), 011401.

[31] A. Abu-Odeh, et al., Efficient exploration of the High Entropy Alloy composition- phase space, Acta Mater. 152 (2018) 41–57 Jun.

[32] D.M. Tax, R.P. Duin, Support vector domain description, Pattern Recogn. Lett. 20 (1999) 1191–1199.

[33] V. Vapnik, The Nature of Statistical Learning Theory, Springer, New York, 1995.

[34] B. Schölkopf, A.J. Smola, Learning with Kernels: Support Vector Machines, Regularization, Optimization, and beyond, MIT Press, Cambridge, MA, 2002.

[35] C.-C. Hsieh, W. Wu, Overview of intermetallic sigma (σ) phase precipitation in stain- less steels, ISRN Metall. 2012 (2012).

[36] H. Mao, H.-L. Chen, Q. Chen, TCHEA1: a thermodynamic database not limited for “high entropy” alloys, J. Phase Equilibria Diffus. 38 (2017) 353–368.

[37] H.-L. Chen, H. Mao, Q. Chen, Database development and Calphad calculations for high entropy alloys: challenges, strategies, and tips, Mater. Chem. Phys. 210 (2018) 279–290, https://doi.org/10.1016/j.matchemphys.2017.07.082.

[38] R. Magnabosco, Kinetics of σ phase formation in a Duplex Stainless Steel, Mater. Res. 12 (3) (2009) 321–327 Sep.

[39] B.E. Franco, J. Ma, B. Loveall, G.A. Tapia, K. Karayagiz, J. Liu, A. Elwany, R. Arroyave, I. Karaman, A sensory material approach for reducing variability in additively manufactured metal parts, Sci. Rep. 7 (2017), 3604. https://doi.org/10.1038/ s41598-017-03499-x.

[40] J. Ma, B. Franco, G. Tapia, K. Karayagiz, L. Johnson, J. Liu, R. Arroyave, I. Karaman, A. Elwany, Spatial control of functional response in 4D-printed active metallic structures, Sci. Rep. 7 (2017), 46707. https://doi.org/10.1038/srep46707.

3. PRINTING METHODOLOGY FOR FUNCTIONALLY GRADING IRON ALLOYS TO REFRACTORY METALS

3.1. Introduction

Refractory alloys are often challenging to mold and weld let alone additively manufacture [1], [2]. Their high brittleness, high melting point, and tendency to form secondary phases, makes printing challenging [3], [4]. However, their high melting point and resistance to neutron corrosion make them an optimal choice for many high heat and nuclear applications [5], [6]. On the other side of the spectrum, steel alloys do not possess high heat or radiation corrosion resistances but are generally malleable and well-studied for additive [7]–[9]. Each of these materials has been used in nuclear applications for different purposes: refractories in reactor-facing components that experience extreme temperatures [10], [11], and steels in adjacent heat sinks or other structural components [12], [13]. Given their prevalence, joints between these materials are commonly necessary, but large differences in material composition and properties introduce significant issues with traditional joining techniques [14].

The most common technique for joining these two materials is brazing [15]–[17]. This technique will join the two metals together, but it is often seen that the brazed joined will produce brittle phases without interlayers or is more prone to failure under thermal cycling due to the buildup of thermal stresses [18], [19]. Furthermore, any discrete boundary between these materials produces large discontinuities in properties like thermal expansion, which produce significant stress concentrations and can lead to cracking [14], [20]. Researchers have proposed using discrete interlayer materials (e.g.

V, Ni, Nb) to reduce these drastic changes in properties, but lesser discontinuities persist in these materials, and brittle phases, like intermetallic compounds, are also prevalent [14], [21]–[24]. These problems prohibit the production of structurally sound components, especially in critical, risk-averse applications like nuclear energy. To circumvent these problems, we propose employing a continuous compositional gradient between a refractory alloy and steel to produce functionally graded parts suitable for these applications.

The design of compositional functional gradients in metals can experience a number of the same problems seen in brazing and welding. For example, the formation of deleterious phases (e.g. sigma, laves, intermetallics) is common in the linear gradient path between arbitrary compositions [25]. The presence of these phases can lead to brittle regions or large mismatches in thermal expansion, both of which have been shown to produce catastrophic cracking during the additive manufacturing process. [26]–[29]. The additive manufacturing process imposes certain printability requirements on solidification range, solidus temperature, and hot cracking susceptibility that must be met by every composition in the gradient path if the material is to be successfully printed.

Kirk et al. [30] have developed a computational methodology to design compositionally graded alloys that avoid the issues of phase formation. The methodology is capable of planning paths in high dimensional spaces and can optimize paths for a cost function. This methodology has been validated by designing and printing a functional gradient from 316L stainless steel to pure chromium [31]. Both the planned

gradient and a simple linear gradient were printed and characterized to determine composition and phase amount after heat treatment. The planned gradient was able to eliminate the detrimental sigma phase after heat treatment demonstrating the success of the methodology.

In this work, the techniques presented in Eliseeva et al. [31] are employed to design and print a novel gradient from Fe9Cr to W. This system differs from prior work in that the number of elements is increased, increasing the space dimensionality and thus the time and complexity of both the design and manufacturing processes. In addition, the gradient design problem poses several unique but critical manufacturing challenges. There is a dramatic melting point difference of 2000C degrees between W and other constituent elements (Fe, Cr), which complicates the melting process and introduces issues such as vaporization, balling, or hot tearing [22], [24]. To address these issues, special consideration for the manufacturing process was added to the design methodology and the design of the manufacturing process itself had to consider and overcome all of these challenges.

3.1.1. Path Simplification

After analyzing the results of the path planning algorithm seen in Appendix B, the optimal path was simplified to make experimentation easier and to maximize separation from constraint boundaries. To simplify the path, excess W was removed from the first half of the path and excess Fe and Al were removed from the second half of the path, then compositions were linearized where possible. The simplified path is shown in Figure 343. The simplified path begins by traversing the Fe-Cr-Al ternary from

Fe9Cr to pure Cr and then simply following the Cr-W binary from pure Cr to pure W. This path lies on the exactly on the edges and boundaries of the Fe-Cr-W-Al composition space and, as such, is impossible to discover via uniform random sampling of Fe, Cr, W, and Al. For a path planning algorithm to discover such a path, it would need to sample the lower dimensional subspaces (i.e. ternary and binary regions) directly.

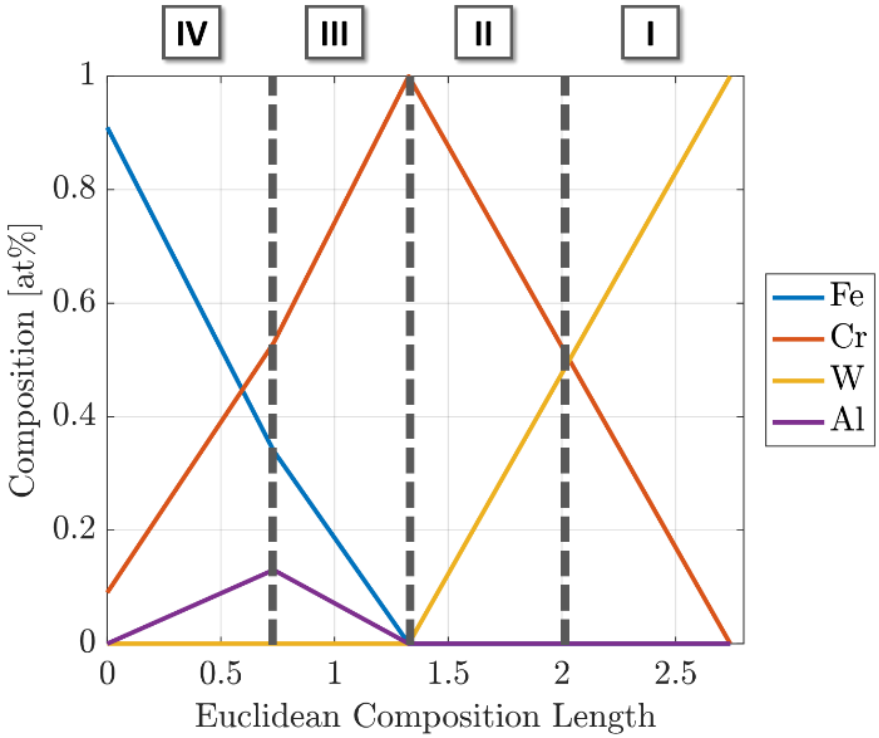

Figure 13. The optimal path (shown in Figure 37a) simplified for experimentation. Five critical compositions were identified and used to divide the path into four linear gradient regions for experimental reference.

The phase fractions along the simplified path at various temperatures are shown in Figure 344. These plots show no deleterious phases at any of the selected temperatures. This is a significant improvement over the original optimal path, which showed up to 0.50 mole fraction of mu phase and up to 0.10 of laves. However, this

simplified path is about 25% longer than the original path, indicating it is suboptimal to the original optimal path with respect to its problem formulation.

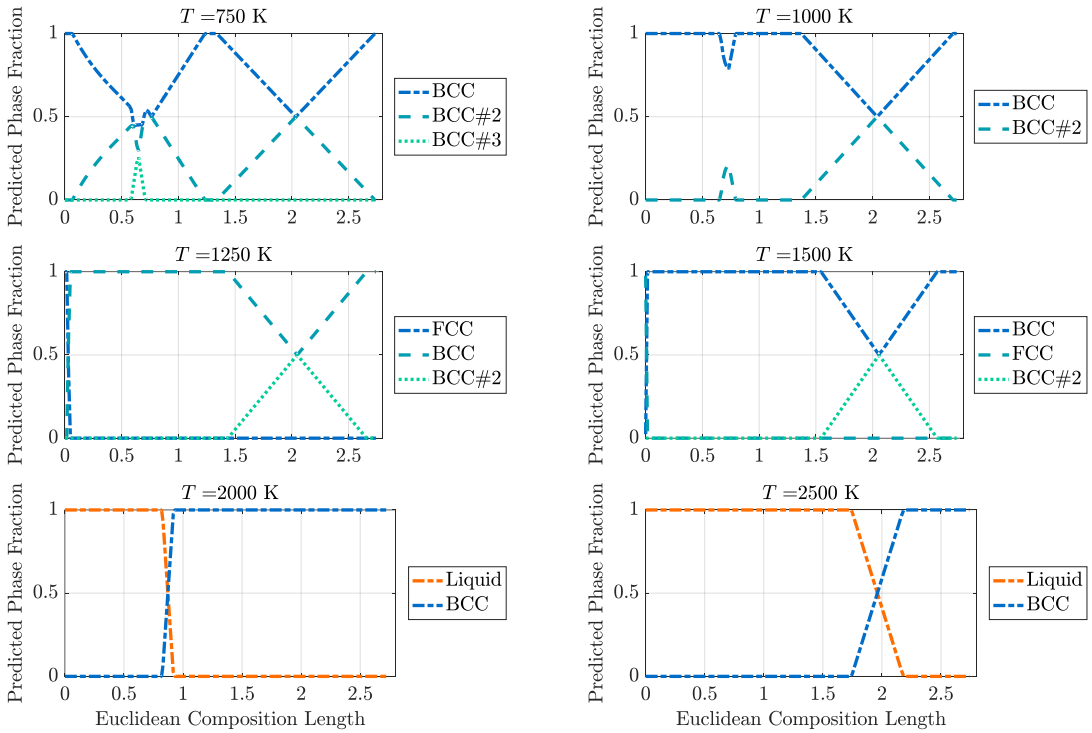

Figure 14. Equilibrium phase fractions along the simplified path (shown in Figure 13) at various temperatures. Phases are numbered by descending phase fraction when multiple phases of the same structure are present. Consequently, phase numbering is not necessarily consistent with phase constitution.

3.2. Experimental Methodology

In order to print the compositions defined by the planned path shown in Figure 13, a standard methodology was created as shown in Figure 15.

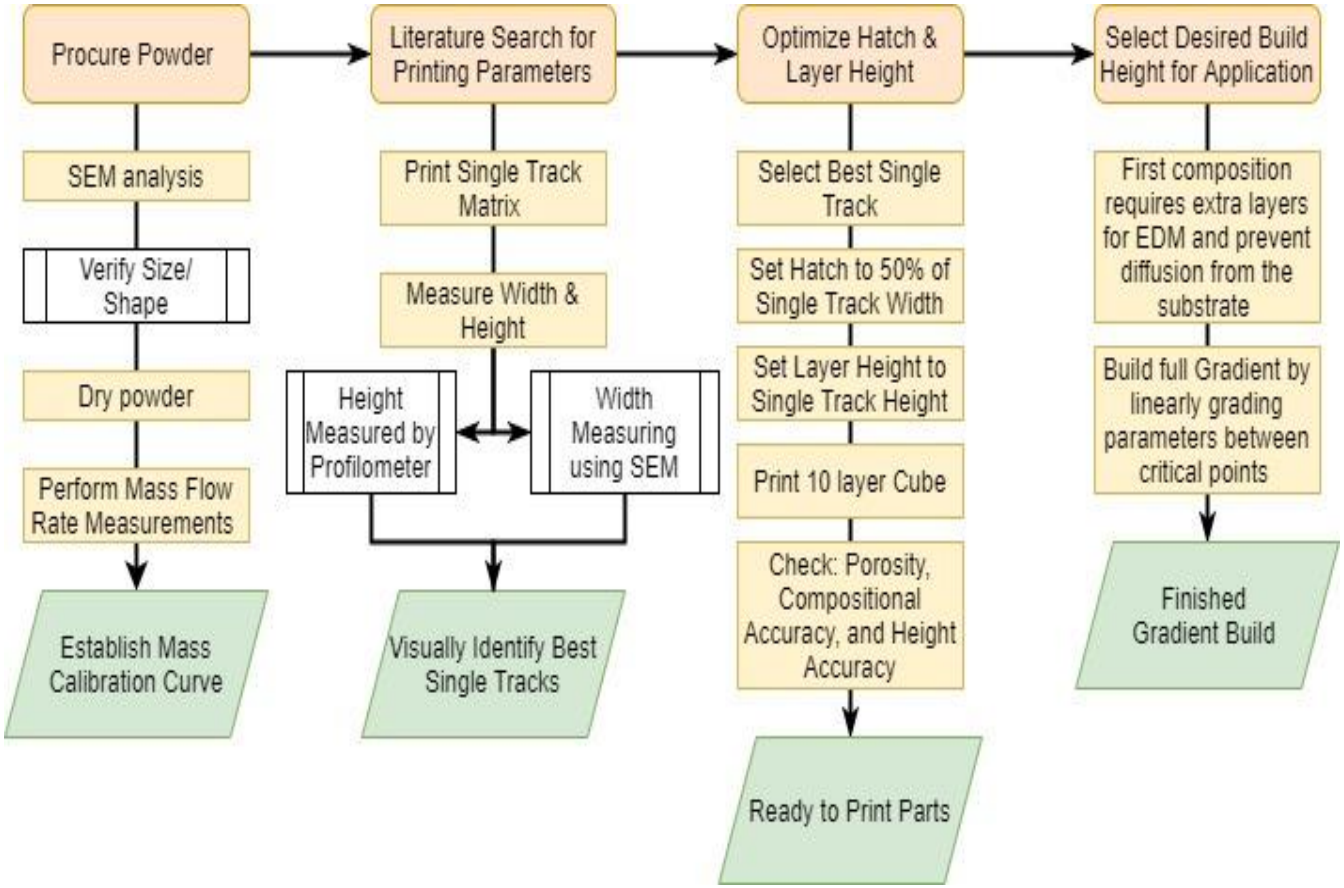

Figure 15. Flow chart of steps required to manufacture a functional gradient

This methodology allows for the simultaneous printing of materials with a large range of melting points and allows for smooth transitions between parameter sets. First the corresponding powders for the planned path were procured: commercially pure Fe, pure Cr, Al6061, and pure W, as shown Table 1. The sizes and distribution were provided by the companies the powders were received from.

Table 1. Powder Properties Used for Printing

Powder	Provider	Size range	Manufacturing process
Fe	TLS	45-100um	N atomized
Cr	TLS	45-100um	Ar atomized
W	Tekmat	45-90um	Inert gas atomized
Al6061	Valimet	40-100um	Inert gas atomized

These powders were then dried for 8h at 100C in an inert Ar environment to eliminate any trace moisture. The dry powders were then assigned to one of four powder feeders. Powder mass flow rates for each powder were then determined by collecting a sample of power for 30 seconds at a predetermined feeder rotation speed. Test were conducted at after stead flow was achieved at each speed, approximately 20 seconds. Figure 16, summarizes the powder mass flow rates for all powders used in this study as a function of the feeder rotation speed. The desired critical compositions from the planed path were then converted to weight percentage, which was used with the calibration

curves to calculate a constant relative volume of powder under the laser beam for each critical composition. This kept the amount of powder flowing out of the powder nozzles constant and allowed for the weld pool volume to remain constant. This constancy in weld pool volume allowed a variable to be removed when comparing the width and heights of the weld pools and allow for more consistent prints.

Following the calibration of the powder flow rates, an Optomec LENS® MR-7 direct energy metal deposition system with 4 powder feeders and a 1000W, 1060nm laser was used to print 13 mm single tracks of the critical compositions. The laser power and laser line speeds were varied systematically based on literature values. These single tracks were inspected with a scanning electron microscope (SEM) for uniformity in track height and width, the absence of other traditionally recognized additive manufacturing (AM) defects (lack of fusion and balling), consistent curvature of solidification front, and good fusion to the substrate. As shown in Figure 17 only single tracks that met all the criteria were selected for the next step. The acceptable single tracks were then measured for width with an SEM and height with a profilometer to determine hatch spacing between laser scan lines and a starting layer height at each critical composition point.

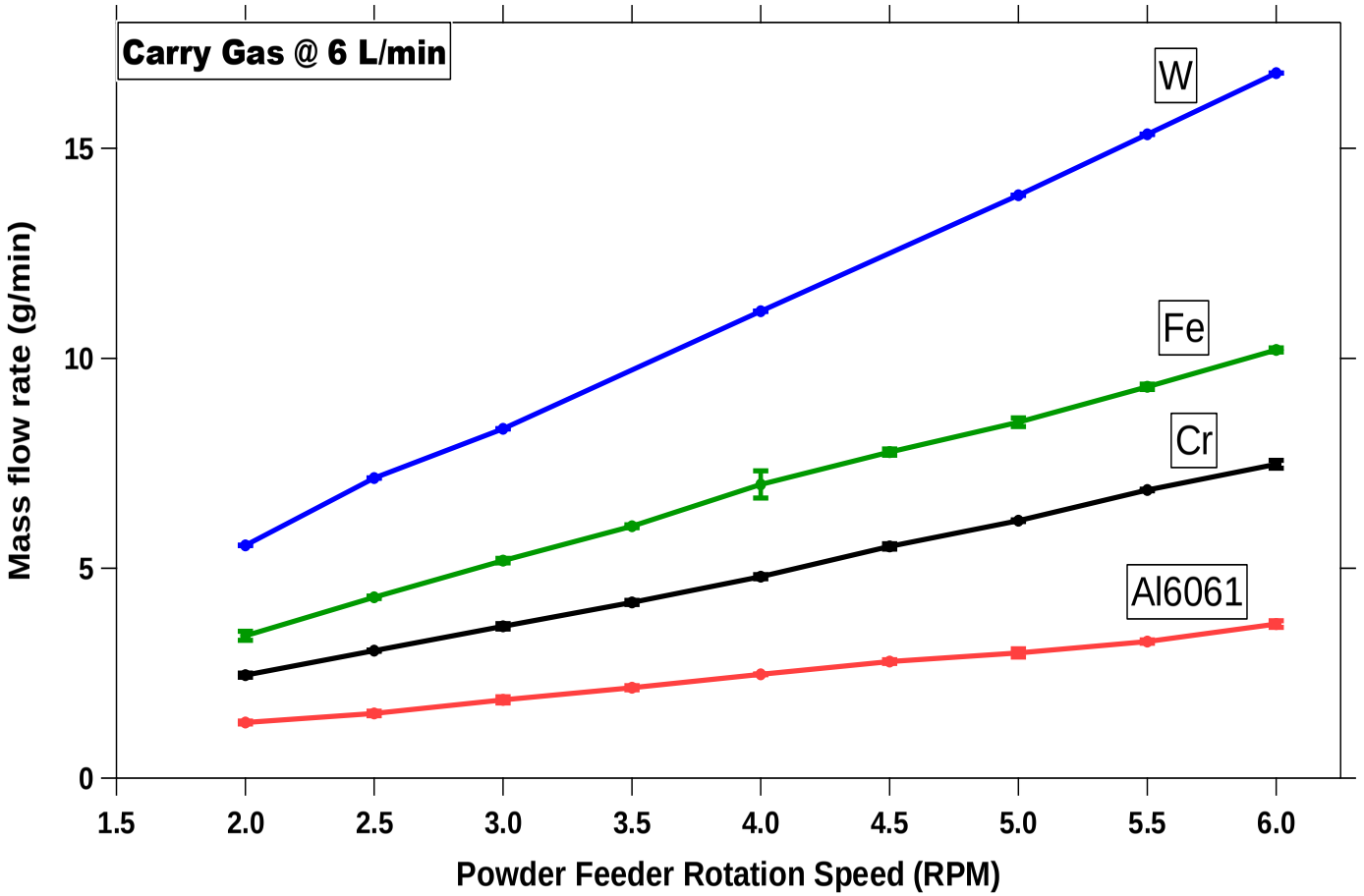

Figure 16. Mass flow rates for each powder (Fe, Cr, W, and Al6061) used in this study in different powder feeders as a function of the powder feeder rotation speed. Carry gas flow rate refers to the gas flow that carry the powder along the feeder lines. This rate was kept constant throughout all the experiments.

After completing the study of the single tracks, 10-layer thin square prisms were fabricated using the most viable set of single tracks. The heights of the 10-layer prisms were measured to find the average layer height achieved for each combination of laser power, laser line speed, and chosen hatch spacing, and then the average as compared to the initially programmed layer height. Figure 18, displays Fe9Cr 10-layer cube changes in average measured layer height as a function of programmed layer height. Note that if the programmed layer height is significantly different than the actual deposited layer height, the laser beam diameter at the focal point will continuously change with the increasing number of layers deposited and may cause significant printing failures.

Using the measured average layer height as the new programmed layer height, the prisms were printed again, and this iterative process continued until the programmed total height matched the printed part height; allowing the focal length of the laser to remain consistent throughout the build. Once this step is completed, the hatch spacing can be adjusted, if required, to increase the density of the build. This process not only allowed for the build to achieve the desired height but also for the gradient to be as accurate as possible.

a

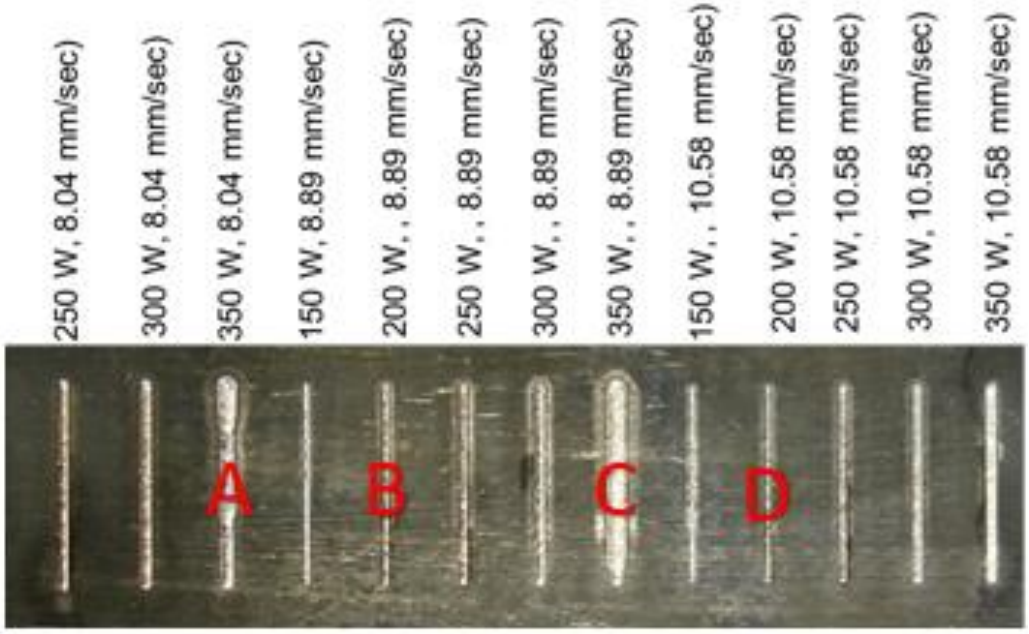

b

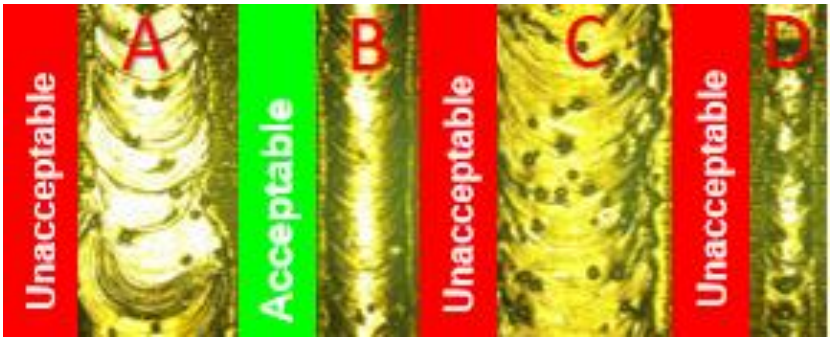

Figure 17. (a) Selected single tracks of Cr printed using the DED system with the power and speed combinations shown. The four tracks in (b) are from the red boxes in (a) displaying the classification of acceptable and unacceptable tracks. A is an example for non-uniform track width; B: Acceptable, good track; C: Uneven solidification front and spatter particles; D: Lack of sufficient fusion to the substrate.

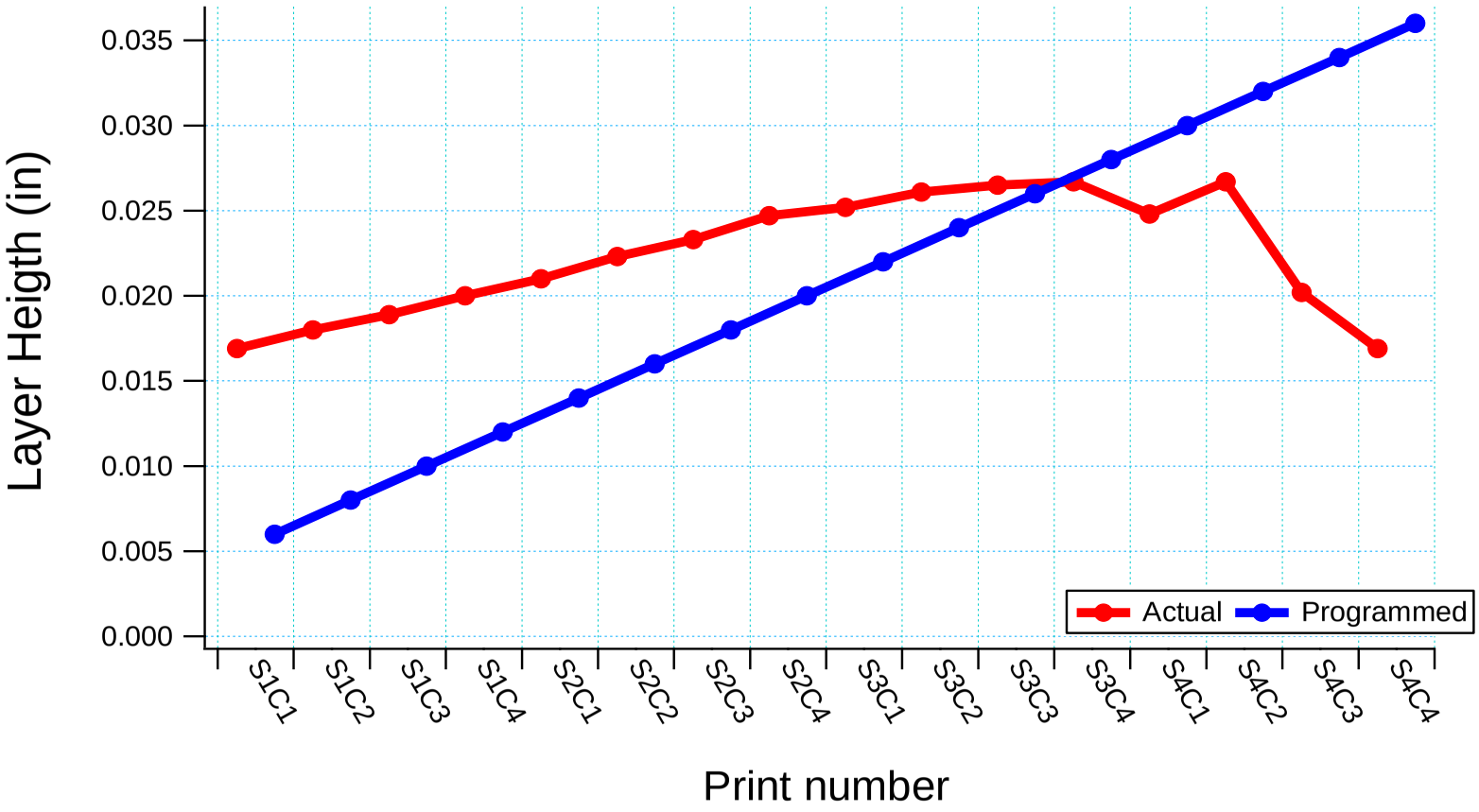

Figure 18. Example of an iterative process for optimization of layer height for printing a given powder composition by changing the programmed layer height and hatch spacing. Demonstrating how the programmed and actual average layer height converge and then diverge as laser height is adjusted.

Next, the critical compositions were combined using linear composition grading. The small gradients were printed using the parameters established in the previous steps. These samples were sliced into 2mm sections with wire electrical discharge machining (EDM) parallel to the built direction such that each sample includes all layers of the gradient. The 2mm thick slices of each graded sample were then embedded in an epoxy mount and mechanically polished down to a 0.05 μm surface finish, first using Si carbide paper from 600 grit to 1200 grit, followed by diamond paste polishing from 6 μm to 0.05 μm. These slices were examined with Phenom XL G2 Desktop SEM equipped with Energy Dispersive Spectroscopy (EDS). The phase structures of the gradient samples were then determined using a Bruker-AXS D8 X-ray diffractometer with Cu Kα (wavelength λ =0.154 nm) radiation. A more in-depth look into composition was done using Cameca SX Five Electron Microprobe Analyzer (EPMA) using wavelength dispersive spectroscopy (WDS), operated at 15 keV and 20 mA.

3.3. Experimental Results

As shown in Figure 13, the designed path is simplified and is approximated into 4 linear gradient segments, that are numbered sequentially starting from 100% W (region 1) to 100% Fe-9Cr steel (region 4). Region 4 and 3 were first printed, starting with single tracks to identify the appropriate parameter set.

A standard process parameter matrix was utilized for single tracks of laser speeds between 7 and 20 inches/min and laser power between 200W and 400W. Each single track was examined using SEM as discussed in the previous section. The images were then uploaded into Image J software where the average track widths were measured, and

the overall quality of the single tracks was evaluated. This method allowed optimal printability areas of the three critical composition points within the Region I of the path to be determined. The parameters that resulted in acceptable single-track characteristics for printing defect free parts from all three critical compositions were plotted together and the overlap region is presented in Figure 19. This region narrowed down the optimum process parameter window significantly, allowing the focus to be concentrated on a small area of process parameter space, and was used to generate the parameter set for the next step, a 10-layer square prism study for the optimization of layer thickness and hatch spacing.

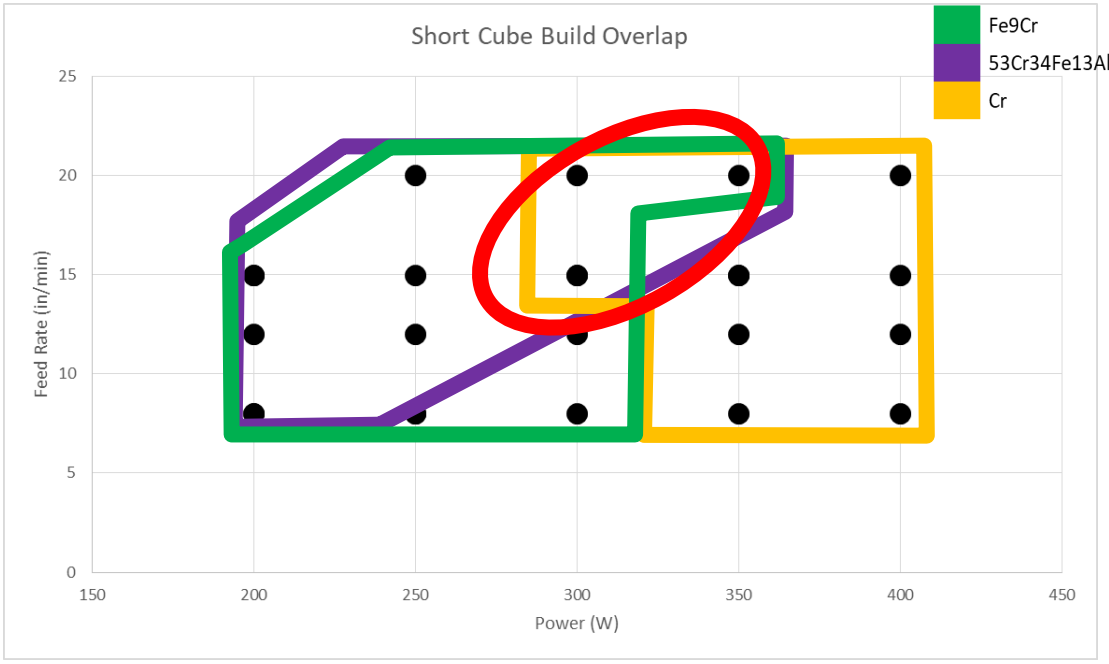

Figure 19. Optimal printability regions for the critical compositions points in Region IV and III of the new gradient path using single track experiments described in the text.

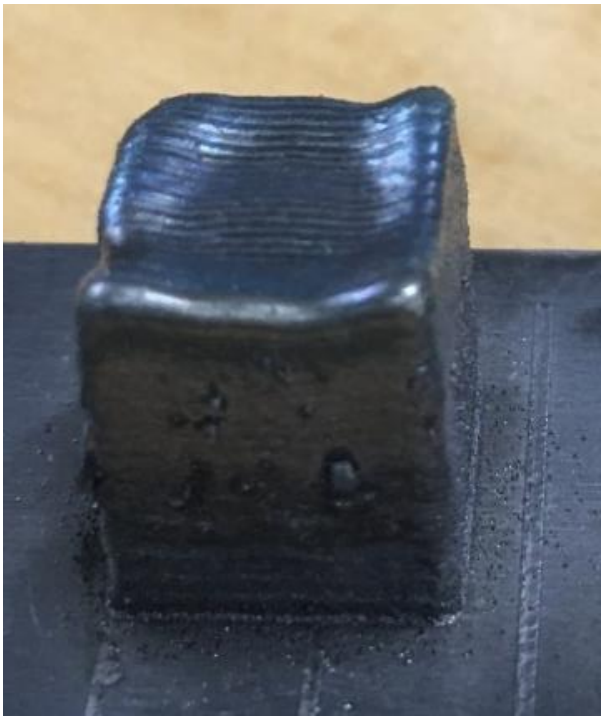

Figure 20. Region IV to III gradient print of the designed Path from Fe-9Cr to 100 %Cr.

Due to the validated optimum processing parameter region in Figure 19 and the success in testing these parameters for optimizing layer thickness and hatch spacing, one constant parameter set was selected for printing the entire Region IV and III of the path. The result seen in Figure 20 the part was relatively dense with minimal micro-cracks. From the SEM-BSE micrographs, Figure 21, it can be seen that the relatively density is consistent over the entirety of the gradient, and its microstructure evolves into larger grains as the sample continues to build up heat.

The WDS with EPMA evaluation, Figure 22 respectively, shows little deviation from the intended composition with an average error of less than 3.6% overall and a

standard deviation of 4.1. There was substantial Fe vaporization near the middle and top of the print, where the heat buildup was sufficient to vaporize notable portions due to continuous laser exposure and the substate as well as the Ar atmosphere heating up and becoming inefficient heat sinks. The sample was printed with no sooting, and the printed height was within 0.01 inches of the programmed height which is well within the accuracy of the system. The smooth surface and even layers of this part made it the best candidate for continuing gradient printing.

The examination of the entirety of the sample with XRD reviled that the gradient is BCC crystal structure as expected and there was no sign of detrimental phases appearing. As show in Figure 23 the BCC peaks are those associated with Cr and Fe, with a strong preference for the (011) direction.

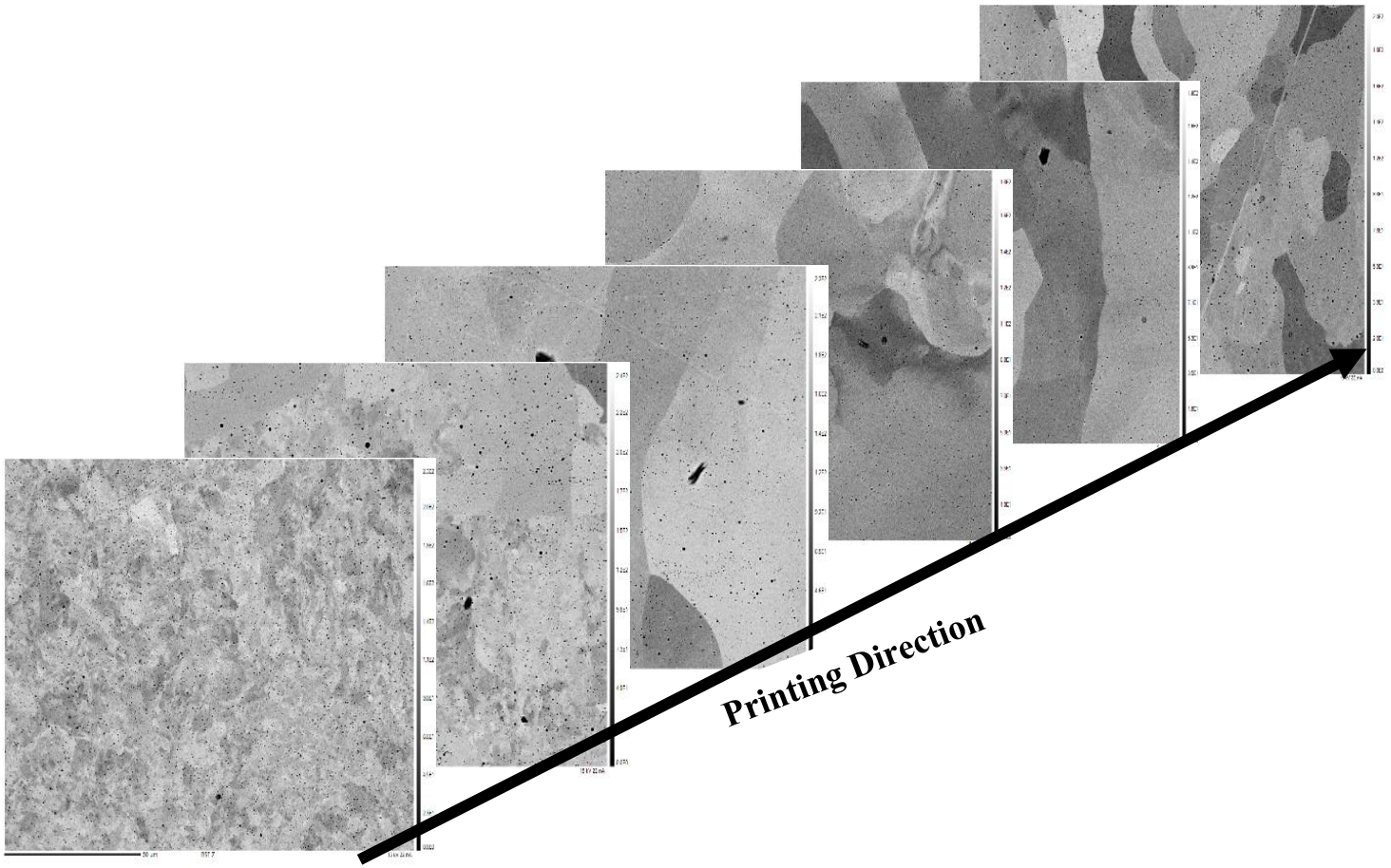

Figure 21. SEM - BSE images of Region IV to III gradient print of the designed path from Fe-9Cr (left) to 100 %Cr (right).

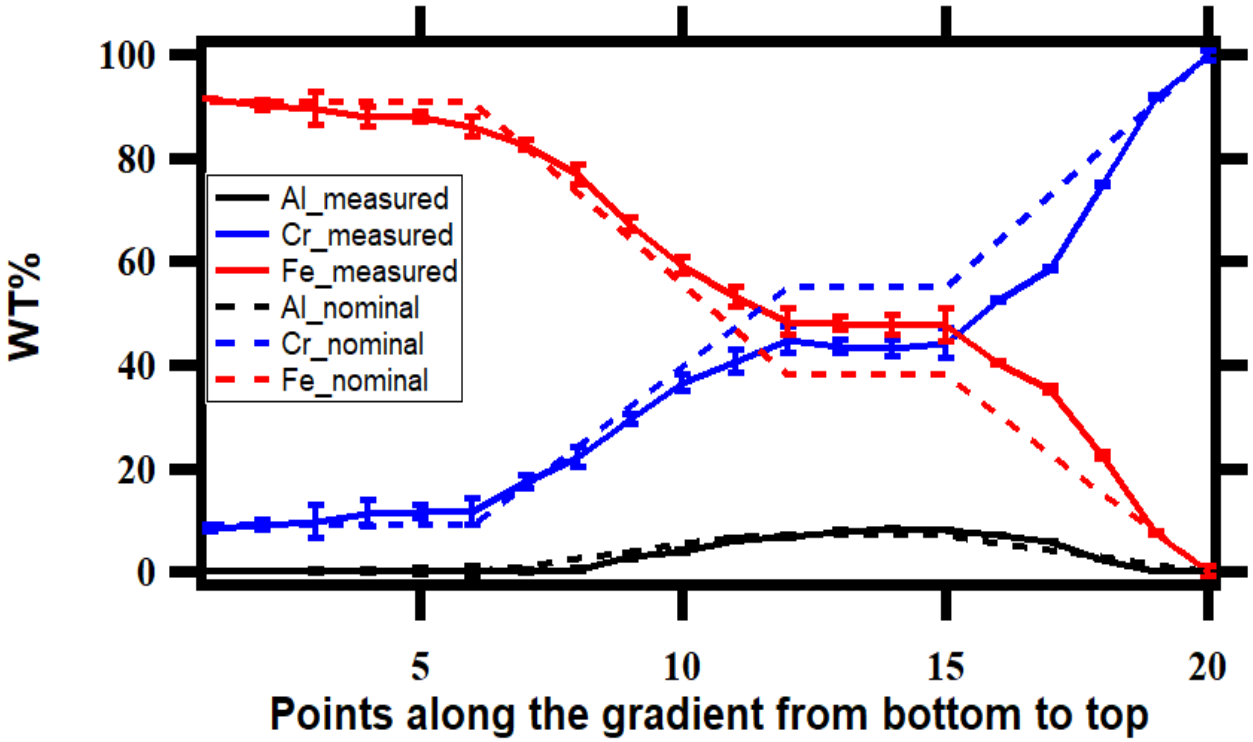

Figure 22. WDS - EPMA results of the Region IV to III gradient print of the designed path from Fe-9Cr to 100 %Cr showing the compositional change across the height in comparison with the target gradient compositions.

With the success seen in Figure 20, the next two critical points were included, and the full gradient was printed as seen in Figure 24. While oxidation and sooting occurred at the top of the sample, there was a substantial buildup of tungsten at the top of the sample.

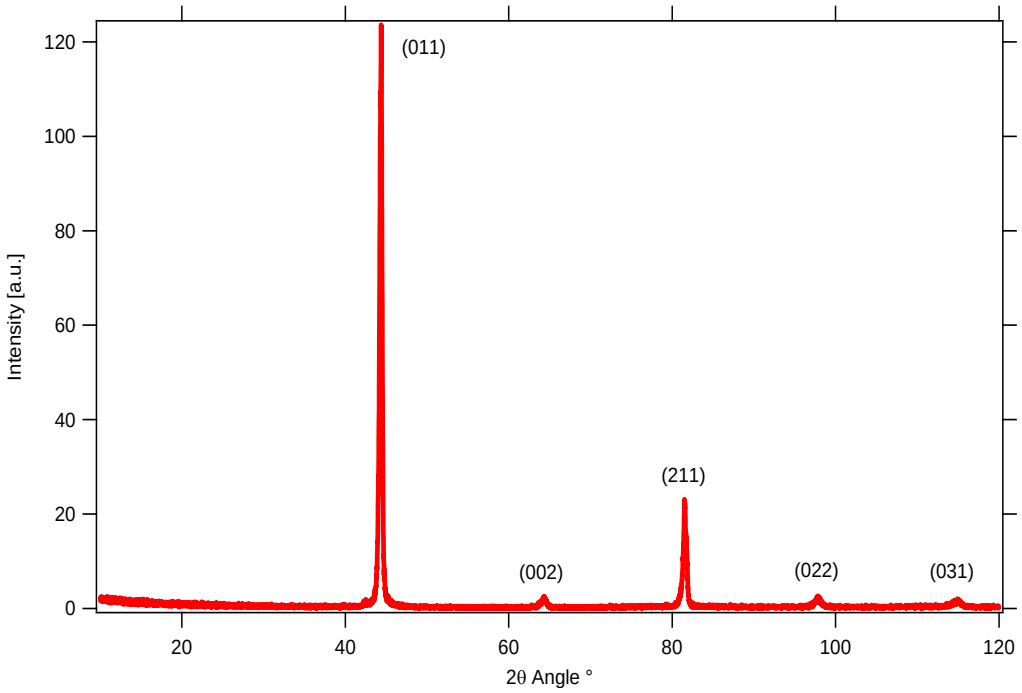

Figure 23. XRD results of the Region IV to III gradient print of the designed path from Fe-9Cr to 100 % Cr.

The SEM microstructure show in Figure 25 showed micro-cracking as more Chromium is incorporated into the matrix. These cracks are likely the result of hot tearing in the chromium rich grains. The rapid cooling of the weld pool can result in a skin that prevents the shrinking of chromium as it solidifies. These small cracks can be eliminated by decreasing the solidification rate. Increase the thermal input would also allow the diffusion of Chromium and Tungsten into each other decreasing the appetence of dendrites.

Figure 24. Full gradient print of the designed Path from Fe-9Cr to 100 %W.

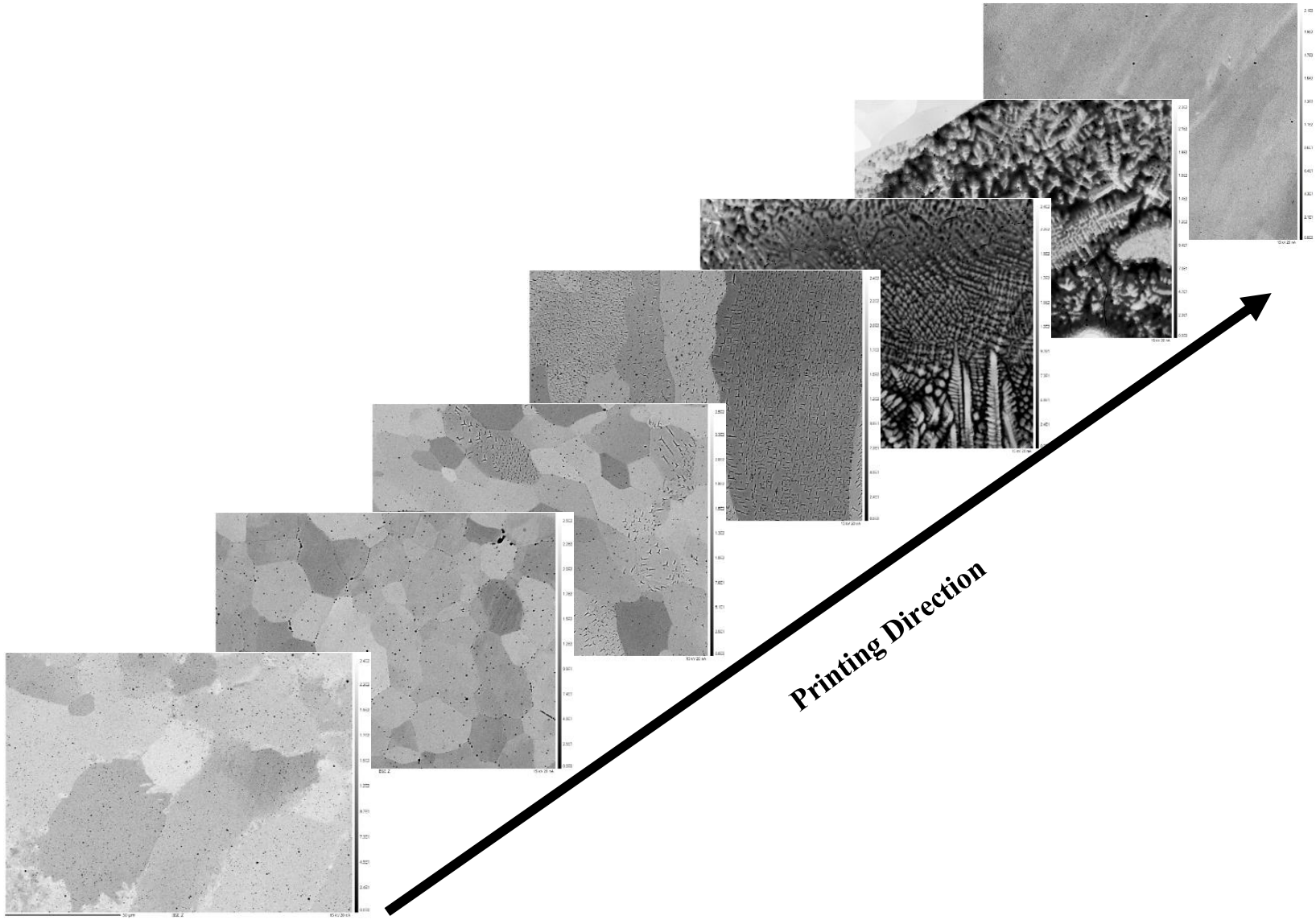

Figure 25. SEM - BSE images of Region I gradient print of the designed path from Fe-9Cr (left) to 100 %W (right).

The WDS analyses has shown an average 2.08 deviation from expected composition and 3.61 stranded deviation as shown in Figure 26.Using XRD, shown in Figure 27, it verified that the expected detrimental phases were avoided it this sample. Only BCC phase was prevenient though the gradient, with a smooth transition from Fe/Cr peak to Tungsten BCC peaks. A slight trace of Cr Oxide causes peak sifting around 100% chromium. The and chromium oxides could have resulted from the atmosphere in the printing chamber being above the oxidation threshold, will prints are done in Ar with less than 100ppm O2 content this may still be too high for Chromium. This problem could be solved by purging and atmosphere to a much lower ppm before printing or printing in a reducing atmosphere.

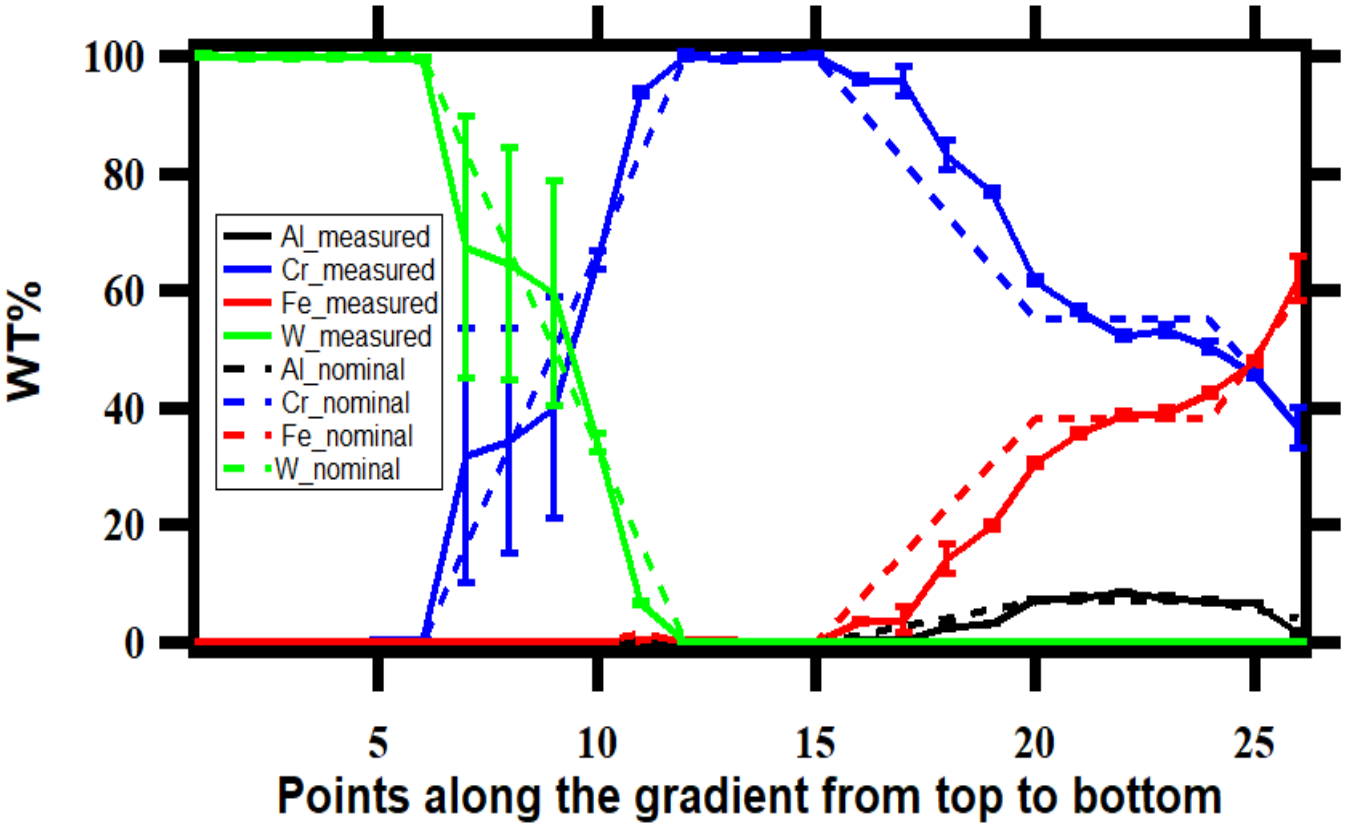

Figure 26. WDS - EPMA results of the full gradient print of the designed path from Fe-9Cr to 100 %W showing the compositional change across the height in comparison with the target gradient compositions.

Even with the appearance of microcracking the results showed that there was no trace of the predicted detrimental phase and the compositional accuracy showed the method was effective to print the planed path successfully.

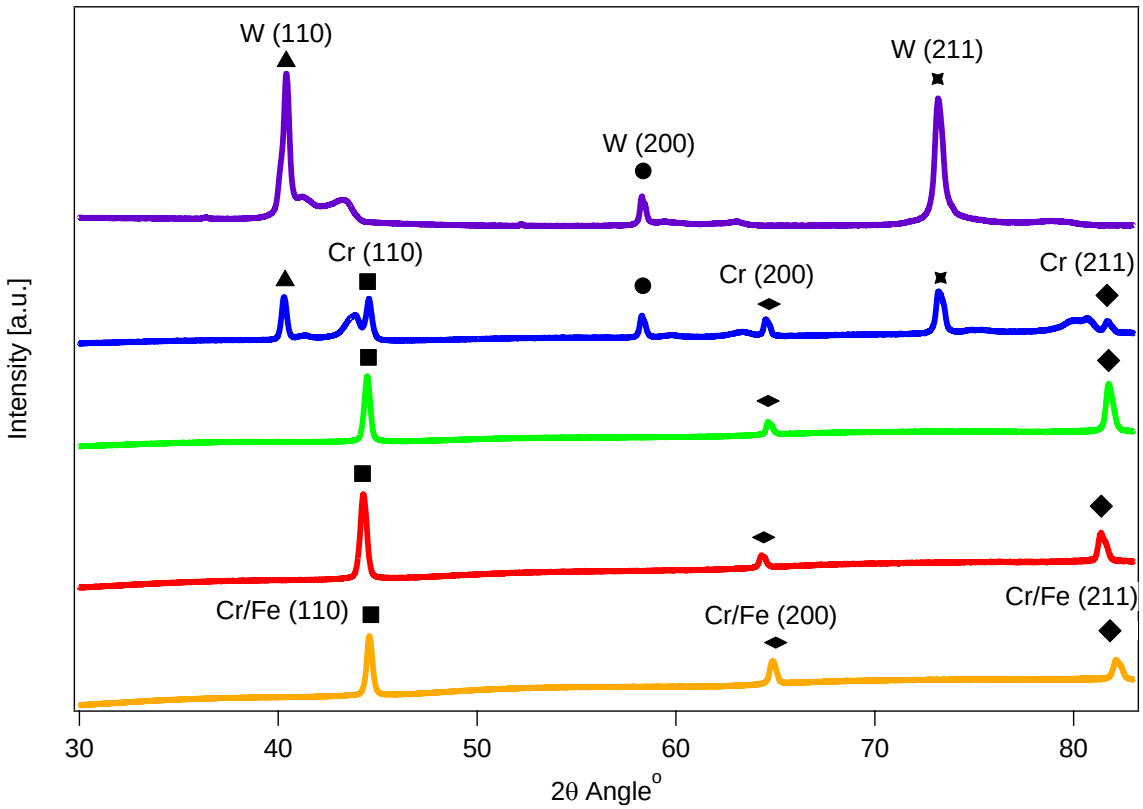

Figure 27. XRD results of the full gradient print of the designed path from Fe-9Cr to 100 %W showing the pecks shifting from Cr/Fe to W as the gradient changes compositionally along the planed path.

3.4. Summary

- An extensive exploration of the Fe-Cr-W-Al thermodynamic space was conducted to discover deleterious phase regions as well as regions of high solidification range and hot cracking susceptibility. The subsequent mapping can be used to avoid compositions or compositional gradients that are susceptible to cracking during manufacturing and other printability issues.
- A novel computational methodology was used to design new gradients between Fe9Cr and pure W. The designed gradient path significantly reduces the phase fraction of deleterious phases when compared to the linear gradient. The designed path also satisfies constraints on printability metrics like solidification cracking and hot cracking susceptibility.
- Analysis of the designed path led to a simplified gradient path that is predicted to produce no undesirable phases at any temperature.
- Developed a methodology to successful print a variety of composition with varying meting temperature and vaporization points.
- Successfully printed full gradient that avoided the predicted detrimental phases.

3.5. References

[1] C. Tan, K. Zhou, W. Ma, B. Attard, P. Zhang, and T. Kuang, “Selective laser melting of high-performance pure tungsten: parameter design, densification behavior and mechanical properties,” Sci. Technol. Adv. Mater., vol. 19, no. 1, pp. 370–380, Dec. 2018, doi: 10.1080/14686996.2018.1455154.

[2] J. Ma, J. Zhang, W. Liu, and Z. Shen, “Suppressing pore-boundary separation during spark plasma sintering of tungsten,” J. Nucl. Mater., vol. 438, no. 1, pp. 199–203, Jul. 2013, doi: 10.1016/j.jnucmat.2013.03.042.

[3] A. Šestan, P. Jenuš, S. N. Krmpotič, J. Zavašnik, and M. Čeh, “The role of tungsten phases formation during tungsten metal powder consolidation by FAST: Implications for high-temperature applications,” Mater. Charact., vol. 138, pp. 308–314, Apr. 2018, doi: 10.1016/j.matchar.2018.02.022.

[4] J.-S. Kim and H.-S. Kwon, “Effects of Tungsten on Corrosion and Kinetics of Sigma Phase Formation of 25% Chromium Duplex Stainless Steels,” Corrosion, vol. 55, no. 5, pp. 512–521, May 1999, doi: 10.5006/1.3284014.

[5] M. S. El-Genk and J.-M. Tournier, “A review of refractory metal alloys and mechanically alloyed-oxide dispersion strengthened steels for space nuclear power systems,” J. Nucl. Mater., vol. 340, no. 1, pp. 93–112, Apr. 2005, doi: 10.1016/j.jnucmat.2004.10.118.

[6] K. L. Murty and I. Charit, “Structural materials for Gen-IV nuclear reactors: Challenges and opportunities,” J. Nucl. Mater., vol. 383, no. 1, pp. 189–195, Dec. 2008, doi: 10.1016/j.jnucmat.2008.08.044.

[7] M. S. F. de Lima and S. Sankaré, “Microstructure and mechanical behavior of laser additive manufactured AISI 316 stainless steel stringers,” Mater. Des., vol. 55, pp. 526–532, Mar. 2014, doi: 10.1016/j.matdes.2013.10.016.

[8] R. Shrestha, J. Simsiriwong, and N. Shamsaei, “Fatigue behavior of additive manufactured 316L stainless steel parts: Effects of layer orientation and surface roughness,” Addit. Manuf., vol. 28, pp. 23–38, Aug. 2019, doi: 10.1016/j.addma.2019.04.011.

[9] F. Hejripour, F. Binesh, M. Hebel, and D. K. Aidun, “Thermal modeling and characterization of wire arc additive manufactured duplex stainless steel,” J. Mater. Process. Technol., vol. 272, pp. 58–71, Oct. 2019, doi: 10.1016/j.jmatprotec.2019.05.003.

[10] R. A. Causey and T. J. Venhaus, “The use of tungsten in fusion reactors: a review of the hydrogen retention and migration properties,” Phys. Scr., vol. 2001, no. T94, p. 9, 2001, doi: 10.1238/Physica.Topical.094a00009.

[11] E. S. Solntceva, M. L. Taubin, N. A. Bochkov, V. A. Solntsev, and A. A. Yaskolko, “Use of tungsten single crystals to enhance nuclear reactors structural elements properties,” Int. J. Hydrog. Energy, vol. 41, no. 17, pp. 7206–7212, May 2016, doi: 10.1016/j.ijhydene.2016.02.019.

[12] R. L. Klueh, “Reduced-activation bainitic and martensitic steels for nuclear fusion applications,” Curr. Opin. Solid State Mater. Sci., vol. 8, no. 3, pp. 239–250, Jun. 2004, doi: 10.1016/j.cossms.2004.09.004.

[13] B. S. Lee, M. C. Kim, J. H. Yoon, and J. H. Hong, “Characterization of high strength and high toughness Ni–Mo–Cr low alloy steels for nuclear application,” Int. J. Press. Vessels Pip., vol. 87, no. 1, pp. 74–80, Jan. 2010, doi: 10.1016/j.ijpvp.2009.11.001.

[14] D. Bachurina et al., “Joining of tungsten with low-activation ferritic–martensitic steel and vanadium alloys for demo reactor,” Nucl. Mater. Energy, vol. 15, pp. 135–142, May 2018, doi: 10.1016/j.nme.2018.03.010.

[15] D. Bachurina et al., “High-temperature brazing of tungsten with steel by Cu-based ribbon brazing alloys for DEMO,” Fusion Eng. Des., vol. 146, pp. 1343–1346, Sep. 2019, doi: 10.1016/j.fusengdes.2019.02.072.

[16] Q. Cai, W. Liu, Y. Ma, and Z. Wang, “Diffusion brazing of tungsten and steel using Ti–Ni liquid phase forming interlayer,” Fusion Eng. Des., vol. 91, pp. 67–72, Feb. 2015, doi: 10.1016/j.fusengdes.2014.12.029.

[17] S. B. Lin, J. L. Song, C. L. Yang, C. L. Fan, and D. W. Zhang, “Brazability of dissimilar metals tungsten inert gas butt welding–brazing between aluminum alloy and stainless steel with Al–Cu filler metal,” Mater. Des. 1980-2015, vol. 31, no. 5, pp. 2637–2642, May 2010, doi: 10.1016/j.matdes.2009.12.005.

[18] D. Easton, J. Wood, S. Rahimi, A. Galloway, Y. Zhang, and C. Hardie, “Residual Stress Generation in Brazed Tungsten Dissimilar Joints,” IEEE Trans. Plasma Sci., vol. 44, no. 9, pp. 1625–1630, Sep. 2016, doi: 10.1109/TPS.2016.2565205.

[19] B. A. Kalin, V. T. Fedotov, O. N. Sevrjukov, A. Moeslang, and M. Rohde, “Development of rapidly quenched brazing foils to join tungsten alloys with ferritic steel,” J. Nucl. Mater., vol. 329–333, pp. 1544–1548, Aug. 2004, doi: 10.1016/j.jnucmat.2004.04.170.

[20] W. W. Basuki and J. Aktaa, “Investigation on the diffusion bonding of tungsten and EUROFER97,” J. Nucl. Mater., vol. 417, no. 1, pp. 524–527, Oct. 2011, doi: 10.1016/j.jnucmat.2010.12.121.

[21] W. W. Basuki and J. Aktaa, “Investigation of tungsten/EUROFER97 diffusion bonding using Nb interlayer,” Fusion Eng. Des., vol. 86, no. 9, pp. 2585–2588, Oct. 2011, doi: 10.1016/j.fusengdes.2011.03.017.

[22] T. Weber and J. Aktaa, “Numerical assessment of functionally graded tungsten/steel joints for divertor applications,” Fusion Eng. Des., vol. 86, no. 2, pp. 220–226, Mar. 2011, doi: 10.1016/j.fusengdes.2010.12.084.

[23] W. S. Liu, Q. S. Cai, Y. Z. Ma, Y. Y. Wang, H. Y. Liu, and D. X. Li, “Microstructure and mechanical properties of diffusion bonded W/steel joint using V/Ni composite interlayer,” Mater. Charact., vol. 86, pp. 212–220, Dec. 2013, doi: 10.1016/j.matchar.2013.10.013.

[24] Y. Wang et al., “Interfacial structure and formation mechanism of tungsten/steel HIP diffusion bonding joints using Ni interlayer,” J. Manuf. Process., vol. 52, pp. 235–246, Apr. 2020, doi: 10.1016/j.jmapro.2020.02.001.

[25] A. Reichardt et al., “Advances in additive manufacturing of metal-based functionally graded materials,” Int. Mater. Rev., vol. 0, no. 0, pp. 1–29, Jan. 2020, doi: 10.1080/09506608.2019.1709354.

[26] B. E. Carroll et al., “Functionally graded material of 304L stainless steel and inconel 625 fabricated by directed energy deposition: Characterization and thermodynamic modeling,” Acta Mater., vol. 108, pp. 46–54, 2016.

[27] L. D. Bobbio et al., “Additive manufacturing of a functionally graded material from Ti-6Al-4V to Invar: Experimental characterization and thermodynamic calculations,” Acta Mater., vol. 127, pp. 133–142, 2017.

[28] B. Chen, Y. Su, Z. Xie, C. Tan, and J. Feng, “Development and characterization of 316L/Inconel625 functionally graded material fabricated by laser direct metal deposition,” Opt. Laser Technol., vol. 123, p. 105916, Mar. 2020, doi: 10.1016/j.optlastec.2019.105916.

[29] W. Meng et al., “Additive manufacturing of a functionally graded material from Inconel625 to Ti6Al4V by laser synchronous preheating,” J. Mater. Process. Technol., vol. 275, p. 116368, Jan. 2020, doi: 10.1016/j.jmatprotec.2019.116368.

[30] T. Kirk, E. Galvan, R. Malak, and R. Arroyave, “Computational Design of Gradient Paths in Additively Manufactured Functionally Graded Materials,” J. Mech. Des., vol. 140, no. 11, Nov. 2018, doi: 10.1115/1.4040816.

[31] O. V. Eliseeva et al., “Functionally Graded Materials through robotics-inspired path planning,” Mater. Des., vol. 182, p. 107975, Nov. 2019, doi: 10.1016/j.matdes.2019.107975.

[32] S. Karaman and E. Frazzoli, “Sampling-based algorithms for optimal motion planning,” Int. J. Robot. Res., vol. 30, no. 7, pp. 846–894, 2011.

[33] O. Adiyatov and H. A. Varol, “Rapidly-exploring random tree based memory efficient motion planning,” in Mechatronics and Automation (ICMA), 2013 IEEE International Conference on, 2013, pp. 354–359, doi: 10.1109/ICMA.2013.6617944.

[34] M. A. Easton, M. A. Gibson, S. Zhu, and T. B. Abbott, “An A Priori Hot-Tearing Indicator Applied to Die-Cast Magnesium-Rare Earth Alloys,” Metall. Mater. Trans. A, vol. 45, no. 8, pp. 3586–3595, Jul. 2014, doi: 10.1007/s11661-014-2272-7.

[35] Z. Sun, X. P. Tan, M. Descoins, D. Mangelinck, S. B. Tor, and C. S. Lim, “Revealing hot tearing mechanism for an additively manufactured high-entropy alloy via selective laser melting,” Scr. Mater., vol. 168, pp. 129–133, Jul. 2019, doi: 10.1016/j.scriptamat.2019.04.036.

[36] S. Kou, “A criterion for cracking during solidification,” Acta Mater., vol. 88, pp. 366–374, Apr. 2015, doi: 10.1016/j.actamat.2015.01.034.

[37] E. Scheil, “Bemerkungen zur schichtkristallbildung,” Z. Für Met., vol. 34, no. 3, pp. 70–72, 1942.

[38] T. Keller et al., “Application of finite element, phase-field, and CALPHAD-based methods to additive manufacturing of Ni-based superalloys,” Acta Mater., vol. 139, pp. 244–253, Oct. 2017, doi: 10.1016/j.actamat.2017.05.003.

4. MACHINE LEARNING FOR POROSITY LOCATION IN ADDITIVELY MANUFACTURED PARTS

4.1. Introduction

Microstructural features produced by complex metal additive manufacturing (AM) processes can strongly influence material properties and are controlled by numerous details of the process plan, fabrication environment, and feedstock utilized[1]–[6]. While some of these contributing factors have a strong stochastic aspect, systematic details of the processing plan also both directly drive the material response and affect susceptibility to random events, often in a location-specific manner. Significant prior work has focused on identifying material-specific global process parameter combinations that generate desirable microstructural features over the balance of a component, but often do not address location-specific features influenced by the details of the processing plan [7]–[9]. In this work, we describe a methodology to develop a transfer function that links location-specific processing information with microstructure features for a laser powder bed fusion (LPBF) process. Specifically, as shown in Figure S1, we use a classifier to link attributes of the time-temperature history to location-specific porosity, and then describe how such a tool could be utilized within a process design and optimization framework.

As significant aspects of microstructural feature formation are linked to the local thermal history, we hypothesize that such information can be effectively utilized to predict likelihood of porosity formation when processing new geometries, utilizing new scan path generation algorithms, or a combination of both. We demonstrate that such a

tool can be trained using a combination of thermal history predictions from a fast-acting model and destructive characterization data as described in Figure S1. Starting with a 3-dimensional model, the part is first printed, its microstructure analyzed, and labels of important features are generated. Concurrently, a digital twin of the printing process is instantiated and used to generate location-specific process representations. These are then featurized, and labels from the characterization activity are associated with feature sets on a location-specific basis. Collectively, these data are used to train a classifier, which can then be used to predict microstructural characteristics—in this case, the presence/absence of porosity originating from unique aspects of the thermal history of a location in the fabricated part—given processing information. Such a capability can be used to assess an arbitrary processing plan for a new component, a plan generated by a new scan path generation algorithm, or even embedded in an optimization framework to generate a novel plan.

While a range of microstructural features are important in different alloy systems, one critical microstructural aspect for mechanical properties, particularly fatigue performance, is the presence of porosity or voids. Pores form due to 3 primary mechanisms during LPBF. The keyhole mechanism occurs when conditions are sufficient to result in significant vaporization from the melt pool, creating a deep depression in the liquid-vapor surface [10]. This feature is often dynamic, unstable, and a can frequently collapse on itself, trapping vapor and creating a void [11]–[14]. The lack-of-fusion (LOF) mechanism is a result of inadequate melting of material due to insufficient energy input, poor laser path, unsatisfactory spreading of powder, or a

combination of these factors. [10], [15]. The third mechanism is the result of trapped gases during powder production[10]. Pores formed during e.g. gas atomization can be retained through the LPBF process as the duration in the molten state is not long enough for these bubbles to reach the liquid-vapor interface and break [16].

In situ methods to reliably identify porosity are in development [17]–[20], and post-print inspection techniques such as x-ray computed tomography (CT) are more commonly utilized for this purpose. While in situ and post build inspections will likely remain necessary for items with stringent reliability requirements, it is highly desirable to optimize processing plans in order to minimize the probability of porosity formation during printing. Significant previous work has focused on porosity across the entirety of the part. Tapia et al., for example, developed a statistical model to estimate porosity based on the function of laser power and scanning speed [21]. While such methods can be applied to decrease the porosity of the full part, they do not account for the full scan path or geometry details. Ning et al. developed a model based on physics and geometry to predict porosity; however, this was to predict the overall porosity in a part and again does not identify location-based formation within the part [8], [9].

The present method takes a finer grained approach, as summarized in Figure 28. Our framework starts with a given part, whose fabrication via 3D printing has already been specified through a layer-by-layer printing protocol. Once the process plan has been defined, the part is fabricated, while the same process plan is executed, through an efficient thermal model, in order to attain a ‘digital twin’. After fabrication, the part is characterized on a layer-by-layer basis, identifying microstructural features of interest—

in this case, porosity. The ‘digital twin’ of a specific layer is in turn represented in terms of a collection of location specific thermal histories that are time- and location-aligned to the fabrication protocol used in the real 3D printed part. Human-assisted automated schemes are used to identify microstructural features of interest in a cross section in order to generate labels (e.g. pore/no-pore). In order to further reduce the dimensionality of the problem, specific features in the location-specific thermal histories are extracted in order to obtain local ‘thermal signatures’. The thermal signatures are then used as features in order to train a classifier against the microstructure-specific labels generated from the experimental observations.

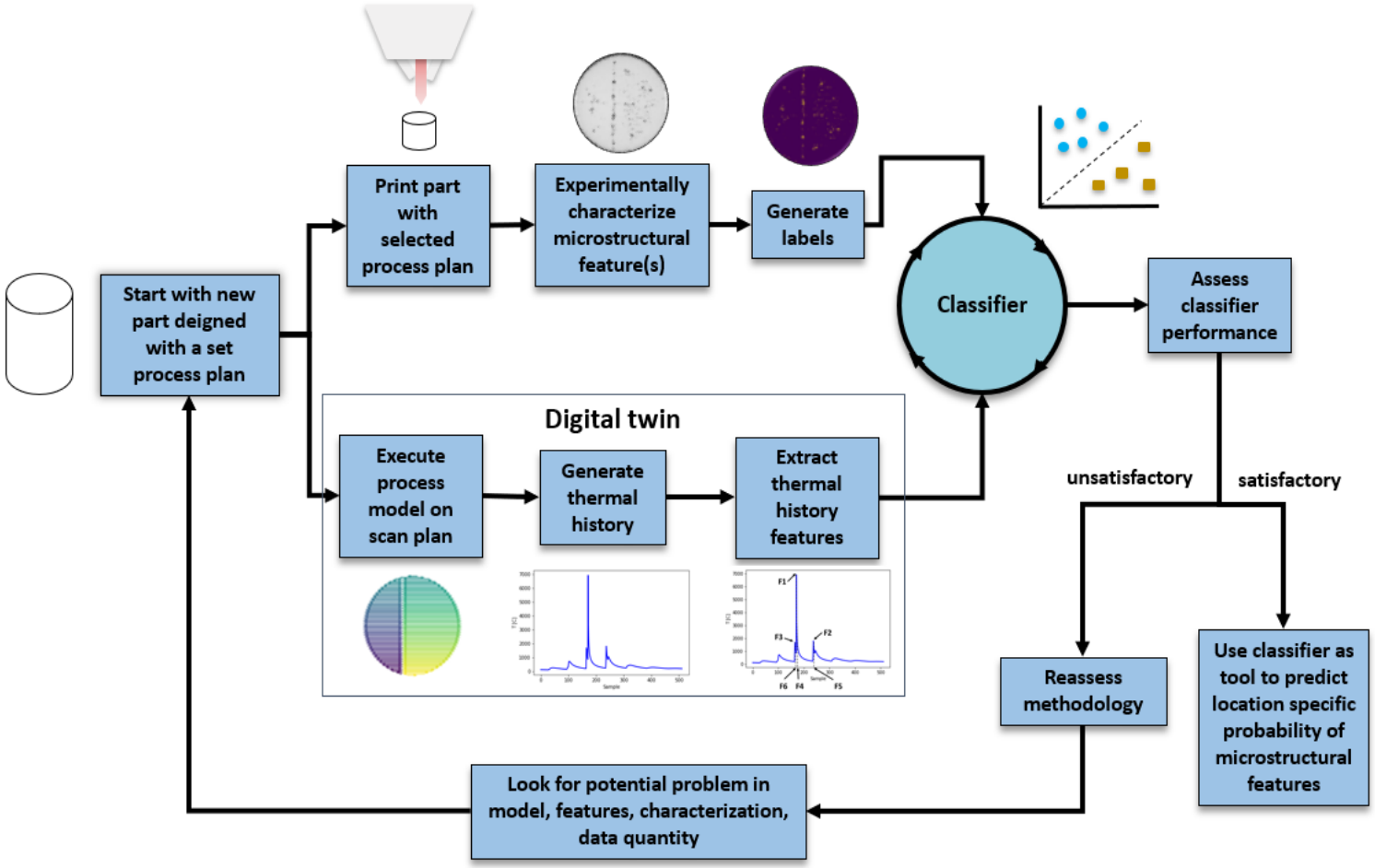

Figure 28. Summary of the process of going from a part's scanning strategy to a classifier that is able to identify the probability of thermally linked feature existing. Starting with a scan strategy a part is created, sectioned and the microstructure features of interest are labeled. At the same time a corresponding digital twin of the scan strategy is generated, thermal curves along the scan strategies are produced, and features are extracted from the thermal curves. Next the extracted features from the thermal curves and microstructure feature of interest location labels are then feed into a classifier. Finally, the efficiency and effectiveness of the classifier can be

Preliminary findings can be seen in Appendix C.

4.2. Results and Discussion

In the Methods section we discuss in detail the different elements of the framework described above. Here, we limit ourselves to present the main results of the present work. The curating and data sampling to ensure independence largely determines a classifiers' usefulness and accuracy. This work aims to test a framework that takes experimentally created parts and links internal microstructural features to thermal curve data for porosity identification. To begin data processing, first the dataset of thermal history peaks need to be normalized. This is especially important for classifiers like K-nearest neighbour (KNN) and support vector machine (SVM) as their effectiveness are greatly affected by the data distribution [22].

The methodology to normalize the data was approached from 3 directions, as shown in Figure 27, first a standard scalar was used to produce a unit vector from the give peak intensity data. This method had the best overall performance for SVM and KNN, it also had notably fastest training test times over the 2 other normalization processes. The second method used to normalize the data using the mean and standard deviation of all temperature and all-time features. This normalization resulted

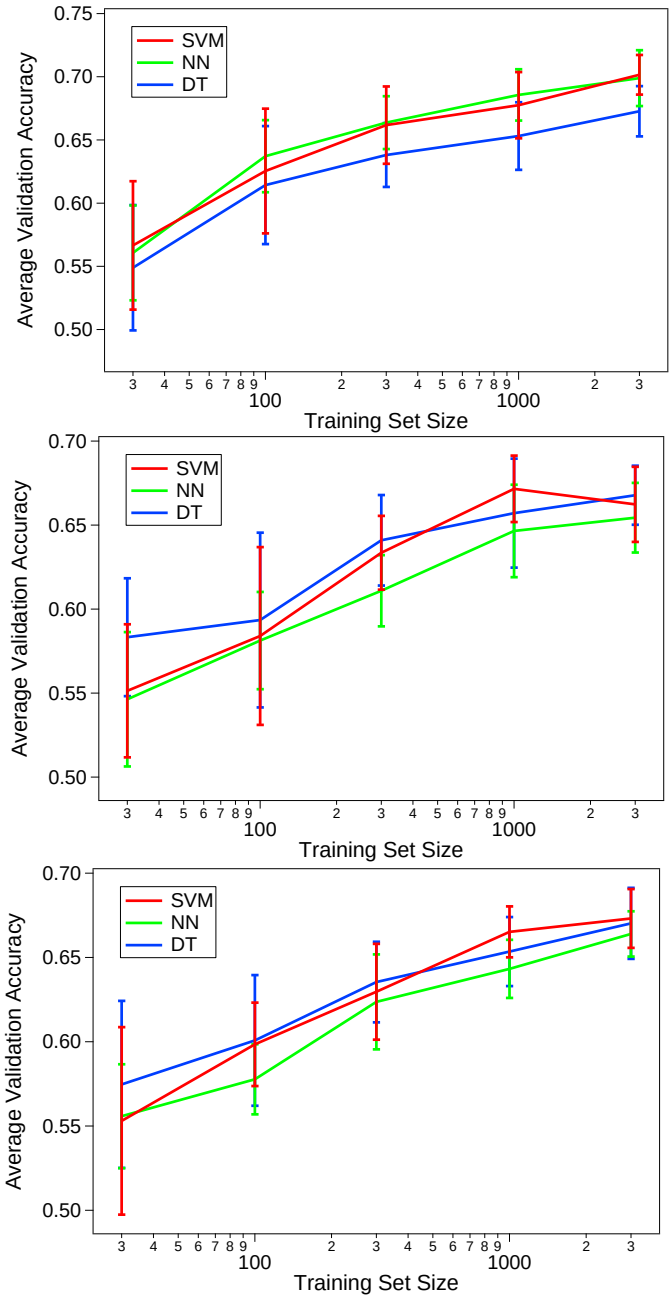

Figure 29. Three methods of standardization of data a) Standard Scaler methodology b) scaled with mean and standard deviation of all temperature and all time features for scaling c) standardized with predefined temperature and time scale for standardization

in worse performance for SVM and KNN while it was relatively consistent for data tree as normalization does not play a large part in the method of data separation in that technique. The last normalization method used a predefined temperature and time scale for standardization. However, this normalization methodology did not offer an improvement over standardized normalization ,which was selected for the remained of this study.

The next important metric to consider is the number of features and their effect on accuracy of the classifier. In this case, the number of features was directly linked to the number of peaks in the thermal curve at a given location. The classifiers' ability to separate the pore thermal curves from non-pore thermal curves increased initially to 5 peaks, as demonstrated in Figure 30. The accuracy initially increases with increasing number of peaks, particularly for the SVM and KNN classifiers, with relatively little improvement as feature sized increased beyond this value. The data tree classifier on the other hand rises with the number of features. However, this can be misleading as data tree will begin over fitting as more features are introduced, especially if those features add little value to the data separability [23]. So, to strike a balance between accuracy and computation time, 5 peaks were used for the following evaluations resulting in 9 total features: 5 peek magnitudes and 4 times between peaks.

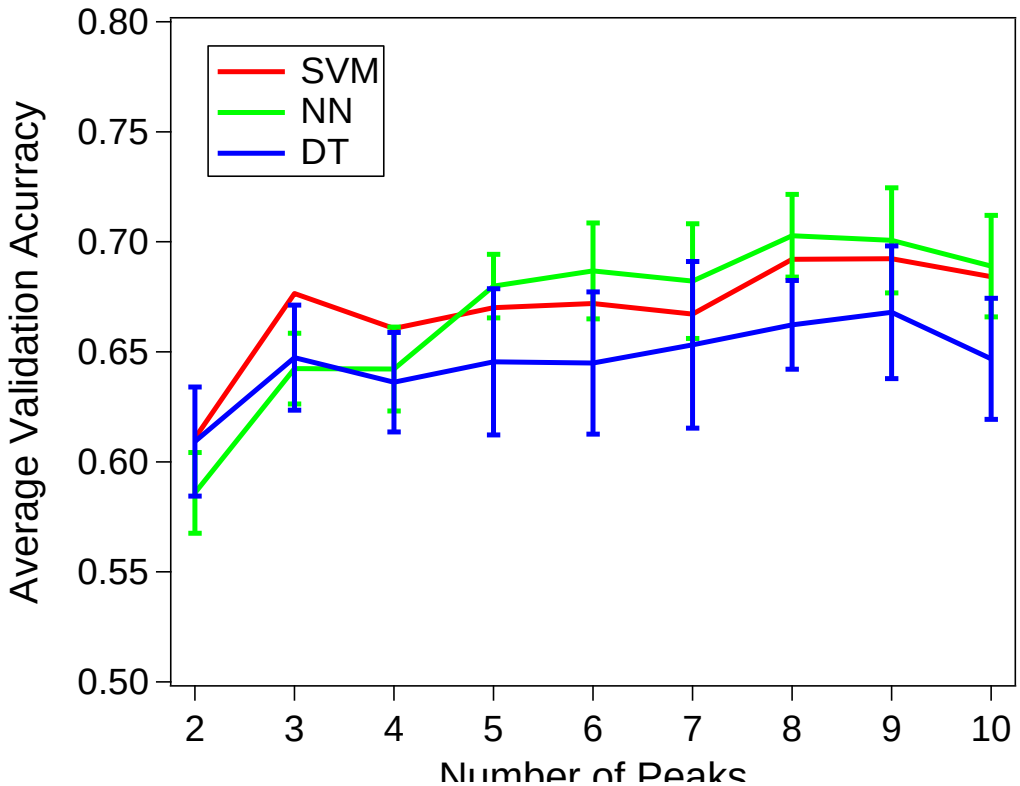

Figure 30. Number of peaks effect on accuracy

Once the number of features were selected and the normalization technique for those features was implemented, the effect of the training set size was assessed. The training set size needs to be selected to ensure the classifiers see each pore type and there is enough information to effectively select hyper-parameters for each classifier. In this case training set of size larger than 300 shows the best validation accuracy, demonstrated in Figure 31. All three classifiers plateau around 65% accuracy and do not show improvement as more data points are used to train the classifier. All the classifiers all have multiple hyper-parameters which can be tailored to achieve the optimal classifier for this data set, however even with the refinement the data plateau. This leads us to

believe that the classifiers are not over fitting, but instead hitting a natural limit of the available data.

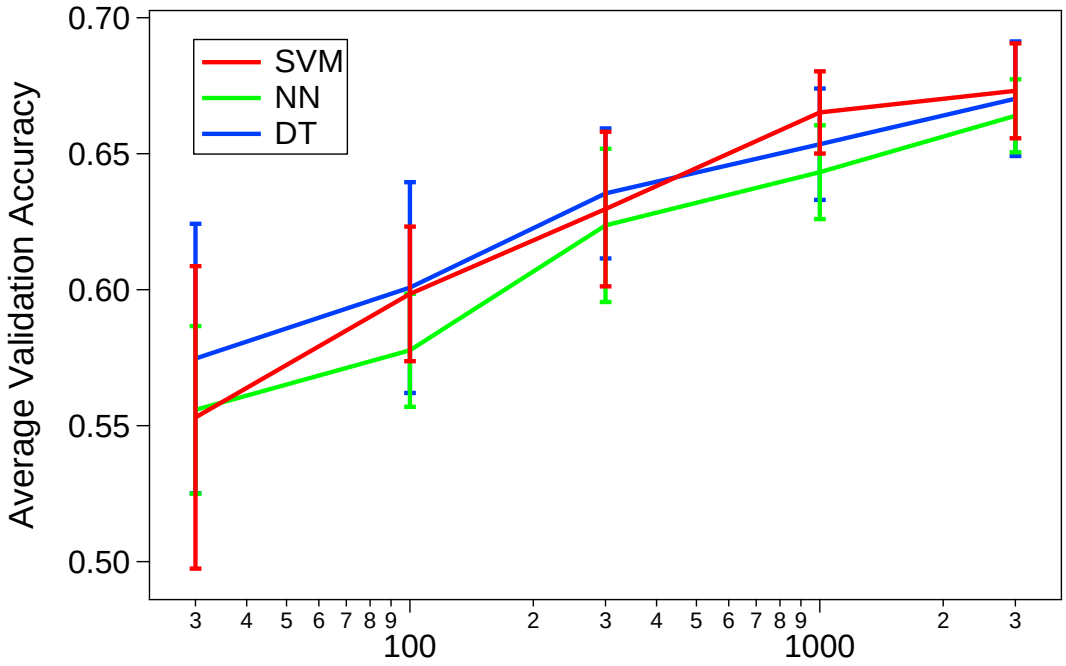

Figure 31. Classifier validation size effect on accuracy

In this work the validation accuracy of the classifier stabilizes around 300 training size. This result could stem from the inherent limitation of the available data. In this work there are only 483 unique pores and as the data are evenly split into independent training and validation sets as described in the Methods section, a maximum of 241 unique pores are available for training. For cases with less than 300 thermal histories, additional unique points are added to the training set as its size is increased. Beyond this size though, addition of thermal histories no longer introduces new pores, but rather begins to better represent the variance in thermal history within the pores already in the set.

Overall, the classifiers reach a max of 65% in their ability to take a single layer of a cylinder and evaluate the thermal histories to determining if porosity had formed. This result shows a direct link between porosity and thermal histories. It also shows that a single layer thermal history is not enough to completely identify porosity formation. For a full understanding of porosity formation multiple layers would have to be considered as processing on subsequent layers can either fill the porosity or vaporize material. Even if such data were introduced it would be impossible to account for stochastic events that occur during printing, and 100% accuracy is never expected. However, this methodology can be applied to evaluate effective scanning strategies.

For this method SVM or KNN stand out as the best classifiers for this data set which effectively separates the data set without over fitting if the training set is kept relatively small around 300 unique points from both classes. These methodologies show the potential for this methodology to become an effective tool not only for porosity identification but for all thermally linked microstructural features. In order to increase is effectiveness more data is required. Since porosity are relatively rare events and there are very few unique incidences available for training more layers would be required to encompass the thermal relationship. It would also be beneficial to introduce a variety of varying geometries to add variety in scan patterns.

4.3. Methods

Lack of density features were identified in a Ti-6Al-4V column which was printed with conditions as described in Ref Schwalbach et al. [24]. This column was robotically serial sectioned [25] with slices parallel to the build direction using optical

bright-field microscopy with a pixel size of 2.084um/px. Approximately 120 slices with a mean slice spacing of 1.0µm was collected. A single slice with significant lack of density was identified for further analysis. The slice image was processed to identify pores using a robust automatic thresholding technique [26], [27] followed by morphological operations to remove small features and scratches [21] and finally, the binary images were segmented, and a reconstruction of the scan path corresponding to the same layer was manually aligned the segmented image. To final pore mask consisting of 54,007,801 pixels 18,083,983 were from the actual cylinders of those 240,947 were from open pore locations. From the 483 unique identified pores only 1.3% of cylinder was identified as containing porosity. To create the data set 20, 000 pixels were selected randomly from each of the two classes i.e. “pore” and “No Pore” this create a data set of 40,000 pixels. The thermal histories were computed on the unique pixels using parameters described in the Sample Linked Parameters column of Table 2.

Table 2. List of Process and Thermophysical Parameters

Property	Phantom Parameters	Sample Linked Parameters
P [W]	200	290
V[mm s^{-1}]	1000	1300
$4\,\sigma_x = 4\,\sigma_z$ [μm]	75	75
η	1.0	0.5
h [μm]	100	140
T_0 [°C]	25	80
ρ[kg m^{-3}]	4252	4252
c_p [J kg^{-1} K^{-1}]	679	679
K [W m^{-1} K^{-1}]	22.9	22.9
Δt [μs]	20	20
r_{cutoff} [mm]	1	1
t_{cutoff} [s]	∞	∞

The Discrete Source Model used to create the thermal curves for every selected pixel is a computationally inexpensive method that captures energy input and the thermal conduction to estimate local thermal history and is described in more detail in [24]. While the model uses a simple temporal discretization scheme to estimate the behavior of complex scanning trajectories and does not explicitly account for radiation and evaporation, it has been shown to capture many important aspects of melt pool geometry in validation activities.

4.3.1. Peak Identification and Feature Creation

Peaks in each thermal history are identified using the find_peaks function in the scipy.signal module [28]. A peak is defined as a local maximum in the temperature as a function of time curve. Furthermore, a peak is required to have a temperature greater than 100°C and be more than 10 time steps from an adjacent peak. If multiple peaks are identified within this distance, only the most intense peak is retained. From this initial list of peaks, the subset of the Npeaks most intense peaks are selected, and the absolute times associated with these events are identified. To remove information about the absolute timing, the chronologically earliest peak is used as a local time datum and its time is subtracted from all remaining times to produce a new set of time features. With this definition, the first time is always zero, and is therefore dropped from the feature vector. Also, if the total number of peaks present in a thermal history is less than Npeaks, then the remaining expected peaks are padded with 0 intensity and times of 0. In this manner, for choice Npeaks the feature vector will have 2 Npeaks-1 components.

4.3.2. Feature Standardization

The native features used are measured in different units and span several orders of magnitude in scale. Such a feature set typically requires some form of feature scaling or standardization for the best performance of some classifiers [22]. Three methods for scaling the native feature vectors were tested including the typical z-score method, a modified z-score method, and a physically informed approach. For the standard z-score method, the population mean and standard deviations are calculated independently across the full population of each component of the feature vector. The component wise

mean value is then subtracted, and the resulting values are divided by the component wise standard deviation, brining each feature component's distribution to have a zero mean and unit variance, which is desirable for efficient training of some classifiers. This approach removes information about the relative magnitude between all feature types, including those measured in like units (e.g., temperature of the tallest and next tallest peak), which may actually be undesirable. One approach to retain this information would be to explicitly add additional features to encode these differences, but this would essentially double the size of the feature vector. Another approach is to modify the scaling methodology. For the modified z-score approach, instead of computing the mean and standard deviation for each feature component independently, we compute these quantities across all values in all feature components measured in the same physical units. In the present case, there is one set of features with units of temperature, and another with time. The final approach tested was to use a physics informed method to select characteristic temperature and time scales for the standardization process. In this case, we subtracted off the material's melting temperature from all temperature features, and then divided by 3 times the same temperature. For the time features, we subtracted off the characteristic time associated with thermal diffusion across a distance of 1 mm. Across these three methods, the standard z-score approach resulted in feature distributions that most closely followed the desired zero-mean unit-variance target, and the physics informed was the most independent of the input data.

4.3.3. Training and Validation

There are only 483 unique pores represented in the original image, meaning that an individual pore is represented by multiple thermal histories. Furthermore, larger pores will contribute more thermal histories to the overall population proportional to their relative area. While the thermal histories coming from different locations within the same pore are not identical, their features are likely to be highly correlated. A purely random assignment of thermal histories to training and validation sets would result in correlated features in both sets, and this could lead to an inflated validation score, particularly as the set sizes are increased. To avoid such a situation, we first divide the population of pores into unique subsets for classifier training, and another for validation, with no unique pores contributing thermal histories to both subsets. Furthermore, we desire that the original size distribution (and potentially pore formation mechanisms) is faithfully reproduced in both subsets to the extent possible. To achieve this, we first order the unique pore indices according to their size, and from this size-ordered list we alternately assign the pores to either the training or validation subset.

Once the two subsets are selected, we train 3 different types of classifier using data from the training subset, including a support vector machine (SVM), k-nearest neighbors (NN), and a decision Tree (DT). Because some training operations can take significant time, we select a subset of the training set of size Ntrain. This subset is then used in a 100 iteration random search for optimal hyperparameters. From this population of 100 hyper parameter combinations, the one achieving the highest 5-fold cross-validation score is selected as the best-performing classifier, and is then employed

to classify points from the as yet unseen validation set. This operation is then repeated 15 times, and the mean and standard deviation of the validation scores of the best performing classifiers is determined and recorded. We also systematically increase Ntrain to determine when adding additional training data is no longer worth the additional training time, particularly for the support vector machine. All calculations are performed using the scikit-learn library [29].

Additionally, Npeaks included in the feature set was varied from Npeaks=2 up to 10. For this test, Ntrain was fixed at 300.

4.4. References

[1] Z. Snow, A. R. Nassar, and E. W. Reutzel, “Invited Review Article: Review of the formation and impact of flaws in powder bed fusion additive manufacturing,” Addit. Manuf., vol. 36, p. 101457, Dec. 2020, doi: 10.1016/j.addma.2020.101457.

[2] S. Tammas-Williams, H. Zhao, F. Léonard, F. Derguti, I. Todd, and P. B. Prangnell, “XCT analysis of the influence of melt strategies on defect population in Ti–6Al–4V components manufactured by Selective Electron Beam Melting,” Mater. Charact., vol. 102, pp. 47–61, Apr. 2015, doi: 10.1016/j.matchar.2015.02.008.

[3] H. Gong, K. Rafi, H. Gu, T. Starr, and B. Stucker, “Analysis of defect generation in Ti–6Al–4V parts made using powder bed fusion additive manufacturing processes,” Addit. Manuf., vol. 1–4, pp. 87–98, Oct. 2014, doi: 10.1016/j.addma.2014.08.002.

[4] J. L. Huang, N. Warnken, J.-C. Gebelin, M. Strangwood, and R. C. Reed, “On the mechanism of porosity formation during welding of titanium alloys,” Acta Mater., vol. 60, no. 6, pp. 3215–3225, Apr. 2012, doi: 10.1016/j.actamat.2012.02.035.

[5] M. Iebba et al., “Influence of Powder Characteristics on Formation of Porosity in Additive Manufacturing of Ti-6Al-4V Components,” J. Mater. Eng. Perform., vol. 26, no. 8, pp. 4138–4147, Aug. 2017, doi: 10.1007/s11665-017-2796-2.

[6] S. Katayama, N. Seto, J.-D. Kim, and A. Matsunaw, “Formation mechanism and reduction method of porosity in laser welding of stainless steel,” Int. Congr. Appl. Lasers Electro-Opt., vol. 1997, no. 1, pp. G83–G92, Nov. 1997, doi: 10.2351/1.5059741.

[7] G. Tapia, A. H. Elwany, and H. Sang, “Prediction of porosity in metal-based additive manufacturing using spatial Gaussian process models,” Addit. Manuf., vol. 12, pp. 282–290, Oct. 2016, doi: 10.1016/j.addma.2016.05.009.

[8] J. Ning, D. E. Sievers, H. Garmestani, and S. Y. Liang, “Analytical modeling of part porosity in metal additive manufacturing,” Int. J. Mech. Sci., vol. 172, p. 105428, Apr. 2020, doi: 10.1016/j.ijmecsci.2020.105428.

[9] J. Ning, W. Wang, B. Zamorano, and S. Y. Liang, “Analytical modeling of lack-of-fusion porosity in metal additive manufacturing,” Appl. Phys. A, vol. 125, no. 11, p. 797, Nov. 2019, doi: 10.1007/s00339-019-3092-9.

[10] W. J. Sames, F. Medina, W. H. Peter, S. S. Babu, and R. R. Dehoff, “Effect of Process Control and Powder Quality on Inconel 718 Produced Using Electron Beam Melting,” in 8th International Symposium on Superalloy 718 and Derivatives, John Wiley & Sons, Ltd, 2014, pp. 409–423.

[11] M. M. Attallah, R. Jennings, X. Wang, and L. N. Carter, “Additive manufacturing of Ni-based superalloys: The outstanding issues,” MRS Bull., vol. 41, no. 10, pp. 758–764, Oct. 2016, doi: 10.1557/mrs.2016.211.

[12] C. Zhao et al., “Real-time monitoring of laser powder bed fusion process using high-speed X-ray imaging and diffraction,” Sci. Rep., vol. 7, no. 1, Art. no. 1, Jun. 2017, doi: 10.1038/s41598-017-03761-2.

[13] R. Cunningham, S. P. Narra, T. Ozturk, J. Beuth, and A. D. Rollett, “Evaluating the Effect of Processing Parameters on Porosity in Electron Beam Melted Ti-6Al-4V via Synchrotron X-ray Microtomography,” JOM, vol. 68, no. 3, pp. 765–771, Mar. 2016, doi: 10.1007/s11837-015-1802-0.

[14] R. Cunningham, S. P. Narra, C. Montgomery, J. Beuth, and A. D. Rollett, “Synchrotron-Based X-ray Microtomography Characterization of the Effect of Processing Variables on Porosity Formation in Laser Power-Bed Additive Manufacturing of Ti-6Al-4V,” JOM, vol. 69, no. 3, pp. 479–484, Mar. 2017, doi: 10.1007/s11837-016-2234-1.

[15] L. N. Carter, K. Essa, and M. M. Attallah, “Optimisation of selective laser melting for a high temperature Ni-superalloy,” Rapid Prototyp. J., vol. 21, no. 4, pp. 423–432, Jan. 2015, doi: 10.1108/RPJ-06-2013-0063.

[16] V. Juechter, T. Scharowsky, R. F. Singer, and C. Körner, “Processing window and evaporation phenomena for Ti–6Al–4V produced by selective electron beam melting,” Acta Mater., vol. 76, pp. 252–258, Sep. 2014, doi: 10.1016/j.actamat.2014.05.037.

[17] B. Zhang, S. Liu, and Y. C. Shin, “In-Process monitoring of porosity during laser additive manufacturing process,” Addit. Manuf., vol. 28, pp. 497–505, Aug. 2019, doi: 10.1016/j.addma.2019.05.030.

[18] J. A. Slotwinski and E. J. Garboczi, “Porosity of additive manufacturing parts for process monitoring,” AIP Conf. Proc., vol. 1581, no. 1, pp. 1197–1204, Feb. 2014, doi: 10.1063/1.4864957.

[19] W. Ren and J. Mazumder, “In-situ porosity recognition for laser additive manufacturing of 7075-Al alloy using plasma emission spectroscopy,” Sci. Rep., vol. 10, no. 1, Art. no. 1, Nov. 2020, doi: 10.1038/s41598-020-75131-4.

[20] J. A. Slotwinski, E. J. Garboczi, and K. M. Hebenstreit, “Porosity Measurements and Analysis for Metal Additive Manufacturing Process Control,” J. Res. Natl. Inst. Stand. Technol., vol. 119, pp. 494–528, Sep. 2014, doi: 10.6028/jres.119.019.

[21] P. Soille, Morphological Image Analysis: Principles and Applications, 2nd ed. Berlin Heidelberg: Springer-Verlag, 2004.

[22] G. M. Weiss and F. Provost, “The effect of class distribution on classifier learning: an empirical study,” Aug. 2001, doi: 10.7282/t3-vpfw-sf95.

[23] T. Wang, Z. Qin, Z. Jin, and S. Zhang, “Handling over-fitting in test cost-sensitive decision tree learning by feature selection, smoothing and pruning,” J. Syst. Softw., vol. 83, no. 7, pp. 1137–1147, Jul. 2010, doi: 10.1016/j.jss.2010.01.002.

[24] E. J. Schwalbach, S. P. Donegan, M. G. Chapman, K. J. Chaput, and M. A. Groeber, “A discrete source model of powder bed fusion additive manufacturing thermal history,” Addit. Manuf., vol. 25, pp. 485–498, Jan. 2019, doi: 10.1016/j.addma.2018.12.004.

[25] M. Uchic et al., “An Automated Multi-Modal Serial Sectioning System for Characterization of Grain-Scale Microstructures in Engineering Materials,” in Proceedings of the 1st International Conference on 3D Materials Science, Cham, 2016, pp. 195–202, doi: 10.1007/978-3-319-48762-5_30.

[26] J. Kittler, J. Illingworth, and J. Föglein, “Threshold selection based on a simple image statistic,” Comput. Vis. Graph. Image Process., vol. 30, no. 2, pp. 125–147, May 1985, doi: 10.1016/0734-189X(85)90093-3.

[27] M. H. F. Wilkinson, “Optimizing Edge Detectors for Robust Automatic Threshold Selection: Coping with Edge Curvature and Noise,” Graph. Models Image Process., vol. 60, no. 5, pp. 385–401, Sep. 1998, doi: 10.1006/gmip.1998.0478.

[28] P. Virtanen et al., “SciPy 1.0: fundamental algorithms for scientific computing in Python,” Nat. Methods, vol. 17, no. 3, Art. no. 3, Mar. 2020, doi: 10.1038/s41592-019-0686-2.

[29] F. Pedregosa et al., “Scikit-learn: Machine Learning in Python,” J. Mach. Learn. Res., vol. 12, no. 85, pp. 2825–2830, 2011.

5. CONCLUSIONS

5.1 Conclusions

This work shows the ability of creating gradients to avoid detrimental phases. This was first performed in 3 powder space with Cr, 316SS, and Ni demonstrating both the ability and the necessity of avoiding detrimental phases such as sigma. This research shows that this methodology could be translated to tangible functional gradients with no detrimental phases even after heat treatment. The four-powder system shows the ability to extend path planning into a more complex space, demonstrating the need for a robust printing methodology for powders that vary in thermodynamic properties. This printing path planning method was applied to a complex gradient and successfully avoided the predicted detrimental phases. However, the results also highlight the need to expand algorithm to avoid all predictable detrimental phases, since stochastic events can still occur during printing. Overall, printing the predicted computational path is an effective methodology for preventing failure in functional gradients.

This work also demonstrates the relationship between heat input and the resulting microstructure, establishing a methodology that allows heat induced microstructural features to be identified though their thermal features. The method's identification potential was successfully demonstrated on a small set of porosity features. The discussion of the data preparation methodology demonstrates the method's robustness and shows its potential.

In summary, multiple methodologies were established for printing complex systems while accounting for predictable detrimental phases. Induced microstructures

can all be predicted with a large degree of success. Both of these methodologies help increase the probability of successfully printing novel parts.

5.2 Future Work

The next step in the gradient work is to expand this research into other functional gradients that have applications in the real world. One of the main focuses should be a stainless-steel gradient to aluminum, which is of strategic importance in the aerospace industry, specifically because of the strength of steel and the lightness of aluminum.

However, steel and aluminum form brittle intermetallics when the two materials are combined and tend to crack because of the brittle phases. The stainless-steel to aluminum functional gradient is an ideal system for the expansion of the methodology specifically due to the number of intermetallics that can form. The proposed path could consist of Fe, Ni, Cr, Ti, and Al. The biggest concern is that while Al has a melting point of 660.3°C, it has a very high reflectivity. Therefore, when Al particles are hit with a laser, most of the energy is reflected and not absorbed into the particle to heat it up. This would require the use of more powerful lasers while printing Al which would result in the vaporization of the higher melting particles like Cr, Ni, and Fe. To overcome this, the printing parameters need to be graded along with the composition in order to create geometrically accurate parts.

Alongside a new gradient, further study of the focal point's role in printing needs to be investigated. The focal point of the laser directly controls the spot size and therefore the amount of heat input. The larger the spot size, the more evenly the heat is

applied over the part for a longer time. This could be used to print difficult materials such as refractory alloys and aluminum.

Future work for the microstructure project focuses on expanding the training data set. This can be accomplished using one of three methods. The first method incorporates more slices of the previously printed part: pores are rare events and incorporating more slices would widen the data set. The second method expands the thermal histories' time to include thermal events from the next deposition layer: this would capture more features for training. The third method prints a variety of shapes that have vastly different printing strategies: this would allow for different types of porosity to be added to the training set. It would be best to include all three methods, as this would offer the most robust data set. Furthermore, the porosity data set is easily identifiable, but this methodology can easily be extended to other thermally activated microstructural features such as grain size.

APPENDIX A

COMPUTATIONAL DESIGN OF PATH-PLANNING ALGORITHM

A.1 Computational Methodology for the Design of Functional Gradients

The formation of undesired intermetallic phases that are detrimental to mechanical properties is a significant challenge in the manufacturing of compositionally graded alloys. Due to the creation of a localized melt pool during direct energy deposition (DED) additive processes (including LENS technology) and the subsequent rapid solidification, the microstructure of additively manufactured materials, in terms of present phases, often deviates from what can be expected under equilibrium conditions. As such, CALPHAD based computational thermodynamics software cannot accurately predict the exact phase constitution of as-built AM materials. However, one can examine equilibrium CALPHAD predictions over a wide range of temperatures to predict all the possible phases that might form at a given composition, at any stage of fabrication or post-processing. By ensuring detrimental phases are not predicted to appear in this wide range of temperatures, designed FGMs can be made more robust with respect to phase kinetics and potential heat treatments. Increasing the dimensionality of the search space to include temperature severely limits the possibility to visualize a potential gradient path. The difficulty of visualizing the design space would also increase dramatically as more elements are added to the FGM. In order to design FGMs that occupy such high dimensional spaces it is therefore necessary to use computational design methods that are not limited by the inability of humans to navigate spaces of N3 dimensions.

Representing FGM design philosophies, like avoiding detrimental phases, preventing steep stress gradients, or achieving desired properties, in an algorithmic manner will therefore allow materials scientists to take full advantage of computational models.

Before implementing the proposed methodology algorithmically, the FGM design problem was formalized as an optimization problem, as shown in Kirk et al. [23]. Consider the composition space of the FGM as the state space Z^d with dimensionality d equal to the total number of unique relevant elements. A point z in the state space is defined by the fractions of each of the relevant elements, as shown in Eq. (1), where the total composition must sum to unity and no fraction can be less than zero or greater than unity.

$$z = \left\{x_1, \ldots, x_d : \sum_{i=1}^{d} x_i = 1 \text{ and } x_i \geq 0 \; \forall \; i\right\} \quad (1)$$

Let p_u (z, T)$\rightarrow$ [0, 1] be a function (e.g. a CALPHAD model) that maps a unique composition (a point z in state space Z^d) at temperature T to an estimated fraction of undesirable phase u. Subsequently, let $Z_{\text{obs}} \subset Z^d$ (obs: obstacle) be defined as the region of composition space where the predicted undesirable phase fraction, p_u, exceeds a user-defined allowable λ_u for any temperature, $T \in [T_r, T_m]$, from room temperature, T_r, to manufacturing temperature, T_m, as seen in Eq. (2). This obstacle region, Z_{obs}, provides a conservative estimate of the compositions that might produce undesirable phases at any temperature during the complicated thermal history of an additive manufacturing process.

$$Z_{\text{obs}} = \{z : \; p_u(z,T) > \lambda_u \; \exists \; u,T\} \quad (2)$$

Next, let the complement of the obstacle region, $Z_{\text{free}} = Z^d \backslash Z_{obs}$, rep- esent the free space. As shown in Eq. (3), the free space represents the region of the composition

space where the predicted undesirable phase fraction is below the user-defined allowable, λ_u, for all temperatures be- tween room temperature and the manufacturing temperature.

$$Z_{\text{free}} = \{z : p_u(z,T) \leq \lambda_u \; \forall \; u,T\} \tag{3}$$

Let the continuous function $\sigma : [0, 1] \rightarrow z$ be a path in composition space. This path represents the compositions of a gradient between two materials. This path is collision-free if and only if $\sigma(\alpha) \in Z_{free} \forall \; \alpha \in [0,1]$ or, in other words, if every composition in the gradient material is predicted to produce a fraction of undesirable phases that is less than or equal to the allowable fraction in the temperature range defined. Let z_{init} and z_{goal} be two target materials at each end of an FGM. A path, σ, is a feasible design for the FGM if it is collision-free and $\sigma(0) = z_{init}$ and $\sigma(1) = z_{goal}$.

Lastly, let $c : \sigma \rightarrow R_{\geq 0}$ be a cost function that relates a path to a strictly positive cost. The cost returned by this cost function is zero if and only if $\sigma(\alpha) = \sigma(0) \; \forall \; \alpha \in [0, 1]$ (i.e. the path is a single point). The objective of the proposed FGM design methodology is to find the path in composition space, σ_{best}, that minimizes this cost function while also avoiding undesirable phases. In other words, σ_{best} is the argument that minimizes the cost function $c(\sigma)$ subject to path feasibility constraints. This objective is summarized in the optimization problem formulation below.

$$\textbf{Find} \qquad \sigma_{\text{best}} = \underset{\sigma}{\textbf{argmin}}\, c(\sigma)$$

$$\textbf{subject to} \quad \sigma(\alpha) \in Z_{\text{free}} \forall \alpha \in [0,1]\,,$$
$$Z_{\text{free}} = \{z : p_u(z,T) \leq \lambda_u \forall\, u,T\}\,, \qquad (4)$$
$$T \in [T_r, T_m]\,,$$
$$\sigma(0) = z_{\text{init}}\,,$$
$$\sigma(1) = z_{\text{goal}}$$

This problem formulation shares many characteristics with the motion planning problem formulation in the robotics community [36]–[38]. As such, a motion planning algorithm was adapted to execute this problem formulation computationally. Motion planning algorithms plan a robot's motion in its environment such that obstacles are avoided and path length, or some other cost which can be computed as a function of the path taken, is minimized [39]–[41]. By applying these algorithms to composition space, FGM gradient paths can be designed that avoid detrimental phase regions and are optimal with respect to some cost function.

Most motion planning algorithms require either a complete, explicit representation of the obstacles in the environment (detrimental phases in composition space) or numerous samples of the environment (often in the tens of thousands for just a 2D space) [41]–[43]. As CALPHAD software will be used to predict the presence of detrimental phases for a given composition and temperature, sampling CALPHAD models directly could become prohibitively expensive, especially in large compositional spaces (3+ elements). To reduce the number of samples needed from phase equilibrium predictions to represent the detrimental phase region(s), thermodynamic spaces defined by CALPHAD models were efficiently sampled by a Constraint Satisfaction Algorithm

(CSA) developed by Galvan et al. [44] for the identification of specific phase regions in multicomponent systems. The CSA has been shown be- fore to be effective in identifying arbitrary, designed-for, phase constitutions in high entropy alloy (HEA) systems [45]. Given initial samples, the CSA creates a Support Vector Data Description (SVDD) [46], a machine-learning classifier similar to a support vector machine [47], [48]. That classifies the region of interest as containing detrimental phases. The CSA then grows the SVDD by sampling the thermodynamic space along directions perpendicular to the SVDD boundary in the region where the boundary is least defined. Once trained in this manner, the SVDD can be cheaply evaluated to classify points in composition- temperature space as lying in the detrimental phase region or not. In this way, the CSA uses a minimal number of samples derived from thermodynamic equilibrium calculations to create a representation of the detrimental phases that is much cheaper to evaluate than the use of the thermodynamic model directly.

With a model of detrimental phase regions that can be cheaply evaluated, many of the motion planning algorithms that require numerous samples of the environment could be used. The Rapidly-Exploring Random Tree (RRT) [36], [41] class of algorithms was chosen for its general applicability and scalability to high dimensional spaces. More specifically, a fixed-node implementation of the optimal RRT [36] (RRT*FN) developed by Adiyatov et al.[37] was used as it can find paths that are optimal to some cost function while remaining under a preset limit on computational expense. In short, the RRT*FN builds a tree of nodes by sampling the environment randomly. New samples are connected to the node in the tree that minimizes cost (i.e.

the parent node). In the basic case where the cost is path length, the parent node is simply the node nearest to the candidate node. Connections are only allowed if no obstacles lie along the line connecting the candidate node and the parent node. To check if any obstacles lie along the connection, the connection is discretized into a fixed number of points that are then evaluated by the obstacle model provided by the CSA. If any point contains detrimental phases, the connection is said to collide with an obstacle and is disallowed.

After a new node is connected to the tree, an optimization routine rewires the connections between the nodes to optimize the path cost globally. This process is repeated until a complete path be- tween target compositions is found to minimize the given cost function. A visual summary of this process can be seen in Figure 34.

Figure 35 summarizes the computational methodology used in this work for the design of FGMs. First, a CSA is used to sample the thermodynamic space defined by CALPHAD models and create a simplified model of where detrimental phases lie in composition space. A motion planning algorithm (RRT*FN) is then used to find a path in composition space be- tween two materials that does not contain these detrimental phases. The resulting path represents the compositions of the optimized gradient material. More information about the design problem formulation and the algorithms used within the methodology can be found in Kirk et al. [23].

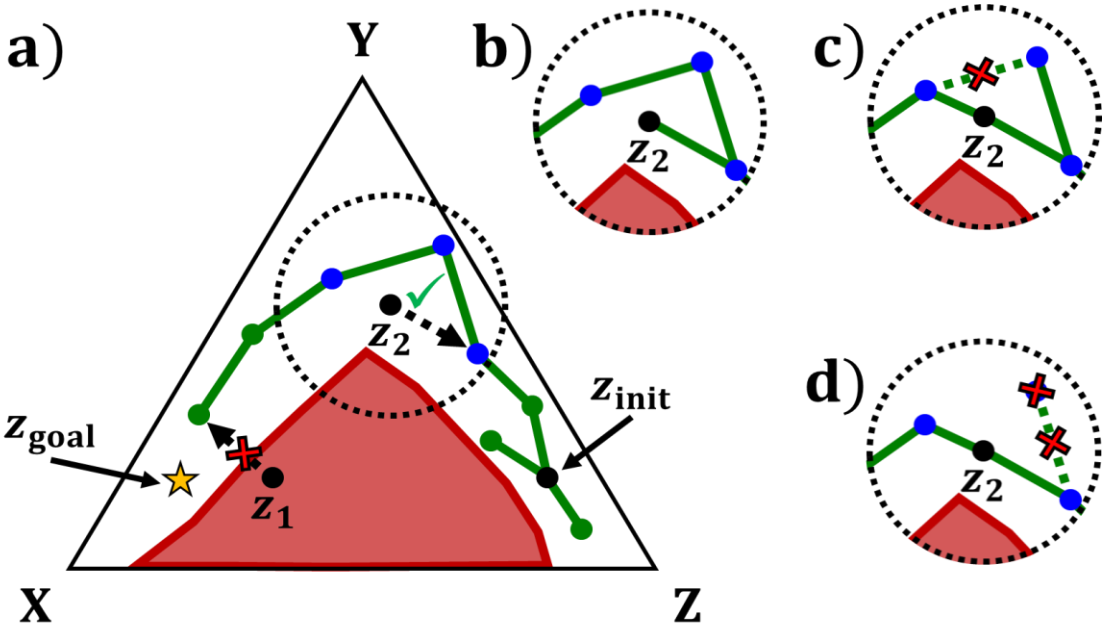

Figure 32. a) A simplified example of the RRT*FN algorithm. Consider point z1 to have been randomly sampled from the composition space of elements X, Y, and Z. A connection is attempted to the existing tree, but the connection is not allowed because point z1 is in the obstacle region containing undesirable phases. Consider another randomly sampled point z2 that is not in the obstacle region. Neighboring nodes in the existing tree within a defined distance (shown as a dashed circle) of the newly sampled point are examined for connection to point z2. b) The node that minimizes path cost (path length in this case) to zinit is chosen to connect with z2 and the connection passes because the connecting segment does not intersect the obstacle region. c) At a future "rewiring" step, a new connection is made to z2 that reduces the cost of the path to another node in the tree. d) If the fixed number of allowed nodes is exceeded in the tree, extraneous nodes are removed during the "removal" step.

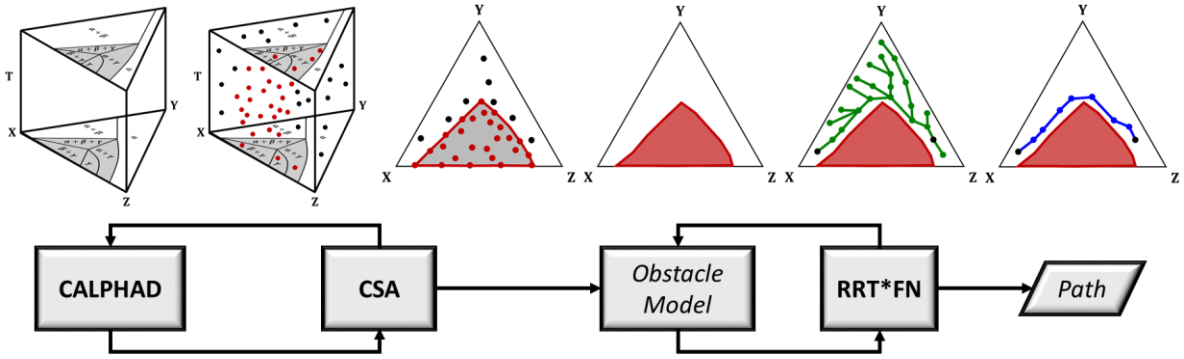

Figure 33. Flow diagram that summarizes the model sequence in the proposed methodology for designing Functionally Graded Materials (FGMs) without forming detrimental phases. A Constraint Satisfaction Algorithm (CSA) samples CALPHAD software to form an obstacle model that represents detrimental phase locations in composition-temperature space. This model is then sampled by the motion planning algorithm to plan a path. RRT*FN: Rapidly-Exploring Random Tree algorithm with a Fixed-Node implementation.

To validate the viability of the method introduced above, a case study was conducted in the iron-nickel-chromium (Fe-Ni-Cr) system. This system was chosen given its relevance to many alloys of interest to the additive manufacturing community, including Inconel type alloys and stainless steels. In the first step, two detrimental intermetallic phases, σ phase and $CrNi_2$, were identified by examining literature and conducting a dense sampling of the CALPHAD model in composition-temperature space. Precipitation of the σ phase with a tetragonal crystal structure leads to loss of ductility and toughness in stainless steels [24]. The $CrNi_2$ phase with an orthorhombic structure is an incoherent intermetallic precipitate and causes embrittlement.

More than 500,000 samples of Thermo-Calc's TCHEA2 database[49], [50] were considered in an equally spaced grid sampling of the Fe- Ni-Cr space from 300 to 1100

K. These samples were used to visualize the locations of $CrNi_2$ and σ phase in the Fe-Ni-Cr ternary phase diagram, as seen in Figure 34a. From this, it can be observed that each phase occurs at a different temperature regime: $CrNi_2$ appears at lower temperatures (300–700 K) while the σ phase occurs at higher temperatures (700–1100 K). For this reason, it would be difficult to accurately visualize these phases in a single isothermal ternary phase diagram. However, after projecting the maximum phase fractions encountered in the temperature dimension onto the composition plane, a 2-D visualization of the locations of both phases in thermodynamic space can be achieved, as seen in Figure 34b. Note that the phase fraction of $CrNi_2$ in- creases as compositions near its compound line (approx. 33% Cr and 67% Ni) and, similarly, σ phase fraction increases to a maximum as com- positions approach the center of the σ phase stability area (pointed by arrows in Figure 34b).

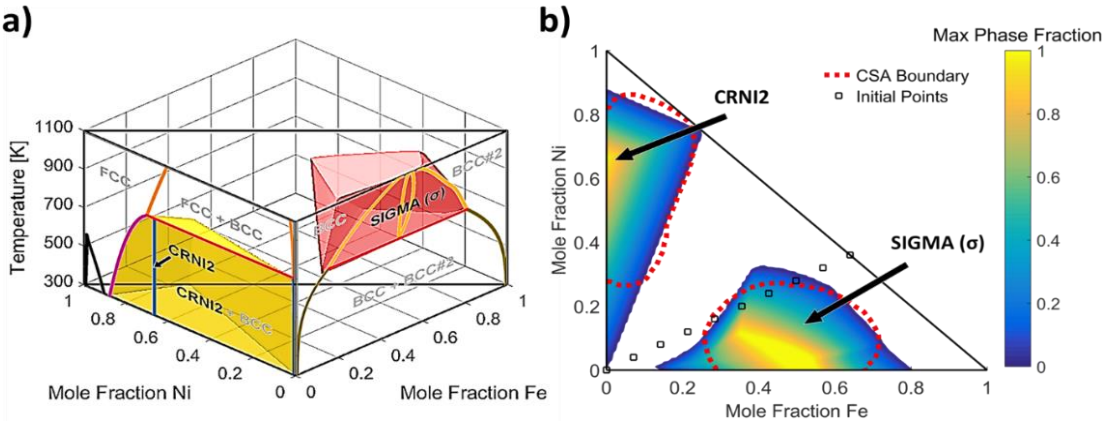

Figure 34. A3. a) A visualization of the locations of $CrNi_2$ and σ phases in the Fe-Ni-Cr thermodynamic space. The Cr-Ni and Cr-Fe binary phase diagrams are shown on the Ni-T and Fe-T planes respectively to assist in visualization. b) The maximum phase fractions of $CrNi_2$ and σ phases projected in the temperature dimension from 300 to 1100 K. The boundary estimated by the Constraint Satisfaction Algorithm (CSA) and the starting points used to initialize the CSA (taken at 1100 K) are also shown.

Before path planning, the CSA was used to construct an approximate model of the locations of both phases in the phase diagram. Initialized with just ten points at 1100 K, shown in Figure 34b, the CSA adaptively sampled the CALPHAD-defined thermodynamic space (using Thermo-Calc's TCHEA2 database [49], [50] to approximate the locations where the phase fractions of $CrNi_2$ and σ phase exceed 1 mol%. Figure 34b shows the CSA estimate of the phase region boundaries after 3000 samples. The CSA boundaries generally underestimate the size of the true phase regions, but the regions missed by the CSA have smaller phase fractions (most are b30%). This example of the CSA is the most general case as few initial points were provided and both phase regions were found simultaneously. In Kirk et al. [23], the CSA was applied to the same system and phases, but the CSA boundaries were shown to nearly match the true boundaries. In that work, the CSA was applied to each phase separately with initial

examples of both phases. The CSA boundaries used in this work, those in Figure 34b, represent the more general case where initial samples of phase locations in thermodynamic space might not be known.

After obtaining the CSA descriptions of undesirable phase boundaries, the composition space was further constrained to only include alloys that can be fabricated using the combination of 316L stainless steel, pure nickel, and pure chromium powders. This constraint can be visualized as the dashed lines in Figure 35. Given these constraints, the RRT*FN algorithm was used to plan gradient paths. Two cost functions were considered that each expressed different design priorities. The first cost function sought simply to find the shortest feasible path between 316L stainless steel and pure chromium while avoiding the undesirable phases. This cost function is shown in Eq. (5), where l_k is the length of the kth segment in the path and n is the total number of segments in the path. This path could be desired if it is important that the number of interlayers be minimized, which could be the case if the part size must be small.

$$c_1(\sigma) = \sum_{k=1}^{n} l_k \tag{5}$$

The second cost function seeks to find a gradient path that is robust to processing-induced compositional variability. To reduce the chance of producing deleterious phases, the distance from the path to deleterious phase boundaries is maximized by minimizing Eq. (6), where $d_{\text{avg, }k}$ is the average distance between the kth segment and the nearest phase boundary.

$$c_2(\sigma) = \sum_{k=1}^{n} \frac{1}{d_{\text{avg},k}} \tag{6}$$

The results of the RRT*FN based path planning for both cost functions can be seen in Figure 35. Figure 35a depicts the shortest possible path be- tween 316L stainless steel and pure chromium as calculated from Eq. (5), which also requires the smallest change in compositions. Figure 35b shows the path that minimizes Eq. (6) and consequently in- creases the separation of the path from the $CrNi_2$ and σ phase regions. Since compositional control in a multi-powder direct energy deposition process is not precise, the second path was chosen to be printed and experimentally validated.

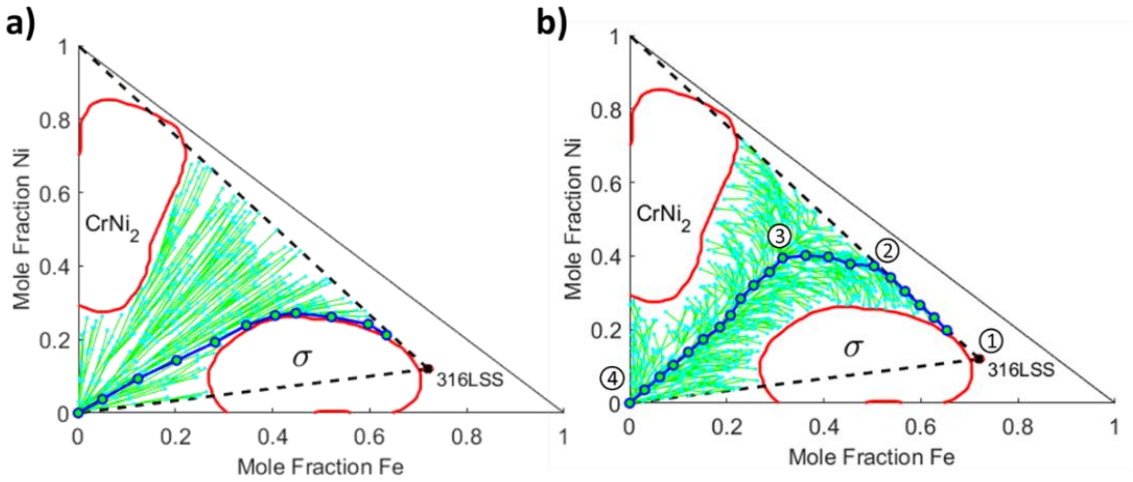

Figure 35. a) The tree created by the RRT*FN algorithm (see text for details) when minimizing the path length to go from 316L stainless steel to pure chromium in the Fe-Cr-Ni phase map while avoiding both $CrNi_2$ and σ phases, as estimated by the Constraint Satisfaction Algorithm. The optimal path is shown in blue. b) The tree created by the RRT*FN algorithm when maximizing the distance from the undesirable phase regions. The optimal path is shown in blue. The numbered points represent the vertices of the simplified path used for experimental validation.

APPENDIX B

PATH PLANNING METHODOLOGY FOR FGM DESIGN

B.1 Path Planning Methodology for FGM Design

The methodology presented in Kirk et al. [30] is summarized in Figure 36. The methodology begins by defining a composition space and target compositions for each end of the desired gradient. Once the design space is defined, information about the space needs to be collected. CALPHAD models are used as the primary information source as they can predict equilibria phase information, which is often the most critical indicator of build success. However, CALPHAD models and other materials models often have an associated computational expense that prohibits the direct use of path planning algorithms, which often require millions of samples. In order to facilitate the use of path planning, cheaper surrogate models must be created to replicate CALPHAD and other relevant models. In the methodology, this is generally done by first sampling CALPHAD throughout the composition space, labeling compositions that violate the constraints, and then training a machine learning classifier. The trained classifier can then be used as a representation of the obstacle region, or the region in composition

space that violates the design constraints. In the current work, a k-nearest neighbors classifier is used given its simplicity and scalability.

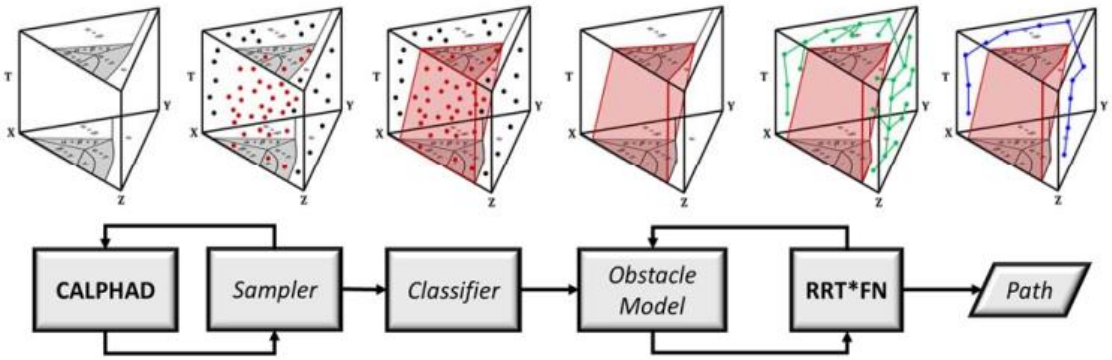

Figure 36. Flowchart depicting the path planning methodology for FGM design presented in Kirk et al.[30]

After the obstacle region has been modeled, a path planning algorithm can be used to find the optimal gradient path. In the current work, a fixed nodes implementation of the Rapidly-Exploring Random Tree algorithm (RRT*FN) [32], [33] is used to plan the gradient paths. Put simply, this algorithm randomly samples the composition space to form a connected tree of nodes or compositions. Connections are made only if they do not intersect with the obstacle region. Connections are also made to minimize the cost function. The cost function is defined by the designer and used to express gradient design objectives. As the number of samples taken by RRT*FN increases to infinity, it is proven to find a feasible path if one exists (i.e. probabilistically complete) and will also find the path that minimizes the cost function (i.e. asymptotically optimal) [32]. The ultimate result of the path planning algorithm is a gradient path through composition space that satisfies the design constraints and optimizes the design objective.

B.2 Phase Equilibria

To avoid the deleterious phases present in the linear Fe9Cr to W gradient, it is necessary to consider additional elements in the search for a feasible gradient path. Preliminary exploration found that adding small amounts of aluminum can destabilize the sigma phase that tends to form at compositions rich in Fe and Cr. Similarly, vanadium was determined to destabilize the laves and mu phases, but stabilize sigma phase. Due to vanadium's expense and difficult of acquisition in comparison to the other elements in this system, it was decided to only consider the Fe-Cr-W-Al system in this work.

Once the design space was chosen, samples of relevant thermodynamic information were gathered from Thermo-Calc's TCHEA2 database. More than 275,000 uniform random samples were taken from the Fe-Cr-W-Al composition space and a uniform temperature distribution from 300 to 3700 K (the melting point of pure W is 3695 K). Phase equilibria were predicted at these samples to determine where deleterious phases (e.g. sigma, laves, mu) are located.

B.3 Solidification Range

The solidification range of an alloy is a predictor of its suitability for additive manufacturing. In general, smaller solidification ranges are desirable as they reduce the potential for hot cracking, a phenomenon common in casting processes and also additive manufacturing[34], [35]. Hot cracking, or tearing, occurs when liquid and solid phases coexist for an extended period, particularly near the end of solidification. As

solidification range decreases, the time spent in the two-phase liquid-solid phase region also decreases, reducing the likelihood of hot cracking.

In this system, solidification range is of particular interest because of large differences in the melting temperatures of the relevant elements. Pure W has a melting point of 3695 K while Fe, Cr, and Al have melting points of 1808 K, 2130 K, and 933 K respectively. These differences can lead to large solidification ranges as W will solidify well before elements with lower melting temperatures.

To estimate the solidification ranges of compositions in the Fe-Cr-W-Al system, Thermo-Calc was used to perform equilibrium solidification calculations for over 60,000 uniform random compositions. Ten thousand of these compositions were used to train a gaussian process regression model that predicts solidification range when given composition. This model was tested on the remaining data and was found to have a coefficient of determination (R^2) of 0.996 and a Root Mean Square Error (RMSE) of 32.6 K on the test set.

B.4 Hot Cracking Susceptibility

In an effort to predict hot cracking more accurately than simply predicting solidification range, QuesTek has developed a proprietary Hot Cracking Susceptibility (HCS) criterion. Like other cracking susceptibility metrics reported in literature[34], [36], HCS considers the fraction of solidification time spent on the final stages of solidification. However, QuesTek's HCS also considers the solidification range and the grain size of candidate alloys in its prediction of hot cracking. The exact form and values of this equation will not be detailed to protect QuesTek's intellectual property.

A surrogate model for Hot Cracking Susceptibility was created by first performing Scheil solidification simulations in Thermo-Calc. Scheil simulations[37] limit the diffusion in the solid phases and therefore more accurately model solidification than typical equilibrium calculations [38]. However, Scheil simulations also take about two to three orders of magnitude more time to perform than simple equilibrium calculations. For this reason, only 1082 simulations were run for randomly selected compositions in the Fe-Cr-W-Al system. HCS was calculated from these simulations using Equation 1. A gaussian random process regressor was trained on a randomly selected subset of 1000 compositions. The model had a coefficient of determination (R^2) of 0.803 and a Root Mean Square Error (RMSE) of 21.5 when tested on a test set formed from the remaining 82 compositions.

B.5 FGM Optimization Problem

The path planning methodology detailed in Figure 36 was applied to the Fe-Cr-W-Al space to find an optimal gradient that maximized performance objectives and satisfied constraints. In the methodology, a potential gradient is represented as a path, σ. Equation 2 demonstrates that an arbitrary point in this path at some index, $\alpha \in [0,1]$, represents a set of compositions of each element in Fe-Cr-W-Al space, where the compositions of Cr, W, and Al are represented explicitly and Fe is the balance element. A total path, from σ(0) to σ(1), therefore represents a continuous sequence of compositions (i.e. a compositional gradient).

$$\sigma(\alpha) = \{x_{\mathrm{Cr}}, x_{\mathrm{W}}, x_{\mathrm{Al}} : x_{\mathrm{Fe}} = 1 - \textstyle\sum_{i=1}^{3} x_i \text{ and } x_i \geq 0 \; \forall \; i\} \quad (2)$$

The objective of the gradient design methodology was to find the shortest length path that satisfied the constraints. Shorter gradient paths are desirable because shorter gradients can lead to less material use and smaller parts. The length of each linear segment in the path, l_k, was calculated as the Euclidean distance between the compositions at each end of the segment. All n segment lengths were then summed to compute a total path length which was used as the cost function, $c(\sigma)$, considered by the path planning algorithm.

Multiple constraints were considered in the optimization problem formulation. First, a model of phases near each composition's solidus temperature, T_{solidus}, was created from the more than 60,000 Thermo-Calc solidification calculations used to create the solidification range model. The first constraint uses this model to ensure that the path does not form any significant deleterious phase fraction (f < 0.01) near its solidus temperature or, in other words, just after solidifying during the manufacturing process. Collapsed temperature models were constructed from the initial sampling of over 275,000 composition-temperature combinations. These models were used to ensure the path avoided deleterious phases at all temperatures from 300 to 3700 K. Constraints on the sigma and intermetallic phases were set to be less 0.01 phase fraction as these phases are easily avoidable. The constraint on laves phase was set to be less than 0.10 to accommodate the close proximity of laves phase to Fe9Cr. Lastly, the constraint on mu phase was set to be less than 0.50. This constraint on mu phase is necessarily relaxed in comparison to the other phases due to the pervasiveness of mu phase in the composition space. A more restrictive constraint would eliminate all but the boundaries of the

composition space and create an insurmountable obstacle for the path planning algorithm in its current state.

In addition to phase constraints, constraints were also placed on solidification range, $\Delta T_{\text{solidification}}$, and Hot Cracking Susceptibility (HCS) in order to promote manufacturabilty of the gradient. Due to the large melting point differences in the design space, feasible paths were constrained to experience a maximum solidification range of less than 900 K, as lower constraints are unlikely to be met in the W-rich portions of the space. The maximum allowable HCS was chosen in a similar fashion. The gradient design problem formulation is summarized below.

$$\textbf{find} \quad \sigma_{\text{best}} = \underset{\sigma}{\text{argmin}} \left[c(\sigma) = \sum_{k=1}^{n} l_{\text{k}} \right]$$

$$\begin{aligned}
\textbf{s.t.} \quad & f_{\text{mu}}(\sigma, T), f_{\text{sigma}}(\sigma, T), f_{\text{laves}}(\sigma, T), f_{\text{intermetallics}}(\sigma, T) < 0.01 \; \forall \; T \approx T_{\text{solidus}}, \\
& f_{\text{sigma}}(\sigma, T), f_{\text{intermetallics}}(\sigma, T) < 0.01 \; \forall \; T \in [300 \text{ K}, 3700 \text{ K}], \\
& f_{\text{laves}}(\sigma, T) < 0.10 \; \forall \; T \in [300 \text{ K}, 3700 \text{ K}], \\
& f_{\text{mu}}(\sigma, T) < 0.50 \; \forall \; T \in [300 \text{ K}, 3700 \text{ K}], \\
& \Delta T_{\text{solidification,max,}\sigma} < 900 \text{ K}, \\
& \text{HCS}_{\text{max,}\sigma} < \text{HCS}_{\text{allowable}}, \\
& \sigma(0) = \{x_{\text{Cr}} = 0.09, x_{\text{W}} = 0, x_{\text{Al}} = 0\}, \\
& \sigma(0) = \{x_{\text{Cr}} = 0, x_{\text{W}} = 1, x_{\text{Al}} = 0\}.
\end{aligned}$$

B.6 Issues with the Linear Gradient

The linear compositional gradient between Fe9Cr and pure W, shown in Figure 37a, is rife with undesirable, deleterious phases. Figure 37b shows equilibrium phase fractions along the path at various temperatures as predicted by Thermo-Calc's TCHEA2 database. From these plots, it is evident that the linear gradient experiences several

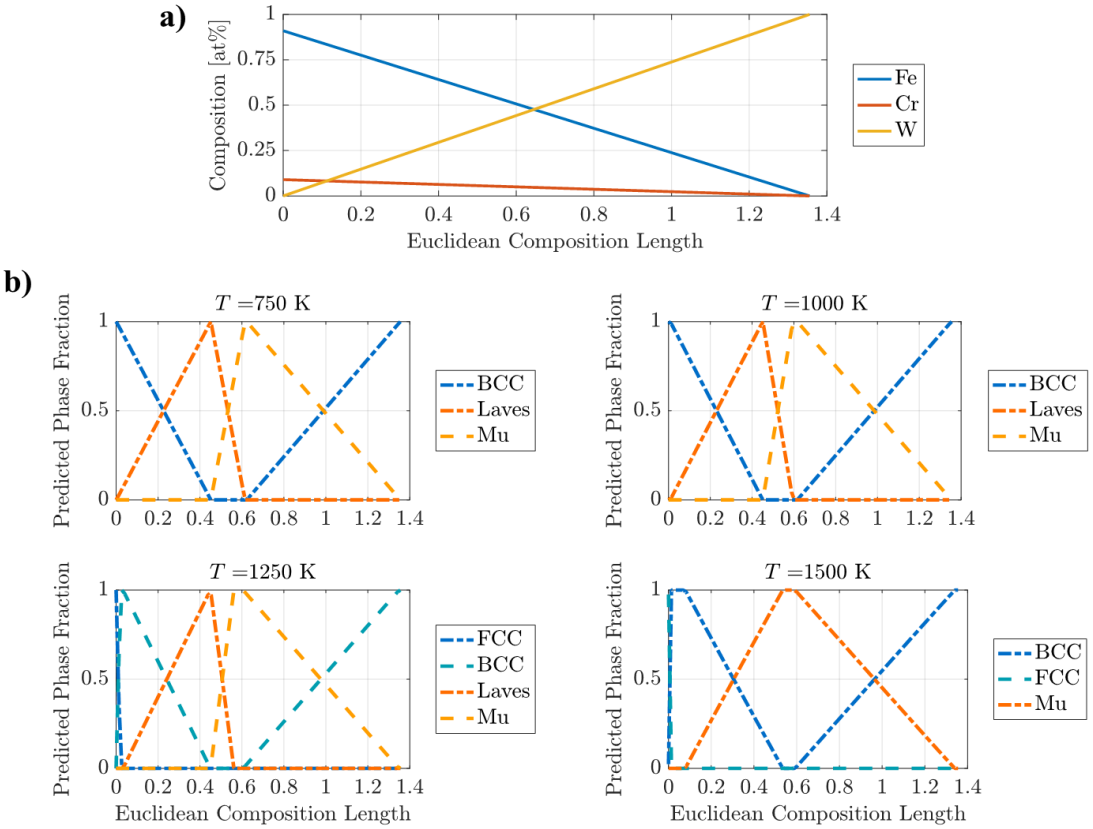

Figure 37. a) Compositions of the linear gradient path between Fe9Cr and pure W. The x-axis represents the length in composition space along the path from Fe9Cr to pure W. b) Equilibrium phase fractions along the linear gradient path at various temperatures.

regions of 100% phase fraction of both laves and mu phases. These phases are known to be brittle and can lead to cracking during the build and severely compromised parts.

B.7 Visualizations of Design Constraints

By collapsing the temperature dimension, phase regions can be visualized in three-dimensions as in Figure 38. The regions plotted in Figure 38 were found by training k-nearest neighbors classifiers (k=3) on the points sampled from composition-temperature space and then testing those classifiers on a full sampling of composition space at a

dense range of temperatures from 300 to 3700 K. These regions represent compositions which are predicted to form the relevant phase at *any* temperature from 300 to 3700 K.

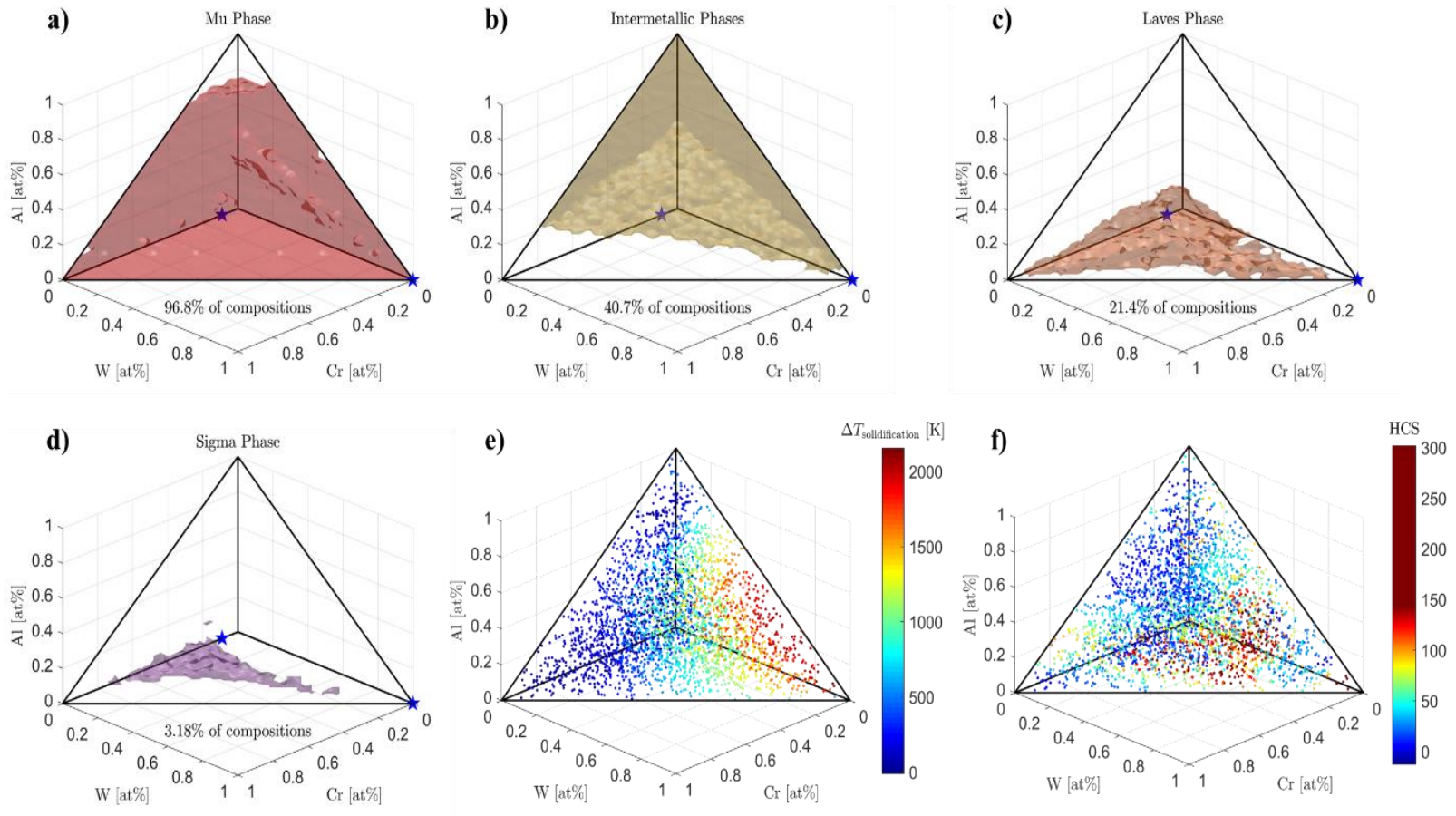

Figure 38. Visualizations of FGM constraints in Fe-Cr-W-Al space. Plots a)-d) show compositions with greater than 0.01 mole fraction of a) mu phase, b) intermetallic phases, c) laves phase, and d) sigma phase at any temperature between 300 and 3700 K. The endpoints of the gradient (Fe9Cr and pure W) are marked with stars. Plots e) and f) show the values of e) solidification range and f) Hot Cracking Susceptibility (HCS) criterion at various compositions.

Figure 38a depicts the region in Fe-Cr-W-Al space where mu phase is present (in greater than 0.01 mole fraction) at some temperature between 300 and 3700 K. Mu phase is present in 96.8% of the tested compositions, even those that are very close to the gradient endpoints (Fe9Cr and pure W). This is an issue if the gradient will experience the relevant temperatures long enough to approach equilibrium and produce mu phase. As seen in Figure 38a, there are very few possible gradient paths from Fe9Cr to pure W that could avoid mu phase at all possible temperatures. Figure 38b illustrates the region occupied by intermetallic phases (40.7% of compositions). This region dominates the Al-rich portion of the composition space. Also, less Al is needed to form intermetallics as compositions approach pure W. Figures 38c and 38d visualize the laves phase (21.4% of compositions) and sigma phase (3.18% of compositions) regions respectively. Both phases are common near the Fe-Cr-W ternary region but dissipate as the Al content increases. The laves phase is present at compositions very close to Fe9Cr, meaning it will be difficult to avoid the laves phase completely at all temperatures in compositions near Fe9Cr.

Figure 38e visualizes solidification range throughout the Fe-Cr-W-Al composition space. This visualization was created by using the gaussian process model to predict solidification range for 3,000 uniform random compositions. Figure 38e demonstrates that solidification range increases as compositions approach pure W and the difference between pure element melting points increases. The highest region of solidification range occurs near the Al-W binary edge where the difference in pure

element melting points is highest. Ultimately, a significant portion of the compositions in Fe-Cr-W-Al space have predicted solidification ranges above that of most successfully printed alloys (~10-200 K). As such, large solidification ranges are practically unavoidable in this system, but designed gradients should minimize solidification range as much as possible.

In a similar fashion to Figure 38e, Figure 38f was created by inputting 3,000 random compositions into the gaussian process model to visualize HCS in the Fe-Cr-W-Al system. While the trends in HCS are less obvious than those in solidification range, there are still definitive regions where HCS is highest. These regions are primarily centered around two locations. One region is where Cr and W are present in near equal proportions and other elements are present only in minor fractions. Similarly, another region of high HCS occurs where Fe and W are present in near equal proportions, but other elements are minimal. These regions are likely where a small fraction of an Al-containing phase is present which requires lower temperatures and therefore more time to solidify. Overall, there are many compositions with suitably low HCS, but the high HCS regions leave limited paths to approach pure W from Fe-rich compositions.

B.8 Path Planning Results

After 500,000 iterations of the path planning algorithm, the optimal path was determined to have the compositions shown in Figure 39a. The optimal path exploits Al in Fe-rich portion of the path to avoid sigma and laves and then transitions to significant amounts of Cr to satisfy constraints on solidification and mu phase. Figure 39b displays both the solidification range and predicted HCS along the optimal path. The

solidification range is predicted directly from Thermo-Calc, but the HCS is predicted from a gaussian process regressor. The maximum solidification range is shown to satisfy the constraint of less than 900 K, however the HCS constraint is shown to be met by most of the path, but eventually violated as the HCS exceeds the allowable near pure W.

This violation was not missed by the path planning algorithm, because the planned path stopped short of pure W, at around 70 at. % W. Usually, the end of the planned path can be simply connected to the goal composition, but that connection happened to violate a constraint in this case. Nevertheless, Figure 38f displays a cluster of high HCS compositions near pure W indicating that high HCS cannot be avoided in this region. As such, the optimal path was deemed to be remain the best feasible path. The phase fractions along the path at temperatures 100 K below the solidus temperature predicted by the machine learning model are shown in Figure 39c. These phase fractions were computed directly from Thermo-Calc, but the solidus temperature was approximated from a gaussian process regressor. This plot confirms that the first constraint on significant deleterious phase fractions near the solidus temperature was not violated by the algorithm.

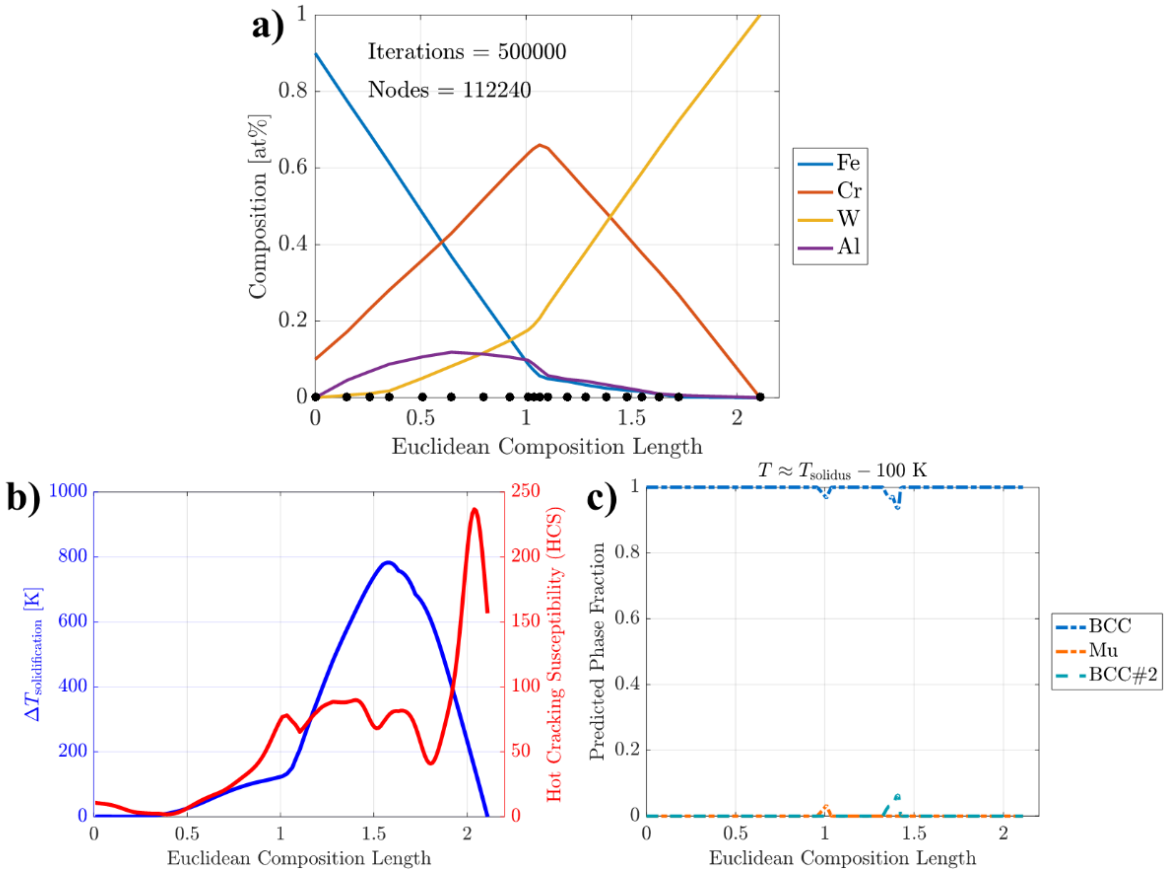

Figure 39. a) The optimal gradient path as planned by algorithm in Fe-Cr-W-Al space after 500,000 iterations. The black dots along the x-axis represent the actual points sampled by the path planner. b) Predicted solidification range and Hot Cracking Susceptibility along the optimal path. c) Predicted phase fractions along the path 100 K below the predicted solidus temperature.

Figure 40 shows equilibrium phase fractions along the optimal path at various temperatures. While deleterious phases are present at some of these temperatures, none of them violate the constraints set in the problem formulation. For example, at a temperature of 750 K, the optimal path experiences a maximum laves phase fraction of about 0.10 and a maximum mu phase fraction of 0.50. These values are the same values set as the maximum allowable phase fractions of their respective phases. Because the

objective of the design problem was to minimize path length, the optimal path will necessarily be the path closest to the constraint boundaries without violating the constraints. Other objectives, like obstacle clearance, could provide paths that are farther away from constraint boundaries if avoiding constraints is of high priority.

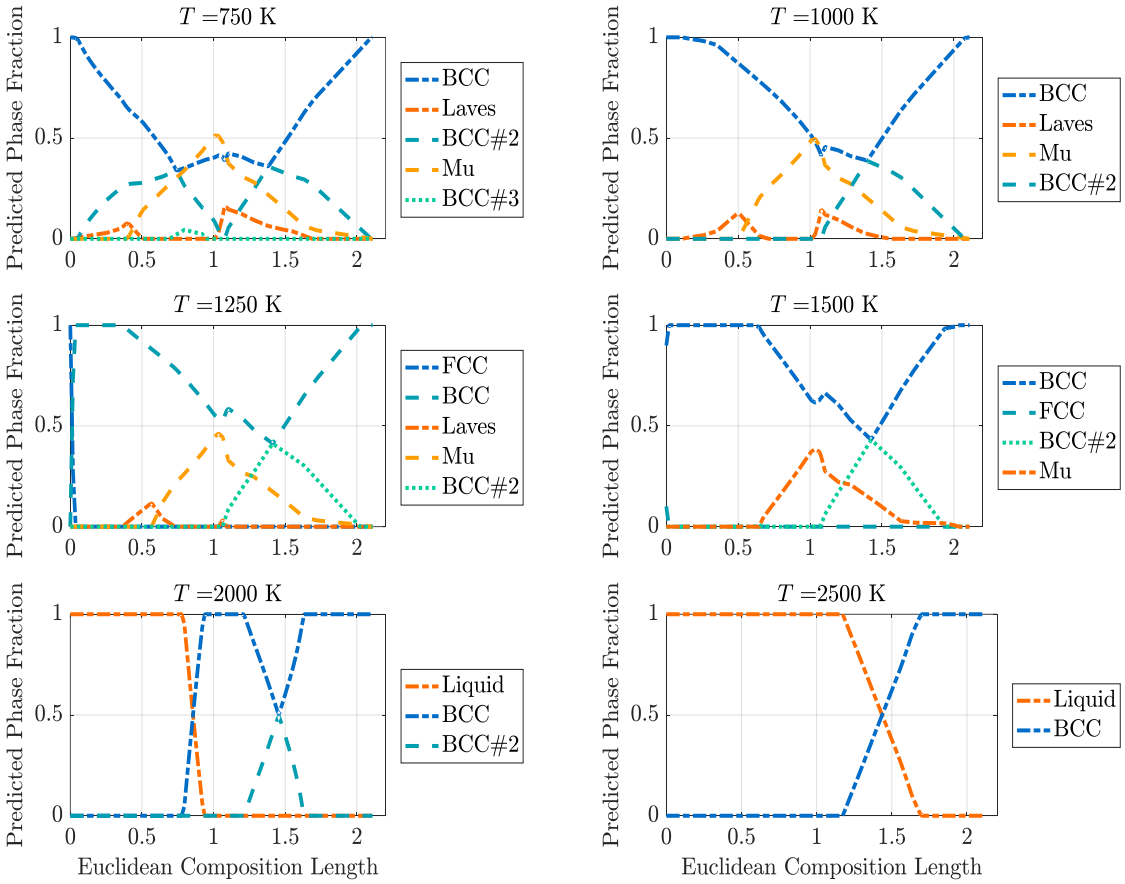

Figure 40. Equilibrium phase fractions along the optimal path (shown in Figure 37a) at various temperatures. Phases are numbered by descending phase fraction when multiple phases of the same structure are present. Consequently, phase numbering is not necessarily consistent with phase constitution.

APPENDIX C

PHANTOM DATA SETS

C.1 Data

The original test data available for this project is a series of thermal histories simulated by researchers at AFRL. These thermal histories are the result of thermal simulations of additive manufacturing processes. The simulations take processing parameters (ex. laser power and speed), material properties (ex. conductivity and heat capacity) and part characteristics (ex. part shape and laser track) as input. A thermal model is then used to create thermal histories at any point sampled from the simulated part. The thermal model considers simple thermal transfer effects like conduction but neglects more complex interactions like evaporation. Nevertheless, the model has been calibrated to experimental data and is assumed to be accurate.

Before experimental data is available, these thermal histories will be used to first predict pore-prone regions. These regions were identified by AFRL's experts to have increased porosity in most cases. Four sets of single-layer thermal histories were provided that focus on differentiating different types of locations. Figure 41 displays the four distinct datasets provided for this project. The first dataset represents a square cross-section with sampling points on the laser tracks, as seen in Figure 41 (a). Figure 41 (b) shows the second dataset which also has a square cross-section. However, the points are sampled both on and off the laser path. Figure 41 (c) displays an "L"-shaped cross-section that includes both short and long tracks. Lastly, a triangular cross-section that

again has varying track lengths is shown in Figure 41 (d). The ‘Square’ dataset consists of thermal histories sampled from 500 random locations.

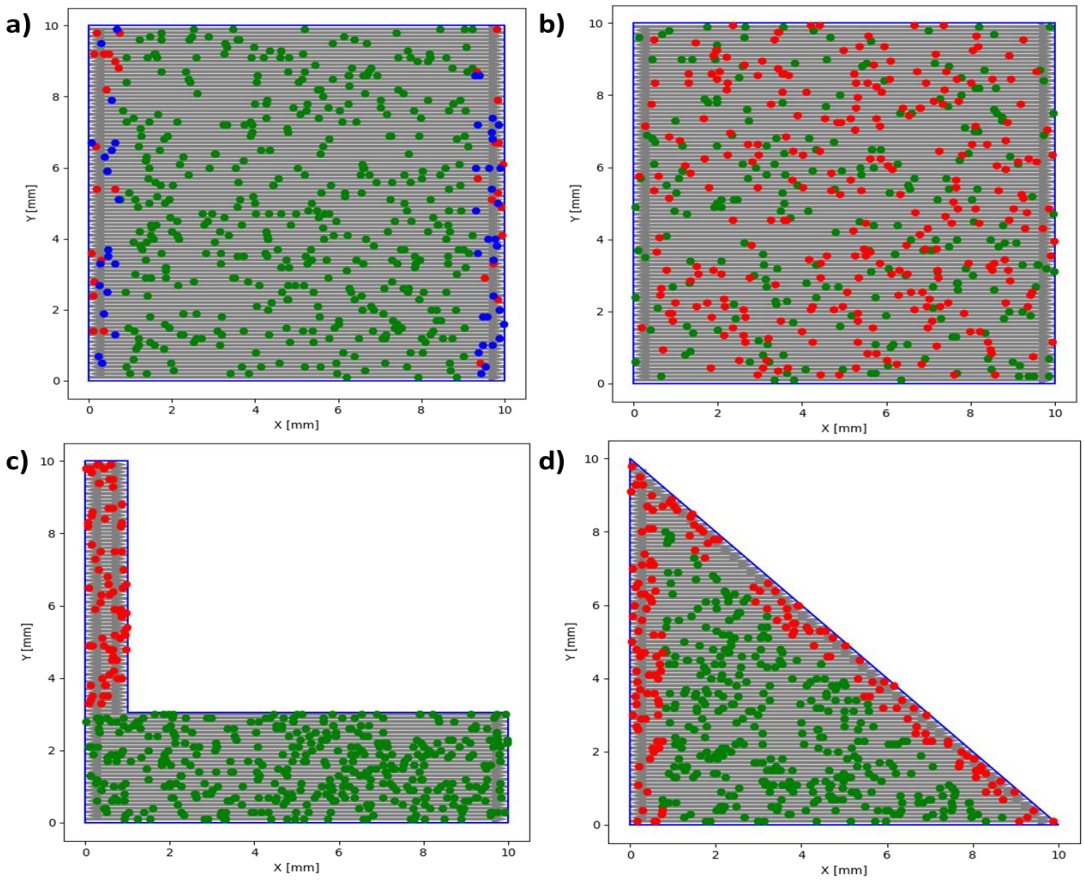

Figure 41. Visual representation of the data provided by AFRL for a (a) square cross-section, (b) square cross-section on and off the laser track, (c) “L”-shaped cross-section, and (d) triangular cross-section. Point colors indicate: (a) the start (blue), middle (green), and end (red) of a track; (b) points on (green) and off (red) the laser track; (c) long tracks (green) and short tracks (red); as well as (d) edge samples (red) and middle samples (green).

Each one of the 500 points has a separate CSV file with all temperature data listed along normalized time. Along with the raw thermal histories, each CSV contains an identification number, the number of time samples, two-dimensional location data,

absolute time when the beam comes closest to the point of interest, absolute time of the start of the thermal history, time interval between samples, and finally a tag indicating the samples location along the laser track: ‘Start’, ‘Middle’, or ‘End’. The goal of the present work is to be able to classify the thermal histories based on these three location labels. Of the 500 samples, 49 are ‘Start’ samples, 419 are ‘Middle’ samples, and 32 are ‘End’ samples. Figure 42 (a) displays the thermal histories for each of these classes separately. Several visual distinctions between each class can be observed. The largest peak in the ‘Start’ curves is followed by the second largest peak, while the second largest peak precedes the largest peak in the ‘End’ curves. Potential features could be extracted that attempt to describe this visual distinction. The ‘Middle’ curves, while more numerous, are far less uniform than the ‘Start’ or ‘End’ curves and might consequently be hard to distinguish. The ‘Square On-Off’ dataset, seen in Figure 41 (b), has the same geometry as the ‘Square’ dataset, but instead separates samples taken ‘On’ the laser track and ‘Off’ the laser track. There are 500 samples split evenly between each class, 250 each. Figure 42 (b) displays every thermal history plotterd for this dataset, separated by class. ‘Off’ samples tend to have smaller secondary peaks than the ‘On’ samples. Figure 41 (c) displays the ‘L’ dataset. This dataset demonstrates the differences between ‘Long’ tracks and ‘Short’ tracks. In this case, there are 486 total samples with 410 from ‘Long’ tracks and 76 from ‘Short’ tracks. As with the ‘Square’ dataset, the imbalance in sample distribution could skew error metrics. Figure 42 (c) displays the

thermal histories from this dataset. ‘Long’ samples tend to have multiple peaks, while ‘Short’ samples seem to have just one dominating peak.

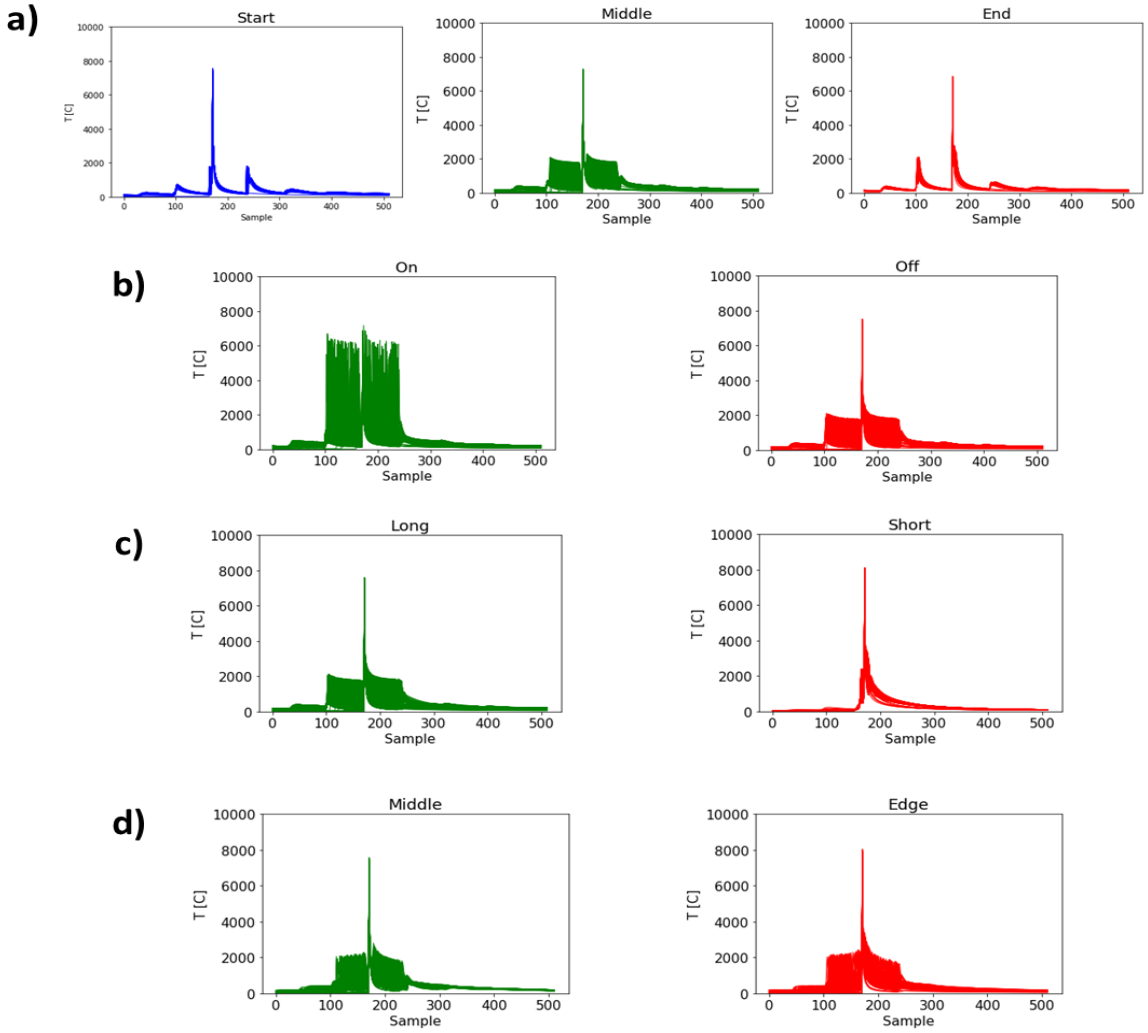

Figure 42. Every thermal history grouped by class and plotted together for the (a) square cross-section, (b) square cross-section on and off the laser track, (c) “L”-shaped cross-section, and (d) triangular cross-section. Line colors indicate: (a) the start (blue), middle (green), and end (red) of a track; (b) points on (green) and off (red) the laser track; (c) long tracks (green) and short tracks (red); as well as (d) edge samples (red) and middle samples (green).

Lastly, Figure 41 (d) shows the ‘Triangle’ dataset which attempts to combine a few characteristics from previous datasets. Similar to the ‘Square’ dataset, this dataset

seeks to differentiate between samples taken from the ‘Middle’ and ‘Edge’ of the part. However, because of its geometry, this dataset contains tracks of varying lengths, much like the ‘L’ dataset. The thermal histories from this dataset are plotted in Figure 42 (d). Unlike the other datasets, the ‘Middle’ and ‘Edge’ histories are difficult to visually distinguish. This may mean this dataset will be more difficult to classify.

The Informatics strategies are limited by the available data. In this case, the available data is sampled from random locations within the part. At each location, temperature measurements are taken at regular time intervals. The location samples are also tagged with a binary indicator that identifies the presence of a pore. These labels of ‘pore’ or ‘no pore’ enable the use of supervised machine learning techniques that can train an algorithm from a training data set. The nature of the problem, to identify pore locations given location data, suggests several characteristics of the informatics strategy.

C.2 Featurization

Initial featurization of the thermal histories began by extracting the peak temperatures of each history. Peaks or maximums were found by iterating through each time sample and recording temperatures that were greater than the temperatures immediately preceding it and following it in time. The number of peak temperatures extracted was limited to three because that was the minimum number of peaks experienced by any of the thermal histories and three features can be visualized relatively easily. Initially, peak temperatures were ordered by magnitude from greatest to smallest. The times corresponding to each maximum temperature were also recorded and put in the same order as their corresponding temperatures. Figure 43 displays an

example of a curve featurized in such a manner. Note that the resulting feature vector begins with the three largest peak temperatures ordered by magnitude (F1>F2>F3) followed by each temperature's corresponding time sample (F4, F5, F6).

Aside from ordering the peak temperatures by magnitude, a separate set of features was created by ordering the peak temperatures chronologically. As seen in Figure 42 (a), the chronological order of peak temperatures could be a descriptive feature. In the 'Start' curves, the largest peak is followed by the second largest peak while, in the 'End' curves, the second largest peak comes before the largest peak. Peak temperatures were obtained by first finding the maximum temperature in the curve. Then the first peak temperatures before and after the ultimate maximum were recorded. This method ensures that the middle feature (F2) is always the ultimate peak of the curve and that the other two features (F1 and F3) will be the first peaks on each side of the ultimate peak, as seen in Figure 44.

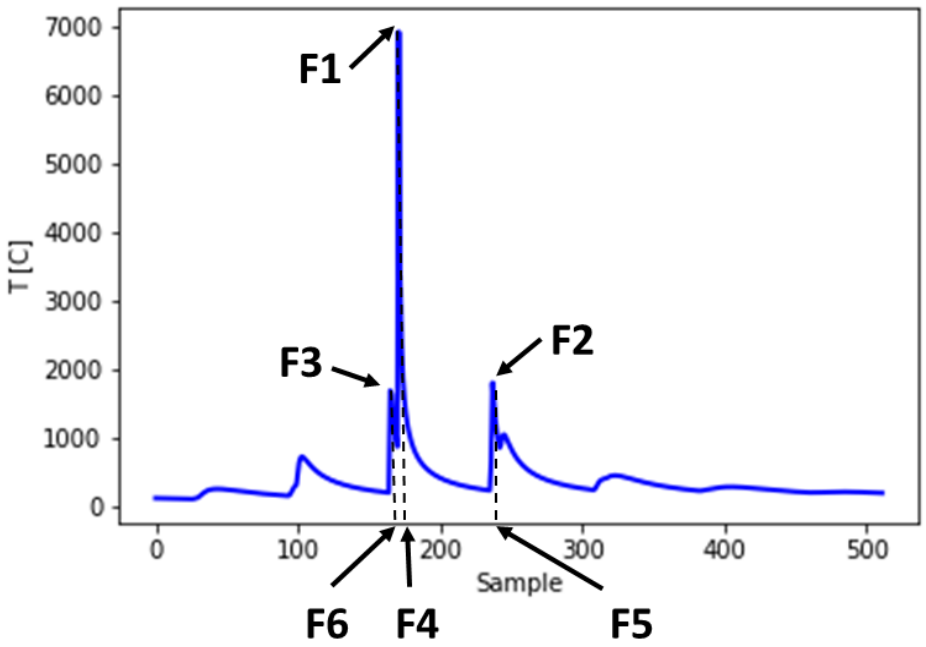

Figure 43. Example of how a thermal curve is featurized by peak temperatures. In this example, the three largest peak temperatures are taken and ordered by magnitude (F1>F2>F3). The corresponding time for each temperature is also taken and put in the same order as their corresponding temperatures.

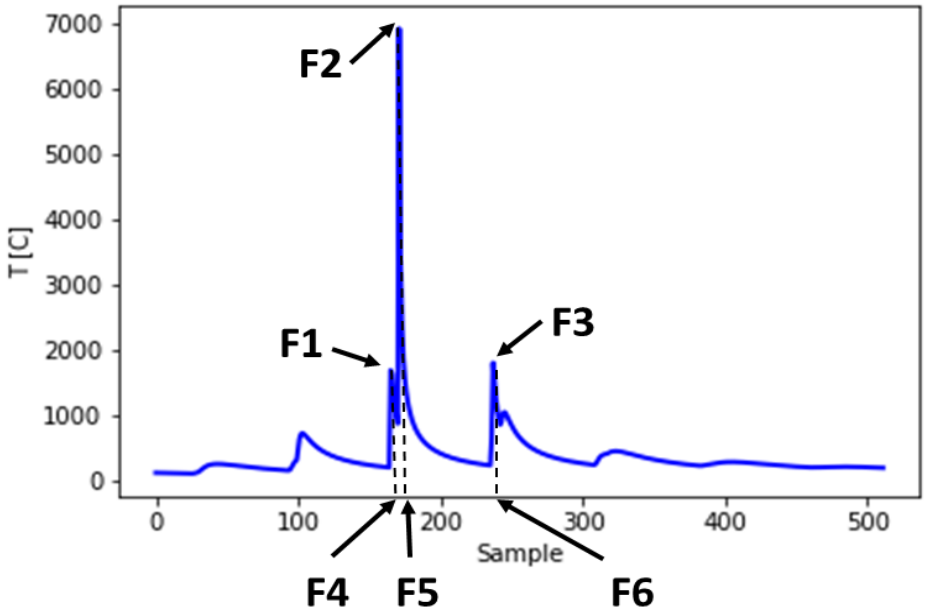

Figure 44. Peak temperatures ordered chornologically and centered on the maximum temperature (F1<F2>F3). The corresponding time for each temperature is also taken and put in the same order as their corresponding temperatures.

Principal Component Analysis (PCA) [38] was conducted on the first set of peak temperature features (see Figure 43) to select only those features that are most descriptive (i.e. can distinguish between classes). In short, PCA is an unsupervised (i.e. ignores class labels) technique that finds which features explain the most variance in the data. Figure 45 displays the portion of the variance explained by each Principal Component (PC). Note that the first three principal components explain more than 90% of the variance in the data. PCs are created from weighted linear combinations of the features. Table 3 displays the weight assigned to each feature in each principal component. Note that the first three PCs are almost entirely composed of the first three

features. Consequently, the first three features (the three largest peak temperatures) will most likely be the most important for classification, but all six features will be kept.

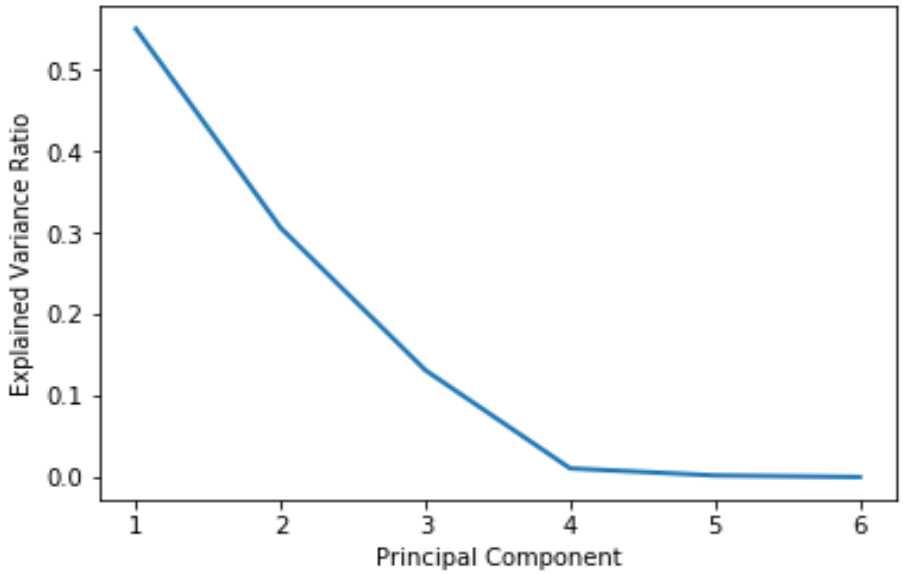

Figure 45. The ratio of variance explained by each principal component in the PCA conducted on the first set of features.

Table 3. Contribution of Each Feature in the First Feature Set to Each Principal Component

	PC1	PC2	PC3	PC4	PC5
F1	**-0.890**	**-0.375**	**0.257**	0.004	0.032
F2	**0.414**	**-0.463**	**0.773**	-0.082	-0.094
F3	**0.173**	**-0.802**	**-0.572**	0.002	0.011
F4	0	0	0	0	0
F5	-0.022	-0.007	-0.008	**0.691**	**-0.723**
F6	-0.073	0.041	-0.095	**-0.718**	**-0.684**

Figure 46 shows a pairwise plot of the first three principal components plotted against each other. In every plot, each class can be visually distinguished and seems clustered reasonably well. This is another good indicator that these features will be descriptive of the data.

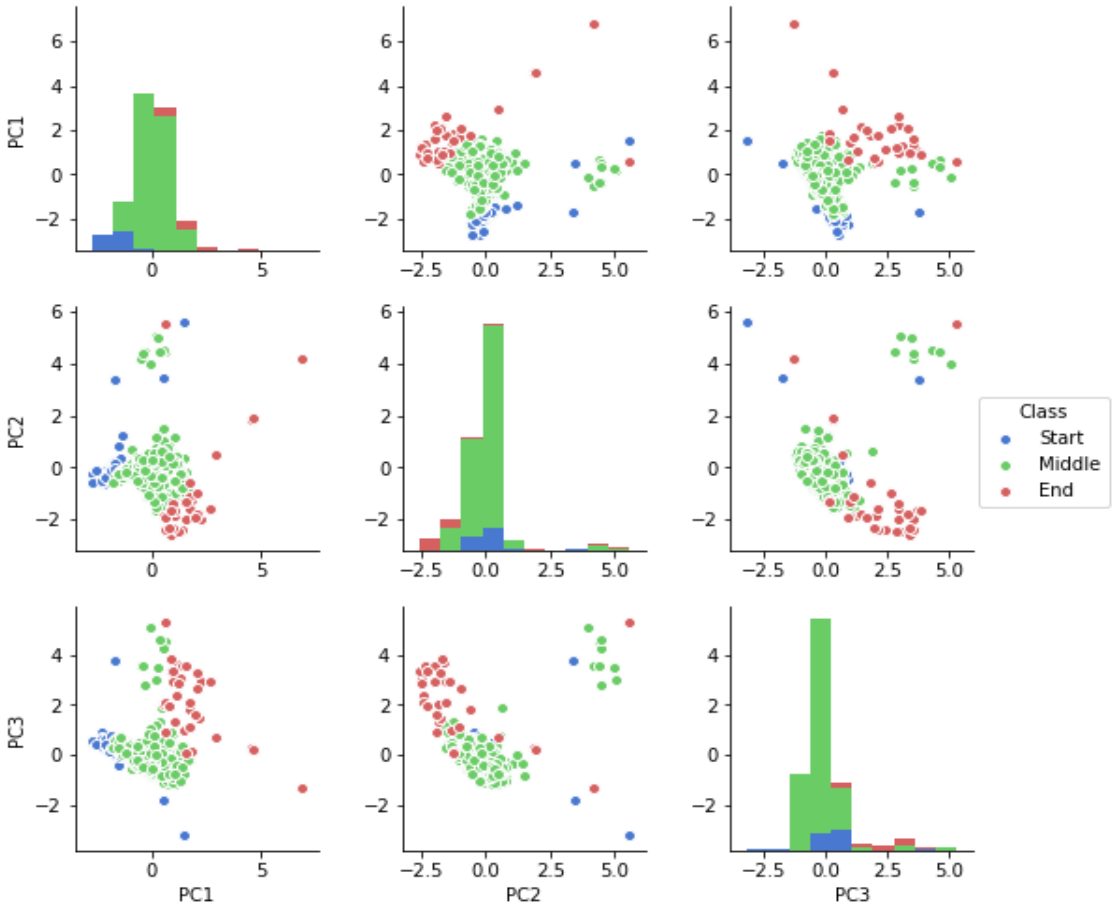

Figure 46. A pairwise plot of each of the first three principal components plotted against each other. The plots along the diagonal represent the distributions of the principal component values for each class.

C.3 Classification

Each feature set was used to train three different types of classifiers. The error of each classifier was then tested on a variety of error metrics. The following section details the methods used to construct and test these classifiers as well as the results obtained.

The first classifier used on the featurized data was a Support Vector Machine (SVM) [33]. In short, SVMs operate by finding the maximum margin hyperplane that separates the data in feature space. Mathematically, finding the hyperplane involves transforming the feature space into a hyper-dimensional space using what is called a 'kernel trick'. The type of kernel used (linear, polynomial, radial basis function, etc.) can have a significant effect on the shape of the hyperplane and thus the effectiveness of the classifier. In this work, a linear kernel was used given its simplicity and interpretability. SVMs are some of the most commonly used algorithms in the machine learning community as they are highly adaptable and have shown good performance in a wide set of applications.

Nearest Neighbor Classifiers (NNCs) [34] are relatively simple classifiers that are used frequently for simple datasets. Given a new test point, NNCs assign the class that is most common among the training points closest to the test point in feature space. In this work, a 5-Nearest-Neighbor classifier (5NN) was chosen, so the nearest 5 training points are sampled for every test point. While NNCs are quite robust and generalizable they can often suffer from overfitting given their simplicity and reliance on local observations.

The last type of classifier used to classify the thermal histories was a Decision Tree (DT) [35] classifier. In general, decision trees classify data by discretely binning data according to the value of a specific feature. This binning is done many times to create layers of the tree until a limit set by the user is reached. Decision trees are generally sought after for their interpretability as they can be seen as a series of logical decisions. However, they often fail to be as consistently accurate as SVMs given their discrete nature.

Several classification error metrics were used assess the performance of each classifier. The first and simplest error metric is the apparent error. Apparent error is simply the portion of the training data that is misclassified by the classifier. This error can be overly optimistic in many cases, particularly when the classifier is overfit to the training data. To combat this bias, the machine learning community often uses cross validation error as a more reasonable metric. Cross validation involves selecting some of the training data to reserve as a test set on which the classifier accuracy is scored. In this work, 5-fold cross validation was used to estimate classification error. As such, each dataset was binned into 5 partitions and each partition was used as the test set. The ultimate error estimation is simply the average of these 5 errors. The available data in this work presents an extra challenge for estimating classification error as each class is not represented equally. There are about ten times as many samples of the ‘Middle’ class as there of the ‘Start’ and ‘End’ classes. Because of this imbalance, error on the ‘Middle’ class will probably dominate the errors on the other classes. To mitigate this potential issue, 5 random samples of each class were reserved in a test set and the error of the

classifier was calculated on this set as a whole and for each class individually. The entire classification process was then repeated 100 times to prevent any effect this random process might have on the error metrics.

C.4 Preliminary Results

To begin the classification process, both featurization strategies were applied to the ‘Square’ dataset to obtain two feature sets (peak temperatures ordered by (1) magnitude and (2) chronologically). The error metrics of each classifier (averaged over 100 runs) trained on both feature sets can be seen in Table 4. The best performing classifiers were the SVM and DT classifiers. These classifiers had less than 10% error on both feature sets, but errors were generally smaller on the chronological feature set. As such, the SVM and DT classifiers trained on the chronological feature set were deemed to have the best performance (and consequently highlighted in green). These classifiers performed very well on the ‘Start’ and ‘End’ classes but tended to misclassify the ‘Middle’ class at a higher rate. This is likely because the ‘Start’ and ‘End’ classes are highly differentiable (the second largest peak always precedes the largest and vice versa) while the ‘Middle’ class exhibits a wider range of curve characteristics.

Table 4. Square Dataset Error Metrics of Each Classifier (Averaged from 100 Runs)

		Error Percent					
	Classifier	Apparent	5-fold CV	Test Set	Start	Middle	End
Feature Set 1	*Peak temperatures ordered by magnitude*						
	SVM	2.3%	2.7%	8.1%	1.2%	10.0%	13.0%
	5NN	3.3%	4.0%	13.3%	0%	16.8%	23.0%
	DT	0%	1.2%	3.5%	0.2%	7.0%	3.2%
Feature Set 2	*Peak temperatures ordered chronologically*						
	SVM	0.0%	1.5%	1.9%	0%	5.8%	0%
	5NN	3.1%	3.6%	14.0%	0.2%	16.2%	25.6%
	DT	0%	0.7%	2.9%	0.4%	8.4%	0%

Table 5 displays the error metrics for classifiers trained on the 'Square On-Off' dataset. These errors were, generally speaking, lower than those obtained for the 'Square' dataset as all error metrics are less than 10% for every classifier. This could possibly be attributed to fewer classes (two instead of three) and equal sample sizes for each class. It is also possible that is easier to differentiate samples taken from 'On' or 'Off' the track than samples taken from the 'Start', 'Middle', or 'End' of the track, because the first case might simply be a change in peak magnitudes while the second is likely a shift in peak positions. The best performing classifiers were the SVM and 5NN trained on the second feature set, which had identical errors. These classifiers performed perfectly on the 'On' class but misclassified the 'Off' class at a rate of 5.6%.

Table 5. Square On-Off Dataset Error Metrics of Each Classifier (Averaged from 100 Runs)

		Error Percent				
	Classifier	Apparent	5-fold CV	Test Set	On	Off
Feature Set 1	*Peak temperatures ordered by magnitude*					
	SVM	3.9%	4.2%	4.2%	2.8%	5.6%
	5NN	2.8%	3.4%	2.8%	0.6%	5.0%
	DT	0%	5.1%	4.2%	4.4%	4.0%
Feature Set 2	*Peak temperatures ordered chronologically*					
	SVM	2.7%	2.7%	2.8%	0%	5.6%
	5NN	2.7%	2.7%	2.8%	0%	5.6%
	DT	0%	5.6%	7.1%	8.2%	6.0%

The results of the classifiers trained on the ‘L’ dataset can be seen in Table 6. These errors are generally as low as those seen in Table 5. In general, the ‘Short’ class was misclassified at a higher rate than the ‘Long’ class, which was rarely, if ever, misclassified. This can likely be attributed to the much smaller sample size of the ‘Short’ class. The best performing classifier, the SVM trained on the second feature set, had zero error by every metric. The reason behind this particular classifier’s perfect performance has yet to be identified.

Table 6. L Dataset Error Metrics of Each Classifier (Averaged from 100 Runs)

		Error Percent				
	Classifier	Apparent	5-fold CV	Test Set	Long	Short
Feature Set 1	*Peak temperatures ordered by magnitude*					
	SVM	1.8%	2.4%	5.0%	0.4%	9.6%
	5NN	1.3%	2.3%	6.0%	0%	12.0%
	DT	0%	1.8%	2.6%	0.8%	4.4%
Feature Set 2	*Peak temperatures ordered chronologically*					
	SVM	0%	0%	0%	0%	0%
	5NN	1.1%	2.1%	5.0%	0%	10.0%
	DT	0%	0.7%	2.0%	0%	4.0%

Lastly, the results of the classifiers trained on the ‘Triangle’ dataset can be seen in Table 7. These errors are generally much higher than those of any of the other datasets. This is likely because, as discussed in Section 6 and seen in Figure 41 (d), this dataset combines several of the characteristics of the other datasets and, consequently, presents a more challenging classification problem. Nevertheless, the best performing classifiers, the DTs, had about 5% error. The Decision Trees could have performed considerably better because they divided the problem into differentiating track length first (resolving the complications of geometry) and then location on the track second. The confirmation of this strategy can be determined by attempting to interpret the DTs, but this is left to future work. In general, the ‘Edge’ class was misclassified at a much higher rate than the ‘Middle’ class. This could be because there were two to three times as many samples of the ‘Middle’ class as the ‘Edge’ class, 339 to 161 respectively. It could also be attributed to the fact that samples from the start and end of the track (as in

the ‘Square’ dataset) are lumped together into one ‘Edge’ class even though they can be quite different, as seen in Figure 42 (a).

Table 7. Triangle Dataset Error Metrics of Each Classifier (Averaged from 100 Runs)

		Error Percent				
	Classifier	Apparent	5-fold CV	Test Set	Middle	Edge
Feature Set 1	*Peak temperatures ordered by magnitude*					
	SVM	19.3%	19.2%	27.9%	7.6%	48.2%
	5NN	7.2%	10.5%	12.6%	4.8%	20.4%
	DT	0%	5.0%	5.0%	3.0%	7.0%
Feature Set 2	*Peak temperatures ordered chronologically*					
	SVM	19.5%	20.4%	27.0%	4.2%	49.8%
	5NN	7.1%	9.6%	11.8%	7.8%	15.8%
	DT	0%	5.2%	5.1%	3.8%	6.4%